ERROR ANALYSIS OF REFLECTION-ONLY MATERIAL CHARACTERIZATION METHODS

By

Raenita Ann Fenner

A DISSERTATION

Submitted to
Michigan State University
in partial fulfillment of the requirements
for the degree of

DOCTOR OF PHILOSOPHY

Electrical Engineering

2011

ABSTRACT

ERROR ANALYSIS OF REFLECTION-ONLY MATERIAL CHARACTERIZATION METHODS

By

RAENITA ANN FENNER

Material characterization is the process of determining the electrical properties of a material by using knowledge of how electromagnetic waves reflect and transmit through a material sample. This characterization can be critical to the design of high-speed circuits and packaging, microwave remote sensing, bioengineering, food engineering, agriculture, and general materials science. An interesting problem within material characterization is the non-contact, non-destructive characterization of conductor-backed media. Conductor-backed media are materials which are directly adhered to a good or a perfect electric conductor (PEC). This scenario occurs in real-life applications such as the characterization of *in-situ* materials or characterization of shielding apparatus. For this specific case, reflection-only methods must be used because measurement of transmission properties is impossible due to the PEC backing.

The main focus of this dissertation is the study of the strengths and weaknesses of various reflection-only material characterization methods by performing a thorough error analysis. More specifically, the propagation of measurement errors into extracted material parameters is investigated. Such analysis is lacking in the material characterization area. Key contributions of this research are (1) a general formulation for deriving reflection-only material characterization methods, (2) a general process for determining the propagated error into many reflection-only material characterization methods, (3) a method for characterizing conductor-backed media, (4) expanding the use of interval analysis in the electromagnetic community, and (5) determining the impact of wave curvature on free-space reflection-only material characterization methods.

To my loving husband for all of his love and support.

I would not have made it without you.

ACKNOWLEDGMENTS

When I think upon the years that I have spent writing this dissertation, I am reminded of the great author Maya Angelou when she said "*We delight in the beauty of the butterfly, but rarely admit the changes it has gone through to achieve that beauty.*" Throughout my time at Michigan State University, I have gone through an intellectual, professional, and spiritual metamorphosis. However, all that I have achieved was not done alone and many people and organizations deserve my many thanks.

First, I would like to thank the person at the cornerstone of my intellectual growth, my advisor Dr. Edward Rothwell. Dr. Rothwell has been a patient and knowledgable teacher and counselor. It has been a pleasure working with you for the past six years, and I hope we can continue to work together in the future.

I also would like to thank my committee members Dr. Shanker Balasubramaniam, Dr. Leo Kempel, and Dr. Lydell Frasch. Thank you for sharing your wealth of knowledge and your constant support in this process. Additionally, I would like to especially like to thank Dr. Frasch, Boeing, and the Air Force Research Lab for sponsoring several years of my doctoral studies.

Professionally, I have learned an immense amount of knowledge from participation in the Sloan program and the AGEP program. The Sloan program has been a home away from home for me. I would like to thank Dr. Percy Pierre and Dr. Barbara O'Kelly for all of your behind the scenes help and organization of a program which transformed my graduate school experience.

Many, many thanks are given to all of my family and friends. To my parents, you have been there for me for my entire life. You sowed the seeds for me to succeed in earning this degree many years ago. One of the most important lessons you taught me was to never give up and to not be a quitter. I am forever thankful for all of your support and prayers, and especially for the confidence you have always had in me, even when I didn't have it for myself.

To my husband, Dr. Anthony Plummer, Jr, I am so proud of all of your accomplishments. I know without a doubt that I would not be here today if it wasn't for all of the intangible support

you provide for me.

Last but not least, I give honor to my savior Jesus Christ. There were many days I thought I would not complete this work, but the strength you gave me enabled me to push through the tough times. I owe everything to you and I hope I share with others the blessings you have bestowed upon me.

Table of Contents

List of Tables

List of Figures

Chapter 1

The Introduction

1.1 Overview of Material Characterization

1.1.1 A Brief History of Materials Science and Material Characterization

The study of materials has spanned the history of human kind. Early materials research can be conceptualized as early humans learning which natural resources were suitable for building shelter, making tools, fabrics, weapons, etc. As time has moved forward, human technological and societal advancements have lead to much more sophisticated research and applications of materials.

In today's society, the impact of materials research is ubiquitous. Materials research encompasses the design of automobiles, electronic devices, health and beauty products, computer networks, green energy technologies, etc. Subsequently, materials research spans many disciplines and fields of study. Materials science and engineering embodies metallurgy, chemical engineering, physics, inorganic chemistry, organic chemistry, crystallography, electrical engineering, and many more areas of study [42]. Each one of these disciplines examines a specified set of physical material properties. For example, a crystallographer may study the diffraction patterns caused by materials to examine the the physical arrangement of atoms within a solid. Alternatively, an organic chemist may study the solubility or melting/boiling point of a material.

Within the discipline of electromagnetics (in the context of electrical engineering), of large interest is *material characterization.* Material characterization is the process of determining the intrinsic properties of materials with knowledge of the material's response to electromagnetic waves. The intrinsic properties of materials are the properties due to the underlying physical behavior of the material, as opposed to extrinsic properties which are performance related properties (resonance, intrinsic impedance, reflectivity, etc.). Intrinsic properties include permittivity, ϵ, magnetic permeability, μ, conductivity, σ, propagation parameters, and electrical transport parameters [33].

1.1.2 The Physical Nature of Materials in the Presence of Electric and Magnetic Fields

The characterization of materials in electromagnetics is largely dependent on the macroscopic physical behavior of materials in the presence of an electromagnetic field. Maxwell's equations and the constitutive relations govern the macroscopic relationship between the electromagnetic field and the media through which the field is propagating. Maxwell's equations and the constitutive relations defined in the frequency domain are

$$\nabla \times \vec{E} = -\jmath\omega\vec{B} \tag{1.1}$$

$$\nabla \times \vec{H} = \jmath\omega\vec{D} + \vec{J} \tag{1.2}$$

$$\nabla \cdot \vec{D} = \rho \tag{1.3}$$

$$\nabla \cdot \vec{B} = 0 \tag{1.4}$$

$$\vec{D} = \epsilon\vec{E} = (\epsilon' - \jmath\epsilon'')\vec{E} \tag{1.5}$$

$$\vec{B} = \mu\vec{H} = (\mu' - \jmath\mu'')\vec{H} \tag{1.6}$$

$$\vec{J} = \sigma\vec{E}. \tag{1.7}$$

In equations 1.1-1.7, $\vec{E}$ is the electric field strength vector, $\vec{H}$ is the magnetic field strength vector, $\vec{D}$ is the electric flux density, $\vec{B}$ is the magnetic flux density, and $\vec{J}$ is the current density vector. Also, ρ is the electric charge density, ϵ is the complex permittivity, μ is the complex permeability, and σ is the conductivity. Examination of equations 1.1-1.7 shows that ϵ, μ, and σ determine the electromagnetic response and spatial penetration of electromagnetic fields at a particular frequency [33].

It is important to note here that through specification of equations 1.5-1.7 that a specific class of materials have been defined. Again, the characteristics of ϵ, μ, and σ determine the electromagnetic behavior of materials. Therefore, if ϵ, μ, or σ are dependent on applied field strength, orientation, or on spatial coordinates equations 1.1-1.7 will have to be adapted. For instance, if ϵ, μ, or σ depend on applied field strengths in a non-linear fashion, the material is termed *non-linear*. Thus, 1.5-1.7 will have ϵ, μ, or σ depend non-linearly on applied $\vec{E}$ and $\vec{H}$. If ϵ, μ, or σ depend on orientation, the material is said to be *anistropic*. For anistropic materials, ϵ, μ, or σ can be second-rank tensors or matrices. Lastly, if ϵ, μ, or σ depend on spatial coordinates then the material is termed *inhomogeneous*. For inhomogeneous materials, ϵ, μ, or σ are functions of space [15]. Moreover, it is important to note the behavior of materials can vary due to temperature, applied field strength, operating frequency, pressure, etc. A case in point is that, if a material placed within a weak electric field may behave in a linear fashion, while a material placed in a strong electric field may behave in a non-linear fashion. In this work, only *linear, isotropic, homogeneous* materials are considered. Also, all analysis is conducted in the *frequency domain.*

Along these lines, materials are grouped appropriately by their ϵ, μ, and σ values. To make comparison of materials more simple, all materials are related to the electromagnetic properties of free-space. The properties of free-space include $\epsilon_\circ \approx 8.859 \times 10^{-12}$ F/m, $\mu_\circ = 4\pi \times 10^{-7}$ H/m, and $\sigma = 0$ S/m. All other material parameters are defined in terms of the free-space values of ϵ and μ. Respectively, ϵ and μ are defined as follows:

$$\epsilon = \epsilon'_r \epsilon_0 - \jmath \epsilon''_r \epsilon_0, \ \ \epsilon'_r \geq 1, \ \epsilon''_r \geq 0 \tag{1.8}$$

$$\mu = \mu'_r \mu_0 - \jmath \mu''_r \mu_0, \ \ \mu'_r \geq 1, \ \mu''_r \geq 0. \tag{1.9}$$

Generally, materials are classified by either their conductive (σ) or magnetic properties μ_r. Classic organization of materials by their conductive properties includes dielectrics (or insulators), semiconductors, and conductors. All three classification of materials have minor responses to magnetic fields, but are generally considered non-magnetic ($\mu \approx \mu_\circ$).

In terms of magnetic properties, materials are classified as either diamagnetic ($\mu < \mu_\circ$), paramagnetic ($\mu \geq \mu_\circ$), or highly magnetic ($\mu \gg \mu_\circ$). Ferromagnetic and Ferrimagnetic materials are considered highly magnetic materials. Although, many magnetic materials are also highly conductive, they are still considered magnetic because their magnetic properties are more meaningful in application.

In this work, of special interest are dielectric and paramagnetic materials. Dielectrics and paramagnetic materials are of special interest because they are commonly used in microwave measurements and applications which are described in Section 1.2. Therefore, the behavior of dielectrics and paramagnetic materials are qualitatively described in order to understand theoretical calculations, measurements, and possible sources of error in the characterization process.

Dielectric Materials

The physical response which determines the permittivity of materials is displacement of free and bound electrons due to the electric field [33]. The complex permittivity of a dielectric material is thus determined by several physical phenomena related to the displacement of free and bound electrons. The prominent physical phenomena responsible are ionic conduction, dipolar relaxation, atomic polarization, and electronic polarization [22]. Figure 1.1 shows that permittivity is frequency dependent and different physical phenomena are dominant at different frequencies [28]. Dipolar relaxation is the process of the misalignment of permanent and induced dipoles due to thermal noise. At lower frequencies, dipolar relaxation is dominant because the thermal effect on atoms is not overshadowed other dielectric phenomena. Also prevalent at lower frequencies is ionic conductivity. Ionic conductivity is due to electrolytic conduction of free ions. Ionic conductivity mostly introduces losses to the material and hence is a major contributor to ϵ_r''.

In the visible light and ultraviolet parts of the spectrum, electronic polarization dominates. Electronic polarization is due to induced dipoles created by the separation of positively charged atomic nuclei from negatively charged electron clouds. At microwave and infrared frequencies, atomic polarization dominates which is caused by deformation of the electron cloud due to applied electric field.

Diamagnetic and Paramagnetic Materials

Similar to how permittivity is related to the displacement and relaxation of free and bound electrons, permeability is related to changes of electron orbits due to applied magnetic fields [46]. Essentially, the electrons spinning in their orbits can be thought of as magnetic dipoles. The physical phenomenon which affects the permeability is analogous to Faraday's law. Fundamentally, a time-varying magnetic field induces an electric field. In turn, the electric field induces a current which generates a secondary magnetic field which opposes the original magnetic field. Like permittivity, the permeability is frequency dependent. In addition, the magnetic properties of materials can vary based on operating temperature, pressure, etc.

1.2 Microwave Material Characterization

As noted, the macroscopic electric and magnetic behaviors of materials vary from material to material (e.g. - dielectrics, magnetic materials, superconductors), frequency, and temperature, etc.. Therefore, there is not one special material characterization method which is applicable to all materials across all possible deployment environments. Accordingly, a sub-area of material characterization is characterizing materials at microwave frequencies.

1.2.1 A Brief History of Material Characterization at Microwave Frequencies

Research on characterization of materials dates back to late 1800's. In [47], there is reference of characterization of materials at microwave frequencies as early as 1895 by Drude in [14]. Drude developed two methods to characterize materials. One method entailed measuring wavelength with a pair of lecher wires, a pair of parallel wires or rods. Another method included measuring the capacitance of a small resonant capacitor.

World War II created the need for electromagnetic signature control and reducing radar cross sections. These applications required the design of tailor made composite materials for radar absorbtion. In 1940, the basic ideas by Drude were expanded upon by von Hipple in [22]. von Hipple described what he termed a "hollow pipe" method. The method utilized an instrument similar to a slotted line which had a transmitter at one end and a metallic boundary at the opposite end. The methodology included placing a dielectric sample adjacent to the metallic boundary and measuring the voltage maximum and minimum parallel to the length dimension of the pipe. By 1947, the "hollow pipe" method was expanded upon in [12] with a rectangular waveguide system. In [12], characterization was done on a variety of materials like nylon, teflon, pork meat, and ivory. The real part of the permittivity, loss tangent, attenuation constant, index of refraction, and power reflection coefficient were characterized for all of the materials.

By 1967, microwave material characterization was influential in the design of circuits and wave transmission calculations. New characterization methods including capacitor, liquid immersion, cavity, and transmission line measurements were cited as state of the art microwave material characterization methods in [9].

Today microwave material characterization is critical to the design of high-speed circuits and packaging, microwave remote sensing, bioengineering, food engineering, agriculture, general materials science, etc. [39],[56].

1.2.2 Classification of Microwave Material Characterization Methods

Considering all of the various applications of microwave material characterization, it makes sense that there are an abundance of characterization methods to suit the variety of applications. Frequency, availability and size of material samples, dielectric losses, anistropy all determine which characterization method should be used [29].

Microwave material characterization methods can broadly be classified as either resonant methods or nonresonant methods. Resonant methods are generally used for characterizing dielectrics at a single frequency or at several discrete frequencies. Common examples of resonant methods are the resonant-perturbation method and the resonator method [33].

Nonresonant methods are generally used to characterize materials over a broad frequency range. Nonresonant methods make use of the difference between material impedances and wave velocities. For instance, as a wave transitions between free-space and a dielectric sample, the difference between the impedance and wave velocity of free-space and the dielectric sample provide a means to calculate the permittivity and permeability. Nonresonant methods are further broken down into reflection/transmission methods and reflection-only methods. Reflection/transmission methods use measurement of both the reflection coefficient and transmission coefficient. The most popular reflection/transmission method is the Nicholson-Ross-Weir (NRW) algorithm described in [40] and [54].

Reflection-only methods, as the name implies, use only data gathered by measuring the reflection coefficient. Reflection-only methods can be realized with waveguide, coaxial-line, or free-space implementations.

1.2.3 Characterization of Conductor-Backed Media: Reflection-Only Methods

An interesting problem within microwave material characterization is the noncontact, nondestructive characterization of conductor-backed media. Conductor-backed media are materials which are directly adhered to a good or a perfect electric conductor (PEC). This scenario occurs in real-life applications such as the characterization of *in-situ* materials or characterization of shielding apparatus [7]. For this specific case, reflection-only methods must be used because measurement of transmission properties is impossible due the PEC backing.

There are many different implementations of reflection-only methods. Coaxial-line reflection-only methods are a popular type of reflection-only methods. Coaxial-line methods are realized with open-ended coaxial probes or coaxial-line cells. Open-ended coaxial probes are coaxial transmission lines where the outer conductor is bent such that the inner conductor is flush with the material sample. Coaxial-line cells are coaxial transmission lines designed such that material samples can be placed within the coaxial cell. Many coaxial-line methods can also be adapted for waveguide methods. There are many advantages to coaxial-line methods which include that they are:

1. Quick, easy and relatively cheap
2. A single probe can be used over a frequency range of with suitable samples
3. Well-suited for non-destructive testing
4. One of the best techniques at microwave frequencies for high loss and medium loss samples.

Although coaxial-line methods have several positive attributes, they are not useful when *noncontact*, non-destructive material characterization methods are necessary. Noncontact methods are often needed in quality control or diagnostic material characterization. When noncontact methods are necessary, coaxial-line methods cannot be used. In these cases, *free-space* material characterization methods are mandatory. Free-space material characterization methods are methods that illuminate a planar material sample with a plane wave. A far-field requirement, appropriate sample size compared to a wavelength, and an environment few additional scatters are necessary to perform free-space methods.

There are several well-known reflection-only free-space material characterization methods. Some of these methods include the:

1. Layer-Shift Method [3]
2. Two-Thickness Method [4]
3. Air/Conductor Method [33].

The free-space methods mentioned here are explained in detail in Chapter 4.

Unfortunately, all of these well-known free-space methods require some form of contact with the sample material or alteration to the structure containing the sample. This leaves the engineer who wishes to perform *noncontact, non-destructive* material characterization on *conductor-backed media* in a precarious situation.

1.3 Overview and Contributions of this Work

The main goals of this work is dual-fold. One goal is to provide a thorough error analysis of reflection-only material characterization methods. Error analysis is of high importance to engineers who perform material characterization. Error analysis is important because it is critical to know to what extent the extracted permittivity and permeability are valid for a sample material.

The first step in the error analysis is the formation of a general set of extraction equations for all reflection-only material characterization methods; this work is presented in Chapter 4. This is an important step because it provides a starting point for an error analysis for all reflection-only methods. In addition, the general formulation provides a central set of extraction equations which can be referenced by everyone wishing to use reflection-only material characterization.

In addition, implementation of a relatively new error analysis method, interval analysis, is introduced in Chapter 6 and sensitivity of reflection-only methods on wavefront curvature is discussed in Chapter 7.

The second goal of this work is find a suitable way to characterize conductor-backed media in a noncontact, non-destructive fashion. Noncontact, non-destructive characterization of materials have been demonstrated in [6] with a coaxial probe and in [49] and [50] with an ellipsometry technique. However, there still is not a *free-space* noncontact, non-destructive method to characterize conductor-backed media. Research on what is termed the dual-polarization method is demonstrated in Chapter 5. The dual-polarization method is a way to characterize conductor-backed dielectrics and magnetic media.

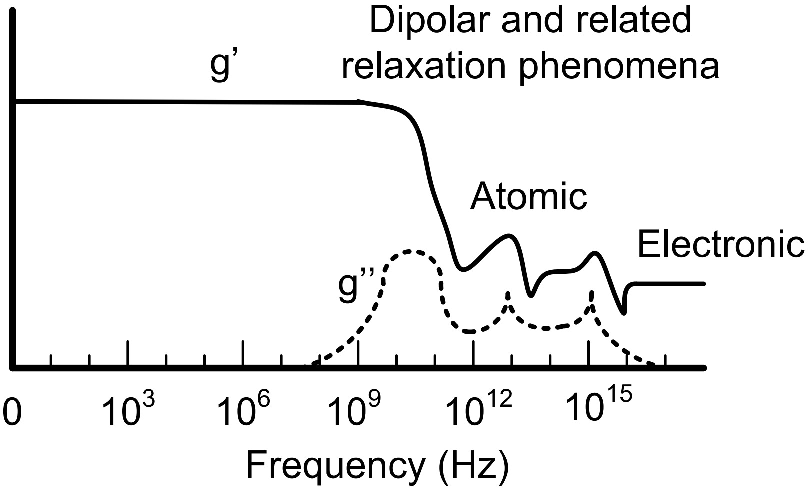

Figure 1.1: Permittivity vs. frequency for a hypothetical dielectric [46]

Chapter 2

Plane Wave Propagation

The characterization of materials with reflection-only free-space techniques requires the analysis of plane wave reflection off of a planar slab. Thus, the canonical problem, shown in Figure 2.1, of plane wave incidence on an infinite slab is of great importance. Furthermore, the reflection-only coaxial-line and waveguide methods presented in this work can be considered special cases of plane wave propagation.

Since the canonical problem of plane wave incidence on an infinite planar slab is essential to the study of reflection-only material characterization methods, the general analysis of this canonical problem is shown in detail. Topics covered in this chapter include: (1) plane wave propagation in unbounded media, (2) reflection and transmission at normal and oblique incidence, and (3) reflection and transmission at layered slabs.

2.1 Time-Harmonic Uniform Plane Waves in Unbounded Media

As a starting point, the understanding of plane wave propagation in unbounded media is fundamental to the analysis of the canonical problem of plane wave reflection off of an infinite slab. A plane wave is a wave where the surfaces of constant phase are planes. A plane wave is termed *uniform* when the field amplitudes are constant over the surfaces of constant phase.

The study of time-harmonic plane waves in unbounded media starts with the time-harmonic form of Maxwell's equations in equations (2.1)-(2.4), which are

$$\nabla \times \vec{E} = -\jmath\omega\vec{B} \tag{2.1}$$

$$\nabla \times \vec{H} = \jmath\omega\vec{D} \tag{2.2}$$

$$\nabla \cdot \vec{D} = 0 \tag{2.3}$$

$$\nabla \cdot \vec{B} = 0. \tag{2.4}$$

Only source-free ($\rho = 0$ and $\vec{J} = 0$), linear, homogeneous, isotropic, and time-invariant media are considered. The constitutive relations for such a medium are

$$\vec{D} = \epsilon\vec{E} = (\epsilon' - \jmath\epsilon'')\vec{E} \tag{2.5}$$

$$\vec{B} = \mu\vec{H} = (\mu' - \jmath\mu'')\vec{H}. \tag{2.6}$$

Taking the curl of both sides of equation (2.1), yields

$$\nabla \times \nabla \times \vec{E} = -\jmath\omega(\nabla \times \vec{B}). \tag{2.7}$$

Using a vector identity, the left-side of equation (2.7) can be rewritten as

$$\nabla \times \nabla \times \vec{E} = \nabla(\nabla \cdot \vec{E}) - \nabla^2\vec{E}. \tag{2.8}$$

In consideration of ϵ being independent of spatial coordinates and equations (2.3) and (2.5), the $\nabla(\nabla \cdot \vec{E})$ term can be rewritten as in [24] as

$$\nabla \cdot \vec{D} = 0 = \nabla \cdot \epsilon \vec{E} = \epsilon \nabla \cdot \vec{E} \rightarrow \nabla \cdot \vec{E} = 0. \tag{2.9}$$

The right side of equation (2.7) can be written in terms of $\vec{E}$ by using equations (2.2) and (2.6) such that

$$\nabla \times \vec{B} = \mu(\nabla \times \vec{H}) = \jmath \omega \mu \epsilon \vec{E}. \tag{2.10}$$

Replacing the left side of equation (2.7) with equation (2.9) and the right side with equation (2.10) gives the very important result of

$$\nabla^2 \vec{E} - \omega^2 \mu \epsilon \vec{E} = 0. \tag{2.11}$$

A similar process can be followed by starting with equation (2.2) to yield

$$\nabla^2 \vec{H} - \omega^2 \mu \epsilon \vec{H} = 0.. \tag{2.12}$$

Equations (2.11) and (2.12) are the homogeneous vector Helmholtz equations. In rectangular coordinates, the vector Helmholtz equations can be separated into three equations of the form

$$\nabla^2 \Psi - k^2 \Psi = 0, \tag{2.13}$$

where Ψ is one of the three components of the electric field in either the x, y, or z direction. Through the separation of variables, equation (2.13) has a product solution of harmonic, propagating wave functions $\Psi = A(\omega) e^{\pm \jmath k_x(\omega) x} e^{\pm \jmath k_y(\omega) y} e^{\pm \jmath k_z(\omega) z}$. The solution to equation (2.11) is therefore

$$\vec{E}(\vec{r}, \omega) = \vec{E}_{\circ}(\omega) e^{\pm \jmath k_x(\omega) x} e^{\pm \jmath k_y(\omega) y} e^{\pm \jmath k_z(\omega) z}. \tag{2.14}$$

In equation (2.14), $\vec{E}_\circ$ is the vector amplitude of the plane wave. For a more compact form of equation (2.14), the wave vector is defined as $\vec{k} = k_x\hat{x} + k_y\hat{y} + k_z\hat{z}$ with $k^2 = \omega^2\mu\epsilon = k_x^2 + k_y^2 + k_z^2$ as its magnitude. Hence,

$$\vec{E}(\vec{r},\omega) = \vec{E}_\circ e^{-\jmath\vec{k}\cdot\vec{r}}, \tag{2.15}$$

with $\vec{r} = x\hat{x} + y\hat{y} + z\hat{z}$ as the position vector. Using the standard engineering notation for electromagnetic field propagation, the negative sign is apart of the exponential function and thus the components of the wave vector are positive or negative such that waves decay with distance.

Finally, for a uniform plane wave there is a specified relationship between the electric and magnetic fields such that

$$\vec{H} = \frac{\vec{k} \times \vec{E}}{\omega\mu}. \tag{2.16}$$

2.2 Reflection and Transmission at Planar Interfaces

Understanding plane wave propagation in unbounded, linear, homogeneous, and isotropic media is the first step in understanding what happens when plane waves are incident on a planar interface. A half-space geometry is initially discussed for oblique and normal incidence. Reflection off of multiple layers is discussed in Section 2.3.

2.2.1 Oblique Incidence

Consider an interface at $z = 0$ between two different different material mediums as in Figure 2.1; material 1 extends infinitely in the $-\hat{z}$ direction and material 2 extends infinitely into the $+\hat{z}$ direction. The plane wave originates in material 1 and is incident on material 2 at an angle θ_i. The incidence angle, θ_i, is between $0-90^\circ$ and is measured from the normal vector of the interface.

An important aspect of the geometry is the plane of incidence. The plane of incidence is the plane in which the wave vector lies. For example, if the wave vector is in the $\hat{x}$ and $\hat{z}$ directions the plane of incidence is the xz-plane. Figures 2.3 and 2.2 diagram the plane of incidence in relationship to the interface between the two materials for parallel and perpendicular polarization respectively.

For simplicity, plane wave reflection at oblique incidence is broken into two different cases: (1) transverse magnetic polarization and (2) transverse electric polarization. Any other arbitrary polarization is a linear combination of transverse magnetic and transverse electric polarizations.

What is of specific interest for this work is the definition of the wave or field impedance in both materials 1 and 2 and the interfacial reflection coefficient defined for both transverse magnetic and electric polarizations. The wave impedance is defined as the ratio of the electric and magnetic fields in planes parallel to the boundary [46]. For instance, if the interface between material 1 and 2 is in the xy-plane, the ratio of the appropriate x and y the components of electric and magnetic fields are computed. The wave impedance is defined in this manner because of the continuity of the tangential electric and magnetic fields across the boundary. Once the wave impedance is defined, the reflection coefficient can be calculated with the well known formula

$$R = \frac{Z_2 - Z_1}{Z_2 + Z_1}, \tag{2.17}$$

where Z_1 is the wave impedance in material 1 and Z_2 is the wave impedance in material 2.

Transverse Magnetic Polarization

Transverse magnetic (TM) polarization is when the magnetic field is perpendicular to the plane of incidence and the electric field lies in the plane of incidence. TM polarization is also often referred to as parallel polarization. The incident, reflected, and transmitted electric and magnetic fields are

$$\vec{E}_i(x,z) = E_{i\circ}\left(\frac{k_z^i}{k_1}\hat{x} - \frac{k_x^i}{k_1}\hat{z}\right)e^{-\jmath k_1(k_x^i x + k_z^i z)} \tag{2.18}$$

$$\vec{H}_i(x,z) = \hat{y}\frac{E_{i\circ}}{\eta_1}e^{-\jmath k_1(k_x^i x + k_z^i z)} \tag{2.19}$$

$$\vec{E}_r(x,z) = E_{r\circ}\left(\frac{k_z^r}{k_1}\hat{x} + \frac{k_x^r}{k_1}\hat{z}\right)e^{-\jmath k_1(k_x^r x + k_z^r z)} \tag{2.20}$$

$$\vec{H}_r(x,z) = \hat{y}\frac{E_{r\circ}}{\eta_1}e^{-\jmath k_2(k_x^r x + k_z^r z)} \tag{2.21}$$

$$\vec{E}_t(x,z) = E_{t\circ}\left(\frac{k_z^t}{k_2}\hat{x} - \frac{k_x^t}{k_2}\hat{z}\right)e^{-\jmath k_2(k_x^t x + k_z^t z)} \tag{2.22}$$

$$\vec{H}_t(x,z) = \hat{y}\frac{E_{t\circ}}{\eta_2}e^{-\jmath k_2(k_x^t x + k_z^t z)} \tag{2.23}$$

where $\eta_1 = \sqrt{\frac{\mu_1}{\epsilon_1}}$ and $\eta_2 = \sqrt{\frac{\mu_2}{\epsilon_2}}$ are the *intrinsic* impedances in materials 1 and 2 respectively [24]. Take note that the intrinsic impedance is different from the wave impedance; the intrinsic impedance is due to physical properties of the material and the wave impedance is the ratio of particular components of the electric and magnetic fields.

For TM polarization, the wave impedance is calculated with the $\hat{x}$-component of the electric field and the $\hat{y}$-component of the magnetic field. For the fields in material 1, either the ratio the of incident electric and magnetic fields *or* the ratio of the reflected electric and magnetic fields may be used to calculate the wave impedance. In consequence, the wave impedance in medium 1 using equations (2.18)-(2.19) is $Z_1^{\parallel} = \eta_1\frac{k_z^i}{k_1}$. Using Figure 2.5, it is customary to rewrite the $\frac{k_z^i}{k_1}$ term in terms of the incidence angle such that

$$Z_1^{\parallel} = \eta_1\cos\theta \tag{2.24}$$

where θ_i is equal to θ_r due to Snell's law of Reflection. The wave impedance for the medium 2 is simply

$$Z_2^{\parallel} = \eta_2 \frac{k_z^t}{k_2}. \tag{2.25}$$

The interfacial reflection coefficient for TM polarization is then computed using equations, (2.17), (2.24), and (2.25).

Transverse Electric Polarization

Transverse electric (TE) polarization is when the electric field is perpendicular to the plane of incidence and the magnetic field lies in the plane of incidence. TE polarization is also often referred to as perpendicular polarization. The incident, reflected, and transmitted electric and magnetic fields are

$$\vec{E}_i(x,z) = \hat{y}E_{i\circ}e^{-\jmath k_1(k_x^i x + k_z^i z)} \tag{2.26}$$

$$\vec{H}_i(x,z) = \frac{E_{i\circ}}{\eta_1}\left(-\frac{k_z^i}{k_1}\hat{x} + \frac{k_x^i}{k_1}\hat{z}\right)e^{-\jmath k_1(k_x^i x + k_z^i z)} \tag{2.27}$$

$$\vec{E}_r(x,z) = \hat{y}E_{i\circ}e^{-\jmath k_1(k_x^r x + k_z^r z)} \tag{2.28}$$

$$\vec{H}_r(x,z) = \frac{E_{r\circ}}{\eta_1}\left(\frac{k_z^r}{k_1}\hat{x} + \frac{k_x^r}{k_1}\hat{z}\right)e^{-\jmath k_1(k_x^r x + k_z^r z)} \tag{2.29}$$

$$\vec{E}_t(x,z) = \hat{y}E_{t\circ}e^{-\jmath k_2(k_x^t x + k_z^t z)} \tag{2.30}$$

$$\vec{H}_t(x,z) = \frac{E_{t\circ}}{\eta_2}\left(-\frac{k_z^t}{k_2}\hat{x} + \frac{k_x^t}{k_2}\hat{z}\right)e^{-\jmath k_2(k_x^t x + k_z^t z)}. \tag{2.31}$$

Again η_1 and η_2 are the intrinsic impedances in materials 1 and 2 respectively. For TE polarization, the wave impedance is calculated with the $\hat{y}$-component of the electric field and the $\hat{x}$-component of the magnetic field. The wave impedance in medium 1 using equations (2.26)-(2.27) is $Z_1^{\perp} = \eta_1 \frac{k_1}{k_z^i}$. Using Figure 2.4, it is customary to rewrite the $\frac{k_z^i}{k_1}$ term in terms of the incidence angle such that

$$Z_1^{\perp} = \frac{\eta_1}{\cos\theta}. \tag{2.32}$$

The wave impedance for the medium 2 is

$$Z_2^{\perp} = \eta_2 \frac{k_2}{k_z^t}. \tag{2.33}$$

The interfacial reflection coefficient for TE polarization is then computed using equations, (2.17), (2.32), and (2.33).

2.2.2 Normal Incidence

A special case of oblique incidence is normal incidence. Normal incidence is when the wave vector is perpendicular to the interface between medium 1 and medium 2 and $\theta_i = 0^\circ$. Plugging $\theta_i = 0^\circ$ into equations (2.24), (2.25), (2.32), (2.33) yields:

$$Z_1^{\parallel} = Z_1^{\perp} = \eta_1, \tag{2.34}$$

$$Z_2^{\parallel} = Z_2^{\perp} = \eta_2. \tag{2.35}$$

2.3 Reflection and Transmission at Layered Slabs

Many reflection-only material characterization methods make use of stacked layers of materials as in Figure 2.6. In these cases, the interfacial reflection coefficients do not account for the measured reflection coefficient for the entire material stack. The reflection coefficient measured due to a layered stack of materials is termed the *global* reflection coefficient and denoted with the Greek letter Γ.

The global reflection coefficient accounts for the multiple reflection and transmissions which occur between the interfaces of the materials. For example, consider a stack of two layered materials as in Figure 2.6. A plane wave is incident on the interface 0; at interface 0 some of the wave will be reflected and some of the wave will be transmitted. This same process will also occur at interface 1 with the incident wave being the original *transmitted* wave at interface 0. The reflected wave from interface 1 will then be a secondary *incident* wave on interface 2. The multiple reflections and transmissions will continue to occur until there is sufficient decay of the waves.

There are several methods which can be used to derive the global reflection coefficient which include using boundary conditions, recursion [16], and the wave matrix method [11]. The wave matrix represents each layer of the material stack with an individual 2×2 matrix called a transmission matrix. Denoting forward moving waves with c_j and backward moving waves with b_j (with j being the j^{th} material layer), the initial step in calculating the global reflection coefficient is utilizing

$$\begin{bmatrix} c_0 \\ b_0 \end{bmatrix} = \prod_{j=1}^{n} \frac{1}{T_j} \begin{bmatrix} e^{\jmath k_z^j \delta_j} & R_j e^{-\jmath k_z^j \delta_j} \\ R_j e^{-\jmath k_z^j \delta_j} & e^{\jmath k_z^j \delta_j} \end{bmatrix} \begin{bmatrix} c_{j+1} \\ b_{j+1} \end{bmatrix} \tag{2.36}$$

where T_j and δ_j are the interfacial transmission coefficient and thickness of the j^{th} material in the stack.

The global reflection coefficient is the ratio of the backward and forward going waves at the first interface, $\frac{b_0}{c_0}$. Thus, equation (2.36) is solved for c_0 and b_0 and the ratio is taken of the two terms.

Three specific forms of the reflection coefficient are vital in this work: (1) a single material backed by air (2) a single material backed by a conductor, and (3) two material stacks backed by a conductor. For a material backed by free-space or another dielectric (medium 2 is backed by air in Figure 2.6), the global reflection coefficient is

$$\Gamma = \frac{R_1(1-P^2)}{1-R_2^2P^2}. \tag{2.37}$$

For a material backed by a conductor (medium 2 is a conductor in Figure 2.6), the global reflection coefficient is

$$\frac{R_1-P^2}{1-R_1^2P^2}. \tag{2.38}$$

Lastly, for two material layers backed by a conductor (medium 2 is backed by a conductor in Figure 2.6), the global reflection coefficient is

$$\Gamma = \frac{R_1+R_2P_1^2-P^1P^2-R_1R_2P_2^2}{1+R_1R_2P_1^2-R_1P_1^2P_2^2-R_2P_2^2}. \tag{2.39}$$

In equations (2.37)-(2.39), P_j are the propagation factors through a material layer and is defined as $e^{-jk_z^jz}$. Also, R_j are the interfacial reflection coefficients between the material layers.

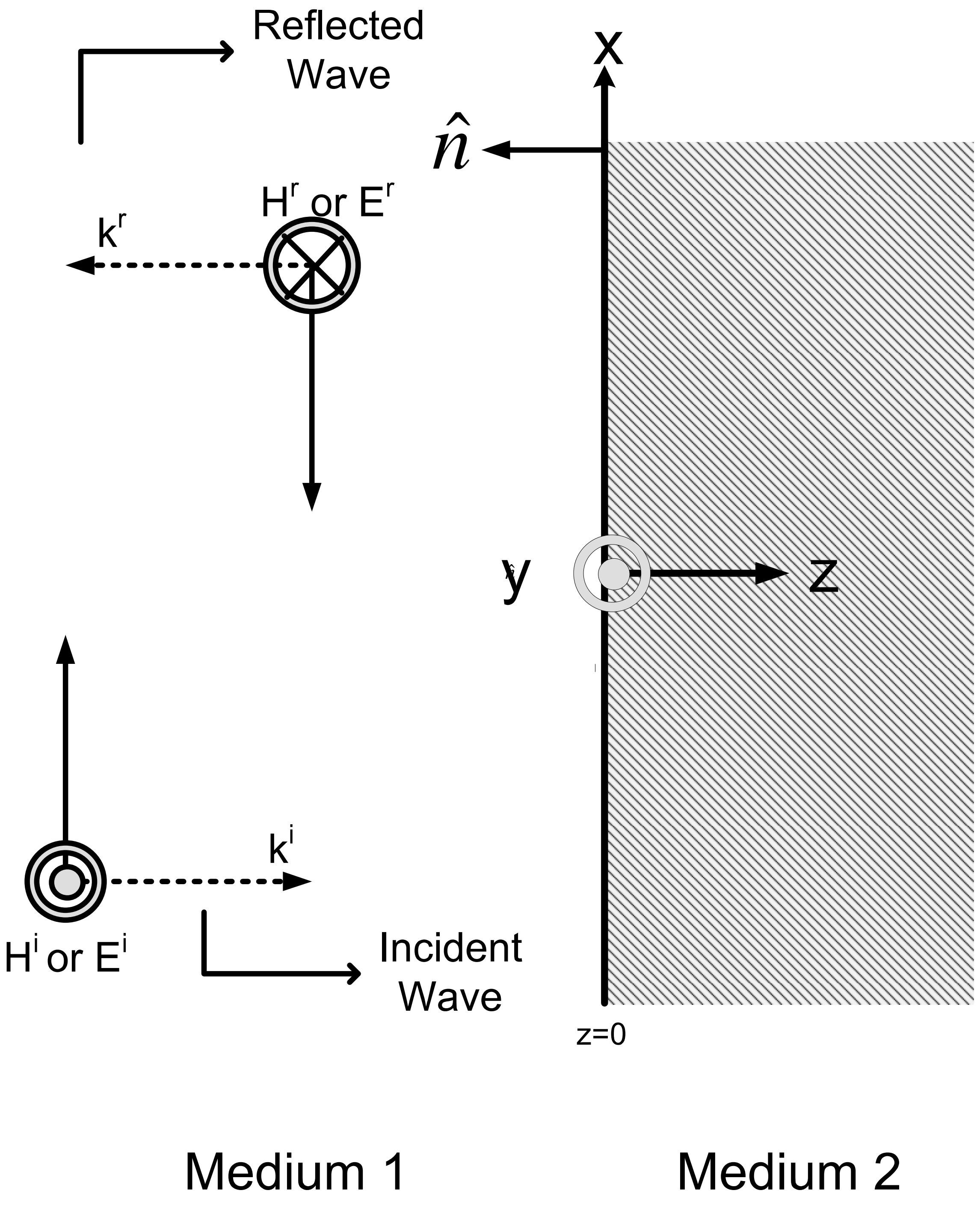

Figure 2.1: Geometry of the canonical problem of plane wave incidence on a planar slab

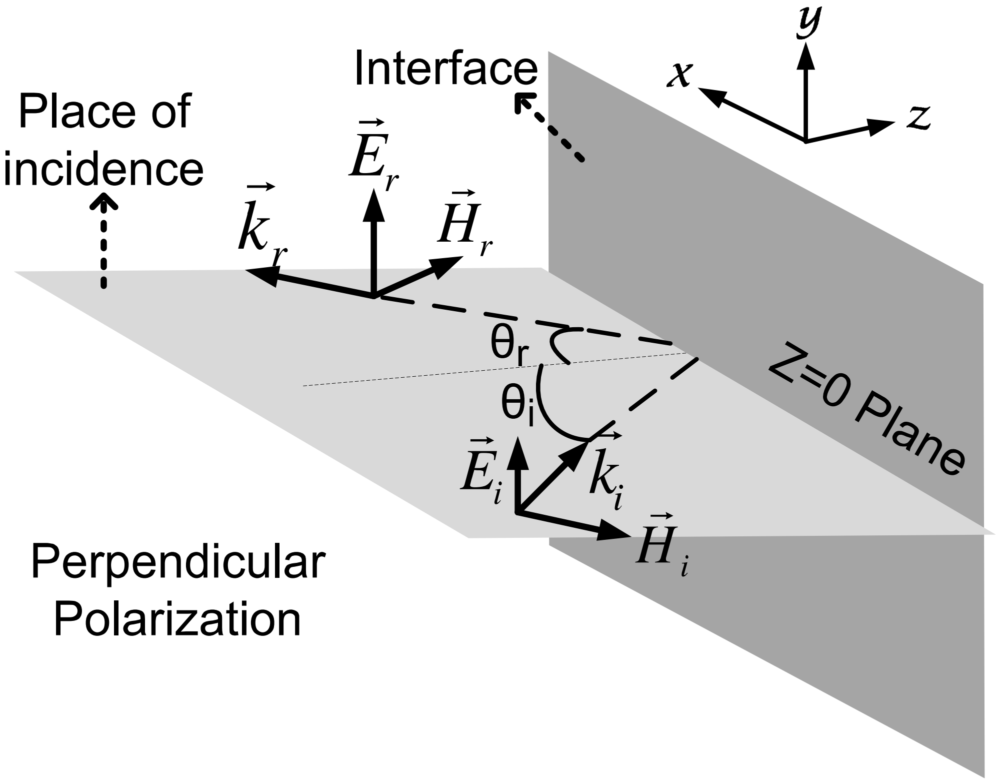

Figure 2.2: Illustration of the plane of incidence with perpendicular polarization

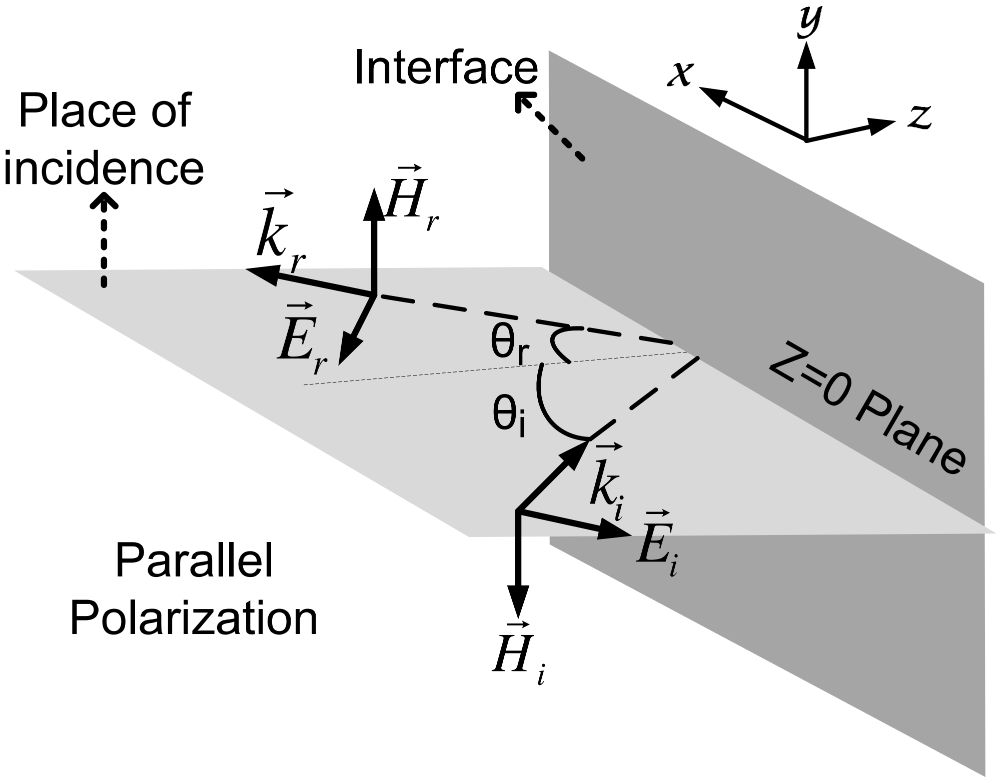

Figure 2.3: Illustration of the plane of incidence with parallel polarization

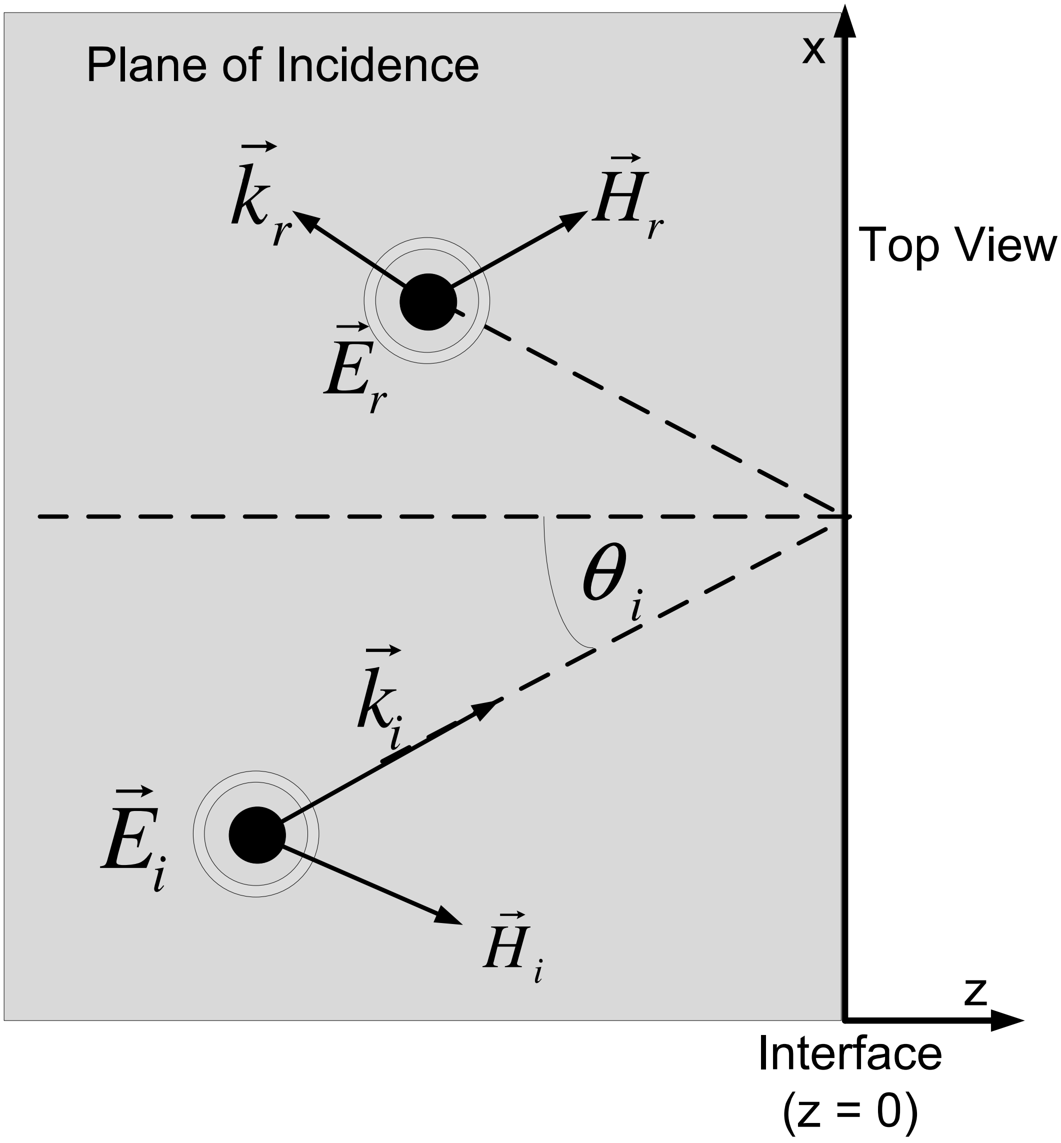

Figure 2.4: Resolution of incident wave vector and electric field of components with perpendicular polarization

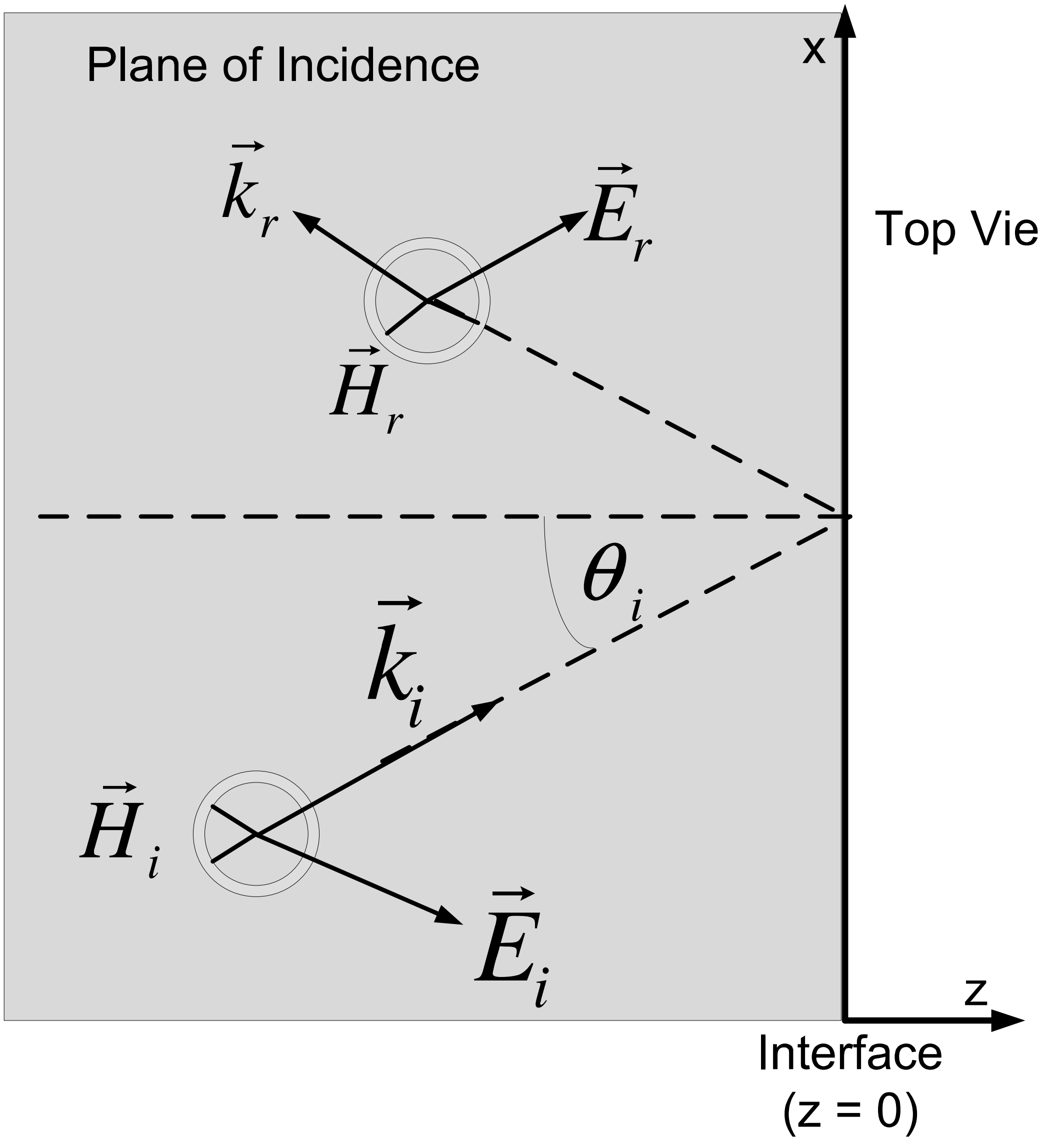

Figure 2.5: Resolution of incident wave vector and electric field of components with parallel polarization

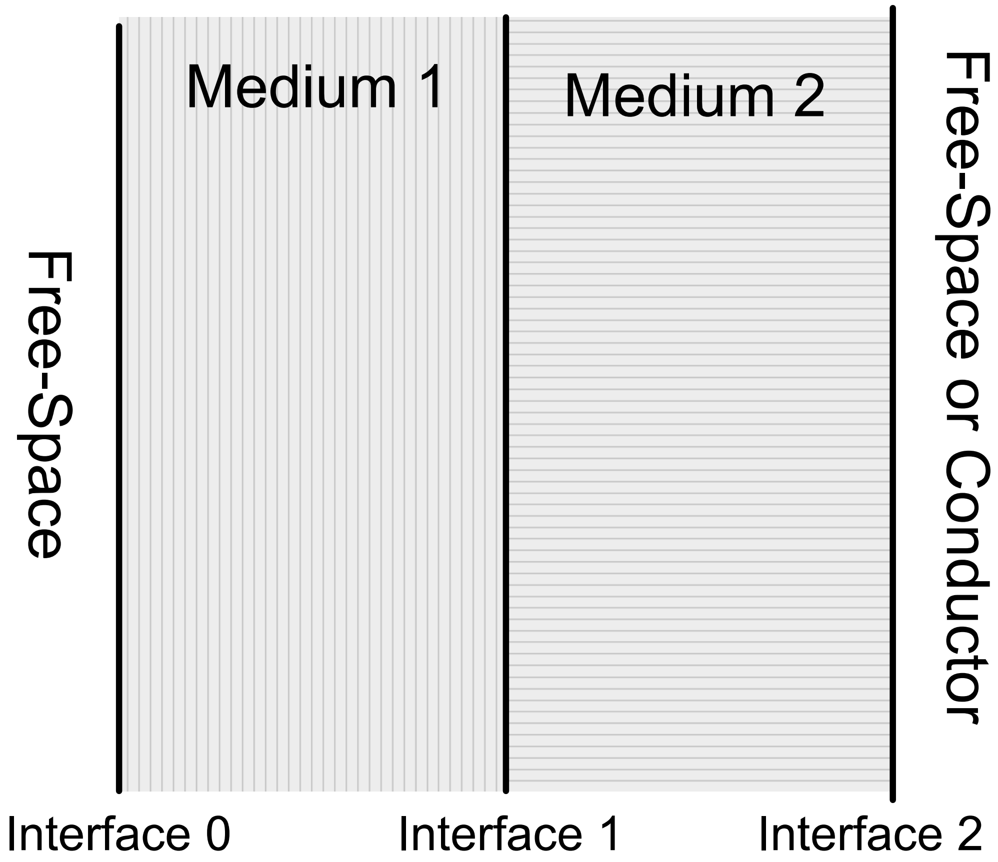

Figure 2.6: Diagram of stacked media

Chapter 3

Overview of Error Analysis Methods

3.1 The Importance of Error Analysis

The science of the measurement of errors is a branch of metrology, the science of measurement [45]. From [53], error analysis is defined as the study and evaluation of uncertainty in measurement. A scientific experiment cannot be concluded until an analysis of the uncertainty in the final result has been conducted [23]. Also, [23] tells us that error analysis seeks to answer the following questions:

1. Do the results agree with theory?
2. Are the results reproducible?
3. Has a new effect or phenomena been observed?

Throughout this work, and in general uncertainty analysis, the term *error* is used frequently. To be clear on the use of the term *error*, [53] gives an excellent definition. Stated concisely, Taylor says that errors are not mistakes or blunders, but inevitable uncertainties which acculminate in the measurement process. Thus, the term *error* is synonymous with *uncertainty*.

Error analysis is an extremely important aspect of material characterization. In perspective of the many applications of material characterization, some of which are listed in Chapter 2, the level of certainty in the extracted permittivity and permeability is paramount. Error analysis in material characterization has included the study of the effect of temperature [8], calibration liquids [41], numerical techniques [40], propagation of high order modes [12], and air gaps in material samples [55] on the reliability of the characterization process.

The intent of this chapter is to expound upon the error analysis methods utilized in this work. In addition, an overview of types of uncertainty, interpretation of uncertainty, and the normal distributed are presented.

3.2 Uncertainties in Measurement

Rabinovich in [45] defines a measured quantity or *measurand* as "a property of phenomena, bodies, or substances that can be described qualitatively and expressed quantitatively." Measurement is the process of determining the value of a physical quantity. The *true value of the measurand* is the known measured quantity which most accurately reflects qualitatively and quantitatively the corresponding property of the object. Thus, the *measurement error* is deviation of the measured measurand and the true value from the measurand.

Uncertainties or errors in measurements arise from various sources. For example, errors can arise from misreading measurement scales, improper calibration of equipment, and equipment malfunction. As with the measurement methods discussed in this work, several measurement instruments are used to arrive to a single result. Since each instrument has its own precision capabilities, there is an inherent uncertainty in the final result. Therefore, the uncertainties in the multiple instruments are said to *propagate* into the final result. Knowing the extent the instrument uncertainties propagate into a result is essential to knowing the degree to which the result can be trusted.

Measurement error can be expressed in two distinct ways. One way of expressing measurement error is to use relative error. Relative error expresses the measurement uncertainty as a fraction or percentage of the true value. Absolute error expresses measurement uncertainty as positive or negative bounds relative to the true value. The absolute error notation is mostly used in this work. Therefore, when a measurement result is presented, it is presented as the best estimate of the measurand plus or minus the measurement error like

$$measurement\,of\,quantity\,x = x_{best} \pm \sigma. \tag{3.1}$$

Here x_{best} is the best estimate of quantity x and σ provide the confidence bounds for x_{best}. It is important to note that $\pm\sigma$ is regarded as a statement of probability for the values of x [23].

3.2.1 Types of Measurement Uncertainty

There are two categories of error in the measurement process. One type of error is systematic error and the second type is random error. Systematic errors are reproducible inaccuracies which consistently influence the experiment in the same manner. Sources of systematic error may be imperfect calibration of measurement instruments, changes in the environment which interfere with the measurement process, or imperfect scales on measurement instruments.

Random errors are uncertainties that lead to inconsistencies in repeated measurements. Random errors are inherently unpredictable and have null arithmetic mean. Examples of sources of random error include unpredictable fluctuations in the readings of measurement instruments or in the experimenter's interpretation of the instrumental readings. Figure 3.1 graphically shows the difference between systematic and random errors.

Systematic errors are very hard to detect because their source is often embedded within measurement instruments or measurement processes. Therefore, systematic errors are unique to a specific experiment. In contrast, random errors are present within every experiment and can be predicted with knowledge of the instrument tolerances in the experiment. Thus, random errors are the focus of this work.

3.2.2 The Normal Distribution

In view that all measurements contain uncertainty due to random error, there is inherently some spread or variability is measurement outcomes. In order to describe the spread of measurement outcomes, probability distributions are essential. The relationship between random variables and the probability distributions which describe them are the fundamental study of probability theory and statistics. The purpose of the probability distribution is to show the range of possible random variable values and their probability of occurrence.

Random variables can either be discrete or continuous. Discrete random variables can be finite set of values or an infinite sequence of values. Conversely, continuous random variables can take on any value in an interval. Due to the types of measurements considered in this work, only continuous random variables will be examined.

In view of the statistical analysis needed for error analysis, there is a need for defining a probability distribution for this work. In order to perform the error analysis, an assumption of the distribution of the permittivity and permeability must be made. The distribution does not need to be the best-fitting distribution for the permittivity and permeability, but adequate enough such that statistical techniques yield valid conclusions. A common distribution to use in science and engineering is the normal distribution. The normal distribution is a very important statistical data representation and appropriate to represent many natural phenomena. Hence, the normal distribution represents the distribution of permittivity and permeability in this work.

The plot of a normal distribution is a symmetric bell-curve as in Figure 3.2. The center of the normal distribution is the mean or best estimate of the experiment, and the standard deviation of the data represents the spread of the curve. In addition, the data represented by the normal distribution follows the 64-95-99.7 rule; this rule means that 64% of the data in the normal distribution will lie within two standard deviations of the mean, 95% of the data will lie within three standard deviations of the mean, and 99.7% of the data will lie within four standard deviations of the mean.

3.3 Calculating Measurement Error

To define the normal distribution of the permittivity and permeability, the statistical mean and the standard deviation must be determined. In this work, two methods to determine the standard derivation are implemented - Monte Carlo simulations and the error propagation method. This section will provide an overview of both methods.

3.3.1 Overview of Monte Carlo Simulations

Monte Carlo simulations are a class of computational algorithms that use repeated random sampling to compute results. Monte Carlo simulations are named after the famous casino in Monte Carlo from the 1940's. Monte Carlo simulations are used for a variety of applications such as, but not limited to, computational physics, physical chemistry, and computational biology.

In addition to the applications listed above, Monte Carlo simulations are widely used for error analysis. The Monte Carlo simulation algorithm proceeds as follows:

1. Define a domain of possible inputs.
2. Generate a set of pseudo-random numbers over the domain.
3. Perform a deterministic computation on the inputs.
4. Aggregate the results (i.e. - calculate the standard deviation).

Positive attributes of Monte Carlo simulations are that they are easy to implement and finding the probability of multi-variable functions is simple. Drawbacks of Monte Carlo simulations are that they can be computationally heavy (hundreds of thousands of trials are necessary for high accuracy) and it is difficult to attain functional behavior over a range of inputs.

3.3.2 Overview of the Error Propagation Method

The error propagation is a method that allows for calculation of the standard deviation of a quantity that is dependent on other measurements. For example, suppose calculation of a hypothetical quantity A is desired. The calculation of A is dependent on the measurement of quantities x,y, and z. However, quantities x,y, and z have their own uncertainties σ_x, σ_y, and σ_z. Therefore, A will have inherent uncertainty due to the uncertainties in x,y, and z.

The error propagation method represents the potential change in the quantity A due to the uncertainties in x,y, and z with the first derivative of A with respect to x,y, and z. The formula for the standard deviation of A due to the uncertainties in *independent* quantities x,y, and z is the quadrature formula

$$\sigma_A = \sqrt{\sigma_x^2 \left(\frac{\partial A}{\partial x}\right)^2 + \sigma_y^2 \left(\frac{\partial A}{\partial y}\right)^2 + \sigma_z^2 \left(\frac{\partial A}{\partial z}\right)^2}. \tag{3.2}$$

For a complete derivation of the error propagation method, the reader is encouraged to read [53].

The error propagation method advantages include being able to calculate the standard deviation over a range or interval and the ability to use the equations to infer mathematical and physical weaknesses in a method. Disadvantages of the error propagation method include calculations which involve dependent variables, possible issues with calculating the derivative, ignoring higher order derivatives, and properly implementing the correct rules for quotients, products, and the like. Also, the error propagation method suffers when the derivatives vary rapidly. When this occurs, an overestimation of the standard deviation is encountered because the assumption that the standard deviation of the input variables is very close to to the change in the derivative is no longer valid.

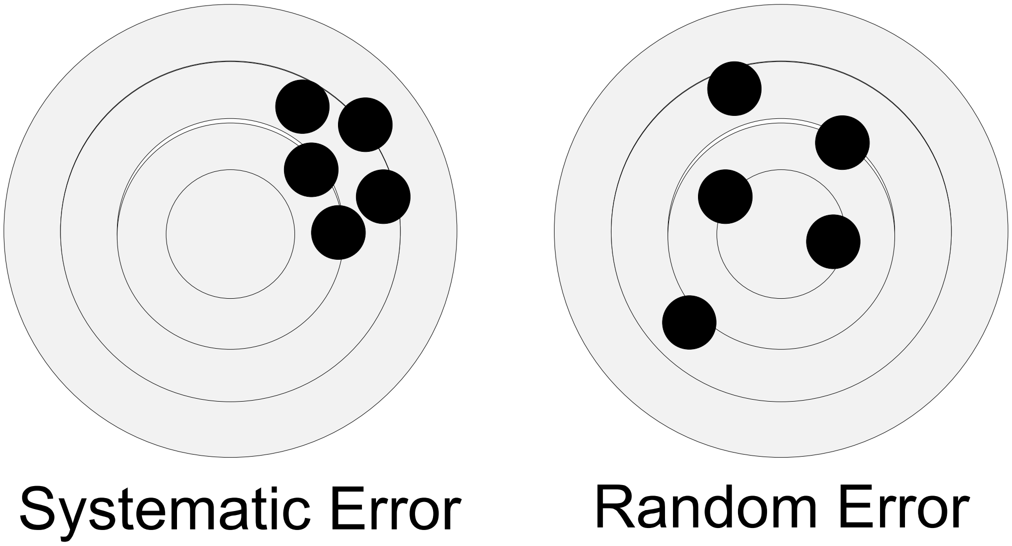

Figure 3.1: Drawing emphasizing the difference between systematic and random errors

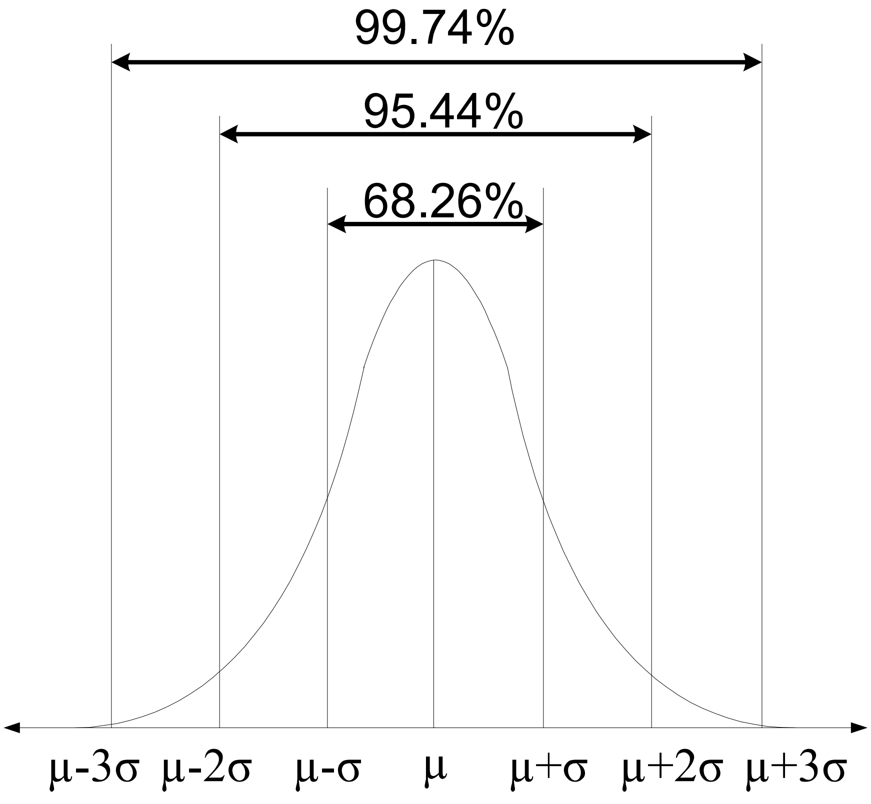

Figure 3.2: Sample plot of the normal distribution

Chapter 4

General Formulation of Reflection-Only Material Characterization Methods

4.1 Introduction

Over time many different formulations of reflection-only characterization methods have become available in the literature, each method having its own set of extraction equations. The purpose of this chapter is to derive and demonstrate a unifying set of extraction equations for most reflection-only material characterization methods. Analysis of the interfacial transverse impedance of a generic free-space arrangement of materials allows for derivation of the unifying set of extraction equations.

Two independent measurements are required to determine the parameters μ and ϵ for any material characterization method. In the case of reflection-only characterization methods, two independent *reflection* measurements must be made. Several approaches have been investigated for obtaining these two measurements, including the

1. *Conductor/Air Backed Method*

2. *Layer-shift method*

3. *Two-thickness method.*

Simultaneous observation of all three reflection-only approaches reveals that all of these reflection-only methods are variations of one single scheme. Analysis of this single scheme reveals a powerful formulation which unifies **many reflection-only material characterization methods**. The extraction equations are evaluated on several different reflection-only arrangements utilizing measured data. The permittivity and permeability extracted with the unifying methodology compare very well to those found using widely-accepted material characterization methods. The unifying extraction equations shown in this chapter systemize most reflection-only methods and provide a common starting point for comparison and analysis. Thus, a common resource for all extraction equations for μ and ϵ has been developed.

4.2 A General Approach to Overlays and Underlays

The geometry of any reflection-only material characterization method may be described using a subset of the arranged overlays and underlays shown in Figure 4.1. In a free-space system, a plane wave originates in free-space, region 0, and is incident on an overlay, region 1. In a guided-wave system (waveguide or TEM), the wave originates in an empty section of guide and is incident on the overlay. The overlay is assumed to be inhomogeneous, with arbitrary z-dependent permittivity and permeability profiles $\epsilon_1(z)$ and $\mu_1(z)$. Region 1 can represent an assortment of formations including a layering of different homogenous materials or layers of spatially-varying materials. The overlay is stacked against region 2, which is the homogeneous MUT with parameters μ_2 and ϵ_2. Finally, the material under test (MUT) is backed by an underlay, region 3, which has inhomogeneous permittivity and permeability profiles $\epsilon_3(z)$ and $\mu_3(z)$, and thus has all of the same potential formations as region 1.

The process for obtaining the formulas for μ and ϵ is slightly different with a free space system than with the guided-wave systems, since the incident wave in a free-space system has an arbitrary angle of incidence and polarization. Thus, these two cases are considered in separate sections.

4.2.1 Free-space system

TM Polarization

Assume that the incident plane wave is polarized either perpendicular to the plane of incidence (TE) or parallel to the plane of incidence (TM). For the case of TM illumination there is a y-component of $\vec{H}$ but not of $\vec{E}$. Since the fields cannot depend on y, only the fields H_y, E_x, and E_z are non-zero, and these must obey Faraday's law

$$\frac{\partial E_x(x,y)}{\partial z} - \frac{\partial E_z(x,z)}{\partial x} = -j\omega\mu(z) H_y(x,z), \tag{4.1}$$

and Ampere's law

$$\begin{aligned} -\frac{\partial H_y(x,z)}{\partial z} &= j\omega\epsilon(z) E_x(x,z) && (4.2)\\ \frac{\partial H_y(x,z)}{\partial x} &= j\omega\epsilon(z) E_z(x,z). && (4.3) \end{aligned}$$

Substituting (4.2) and (4.3) into (4.1) gives the wave equation for H_y [20]:

$$\left\{ \frac{\partial^2}{\partial x^2} + \frac{\partial^2}{\partial z^2} - \frac{\epsilon'}{\epsilon}\frac{\partial}{\partial z} + k^2 \right\} H_y(x,z) = 0, \tag{4.4}$$

where $k^2(z) = \omega^2\mu(z)\epsilon(z)$ and $\epsilon'(z) = d\epsilon(z)/dz$. Substituting the product solution

$$H_y(x,z) = \chi(x)\zeta(z) \tag{4.5}$$

leads to the separated equations

$$\left\{ \frac{d^2}{dx^2} + k_x^2 \right\} \chi(x) = 0, \tag{4.6}$$

$$\left\{ \frac{d^2}{dz^2} - \frac{\epsilon'(z)}{\epsilon(z)} \frac{d}{dz} + k_z^2(z) \right\} \zeta(z) = 0, \tag{4.7}$$

where $k_x^2 + k_z^2(z) = k^2(z)$. The solution to (4.6) is simply

$$\chi(x) = \mathrm{e}^{\pm j k_x x}. \tag{4.8}$$

Note that in order to satisfy the boundary conditions for all x, $k_x = k_{x0} = k_0 \sin\theta_0$ in all regions.

The form of the solution to (4.7) depends on the profile $\epsilon(z)$, but can always be written as the sum of two independent solutions to the second-order equation, $f(z)$ and $g(z)$. Thus,

$$H_y(x,z) = \left[A f(z) + B g(z) \right] \mathrm{e}^{-j k_{x0} x}. \tag{4.9}$$

Defining $\Gamma = -B/A$, H_y can be written as

$$H_y(x,z) = A \left[f(z) - \Gamma g(z) \right] \mathrm{e}^{-j k_{x0} x} \tag{4.10}$$

while E_x is given from (4.2) as

$$E_x(x,z) = \frac{j}{\omega \epsilon(z)} A \left[f'(z) - \Gamma g'(z) \right] \mathrm{e}^{-j k_{x0} x}. \tag{4.11}$$

From these the transverse impedance is defined as

$$Z(z) = \frac{E_x(x,z)}{H_y(x,z)} = \frac{j}{\omega \epsilon(z)} \frac{f'(z) - \Gamma g'(z)}{f(z) - \Gamma g(z)}. \tag{4.12}$$

The transverse impedance is easily specialized to each region in figure 4.1. In region 0, $f(z) = \mathrm{e}^{-j k_{z0} z}$ and $g(z) = \mathrm{e}^{j k_{z0} z}$, where $k_{z0} = k_0 \cos\theta_0$. Using these in (4.12), gives

$$Z_0(z) = Z_0 \frac{\mathrm{e}^{-j k_{z0} z} + \Gamma_0 \mathrm{e}^{j k_{z0} z}}{\mathrm{e}^{-j k_{z0} z} - \Gamma_0 \mathrm{e}^{j k_{z0} z}}, \tag{4.13}$$

with

$$Z_0 = \eta_0 \cos\theta_0. \tag{4.14}$$

Here Γ_0 is the ratio of the transverse components of the electric field at the $z = 0$ interface; *this is the reflection coefficient that is measured in the experiment.* In region 2, the MUT material is homogeneous, and so $f(z) = \mathrm{e}^{-jk_{z2}z}$ and $g(z) = \mathrm{e}^{jk_{z2}z}$, where $k_{z2} = \sqrt{k_2^2 - k_0^2 \sin^2\theta_0}$. Thus,

$$Z_2(z) = Z_2 \frac{\mathrm{e}^{-jk_{z2}z} + \Gamma_2 \mathrm{e}^{jk_{z2}z}}{\mathrm{e}^{-jk_{z2}z} - \Gamma_2 \mathrm{e}^{jk_{z2}z}}, \tag{4.15}$$

where

$$Z_2 = \frac{k_{z2}}{\omega\epsilon_2}. \tag{4.16}$$

Here the parameter Γ_2 must be determined by applying boundary conditions.

Regions 1 and 3 are potentially inhomogeneous, and thus the forms of $f(z)$ and $g(z)$ depend on the material parameter profiles $\epsilon(z)$ and $\mu(z)$. In order to determine the parameters Γ_1, Γ_2, and Γ_3, the boundary conditions on tangential fields must be applied at $z = 0$, $z = z_1$ and $z = z_3$. Continuity of both tangential electric and tangential magnetic fields may be achieved by enforcing continuity of transverse impedance. For TM illumination, $Z_0(0) = Z_1(0)$ produces

$$Z_0 \frac{1+\Gamma_0}{1-\Gamma_0} = \frac{j}{\omega\epsilon_1(0)} \frac{f'(0) - \Gamma_1 g_1'(0)}{f_1(0) - \Gamma_1 g_1(0)}. \tag{4.17}$$

This can be solved for Γ_1:

$$\Gamma_1 = \frac{W f_1(0) - f_1'(0)}{W g_1(0) - g_1'(0)}, \tag{4.18}$$

where

$$W = -j\omega\epsilon_1(0) Z_0 \frac{1+\Gamma_0}{1-\Gamma_0}. \tag{4.19}$$

Since the properties of the overlay (region 1) are known and the reflection coefficient Γ_0 is measured, Γ_1 is a known quantity. Next, the boundary condition $Z_1(z_1) = Z_2(z_1)$ produces

$$Z_1(z_1) = \mathrm{Z}_2 \frac{\mathrm{e}^{-jk_{z2}z_1} + \Gamma_2 \mathrm{e}^{jk_{z2}z_1}}{\mathrm{e}^{-jk_{z2}z_1} - \Gamma_2 \mathrm{e}^{jk_{z2}z_1}}. \tag{4.20}$$

Here

$$Z_1(z_1) = \frac{j}{\omega\epsilon_3(z_1)} \frac{f_1'(z_1) - \Gamma_1 g_1'(z_1)}{f_1(z_1) - \Gamma_1 g_1(z_1)} \tag{4.21}$$

is a known quantity, since Γ_1 is known from (4.18). Finally, implementing $Z_2(z_2) = Z_3(z_2)$ results in

$$Z_3(z_2) = \mathrm{Z}_2 \frac{\mathrm{e}^{-jk_{z2}z_2} + \Gamma_2 \mathrm{e}^{jk_{z2}z_2}}{\mathrm{e}^{-jk_{z2}z_2} - \Gamma_2 \mathrm{e}^{jk_{z2}z_2}}. \tag{4.22}$$

Here

$$Z_3(z_2) = \frac{j}{\omega\epsilon_3(z_2)} \frac{f_3'(z_2) - \Gamma_3 g_3'(z_2)}{f_3(z_2) - \Gamma_3 g_3(z_2)} \tag{4.23}$$

is a known quantity, since the properties of the underlay (region 3) are known. Solving for Γ_2 and substituting into (4.15) gives

$$Z_2(z) = \mathrm{Z}_2 \frac{Z_3(z_2) + j\mathrm{Z}_2 \tan k_{z2}(z_2 - z)}{jZ_3(z_2) \tan k_{z2}(z_2 - z) + \mathrm{Z}_2}. \tag{4.24}$$

Using this in the boundary condition $Z_1(z_1) = Z_2(z_1)$ then gives

$$Z_1(z_1) = \mathrm{Z}_2 \frac{Z_3(z_2) + j\mathrm{Z}_2 \tan k_{z2}\delta}{jZ_3(z_2) \tan k_{z2}\delta + \mathrm{Z}_2}, \tag{4.25}$$

where $\delta = z_2 - z_1$ is the MUT thickness.

Equation (4.25) is a key result. For a given θ_0, $Z_1(z_1)$ is determined entirely by the properties of the overlay, and $Z_3(z_2)$ is determined entirely by the properties of the underlay. Thus, the following important observation is clear: *if two measurements are made with different overlays, exactly the same information is present in (4.25).* Since two independent measurements cannot be made, ϵ_2 and μ_2 cannot be recovered, and so no technique that relies on altering the overlay can be successful. This is in contrast to material characterization using waveguide probes, where altering the overlay has been successfully employed to determine both ϵ and μ [38]. This result was initially demonstrated in [2].

In contrast, if two measurements are made with different known arrangements of the underlay, the two values of (4.25) provide sufficient information to find ϵ_2 and μ_2. In fact, these parameters may be determined in closed form regardless of the configurations of the underlay. Note that since an overlay is not helpful in measuring the parameters of the MUT, it may be prudent to perform measurements with no overlay present. This special case may be easily implemented by setting $Z_1(z_1) = Z_0(0)$, or

$$Z_1(z_1) = \mathrm{Z}_0 \frac{1+\Gamma_0}{1-\Gamma_0}. \tag{4.26}$$

TE Polarization

For the case of TE illumination, only the field components H_x, H_z, and E_y are nonzero; these must obey Ampere's law

$$\frac{\partial H_x(x,y)}{\partial z} - \frac{\partial H_z(x,z)}{\partial x} = j\omega\epsilon(z)E_y(x,z) \tag{4.27}$$

and Faraday's law

$$\begin{aligned} \frac{\partial E_y(x,z)}{\partial z} &= j\omega\mu(z)H_x(x,z) && (4.28)\\ -\frac{\partial E_y(x,z)}{\partial x} &= j\omega\mu(z)H_z(x,z). && (4.29) \end{aligned}$$

Substituting (4.28) and (4.29) into (4.27) gives the wave equation for E_y:

$$\left\{\frac{\partial^2}{\partial x^2} + \frac{\partial^2}{\partial z^2} - \frac{\mu'}{\mu}\frac{\partial}{\partial z} + k^2\right\} E_y(x,z) = 0. \tag{4.30}$$

Seeking a product solution as in the TM case leads directly to

$$E_y(x,z) = A\left[f(z) + \Gamma g(z)\right] \mathrm{e}^{-jk_{x0}x} \tag{4.31}$$

and

$$H_x(x,z) = -\frac{j}{\omega\mu(z)} A\left[f'(z) - \Gamma g'(z)\right] \mathrm{e}^{-jk_{x0}x}. \tag{4.32}$$

From these the transverse impedance for TE fields is defined as

$$Z(z) = -\frac{E_y(x,z)}{H_x(x,z)} = -j\omega\mu(z)\frac{f(z)+\Gamma g(z)}{f'(z)+\Gamma g'(z)}. \tag{4.33}$$

In region 0, $f(z)$, $g(z)$, and k_{z0} are defined the same as for the TM polarization case described in Section 4.2.1. Using $f(z)$, $g(z)$, and k_{z0} in (4.33) again gives (4.13), but with

$$\mathsf{Z}_0 = \frac{\eta_0}{\cos\theta_0}. \tag{4.34}$$

The definitions of Γ_0, $f(z)$, $g(z)$, and k_{z2} are defined the same as in Section 4.2.1, but with

$$\mathsf{Z}_2 = \frac{\omega\mu_2}{k_{z2}}. \tag{4.35}$$

In the case of TE polarization, an equation identical to (4.25) is obtained. However, in the TE case

$$Z_1(z_1) = -j\omega\mu_1(z_1)\frac{f_1(z_1)+\Gamma_1 g_1(z_1)}{f_1'(z_1)+\Gamma_1 g_1'(z_1)}, \tag{4.36}$$

$$\Gamma_1 = -\frac{f_1(0) - V f_1'(0)}{g_1(0) - V g_1'(0)}, \tag{4.37}$$

$$V = j\frac{\mathsf{Z}_0}{\omega\mu_1(0)}\frac{1+\Gamma_0}{1-\Gamma_0}, \tag{4.38}$$

and

$$Z_3(z_2) = -j\omega\mu_3(z_2)\frac{f_3(z_2) + \Gamma_3 g_3(z_2)}{f_3'(z_2) + \Gamma_3 g_3'(z_2)}. \tag{4.39}$$

4.2.2 TEM and Waveguide Systems

The approach described above can also be applied to other types of wave systems, such as TEM field applicators, and rectangular waveguides. For TEM systems, equations (4.14) and (4.34) can be used by setting $\theta_0 = 0$, and by using the appropriate value for Z in each region of figure 4.1. For a TEM system with impedance Z_0, this produces

$$k_z = k, \quad Z_2 = Z_0\sqrt{\frac{\mu_{2r}}{\epsilon_{2r}}}. \tag{4.40}$$

For rectangular waveguides, it is assumed that the frequency band is such that only the dominant TE_{10} mode propagates in the empty guide. Then, the equations for k_{z2} in Sections 4.2.1 and 4.2.1 may be used with $\sin\theta_0$ replaced by k_c/k_0. Here $k_c = \pi/a$ is the cutoff wavenumber, where a is the width of the guide (assumed to be the wide dimension). This produces

$$k_z = \sqrt{k^2 - \left(\frac{\pi}{a}\right)^2}, \tag{4.41}$$

$$Z_0 = \frac{\omega\mu_0}{\sqrt{k_0^2 - (\frac{\pi}{a})^2}}, \quad Z_2 = \frac{\omega\mu_2}{\sqrt{k_2^2 - (\frac{\pi}{a})^2}}, \tag{4.42}$$

etc.

4.2.3 Closed Form Expressions for ϵ_2 and μ_2

Assume that measurements of Γ_0 are made with two different underlays, designated A and B. From these, values of $Z_1(z_1)$ can be computed from (4.21) or (4.36) and values of $Z_3(z_2)$ can be computed from (4.23) or (4.39). Solving (4.25) for $\tan k_{z2}\delta$ in both measurements A and B and equating gives

$$\tan k_{z2}\delta = j\mathrm{Z}_2 \frac{Z_3^A - Z_1^A}{\mathrm{Z}_2^2 - Z_3^A Z_1^A} = j\mathrm{Z}_2 \frac{Z_3^B - Z_1^B}{\mathrm{Z}_2^2 - Z_3^B Z_1^B}, \tag{4.43}$$

where $Z_1^A = Z_1^A(z_1)$, $Z_3^A = Z_3^A(z_2)$, etc. Solving for Z_2 then gives

$$\mathrm{Z}_2^2 = \frac{Z_1^A Z_1^B (Z_3^B - Z_3^A) - Z_3^A Z_3^B (Z_1^B - Z_1^A)}{(Z_3^B - Z_3^A) - (Z_1^B - Z_1^A)}. \tag{4.44}$$

Using this value of Z_2, k_{z2} may be computed from (4.43), and from these ϵ_2 and μ_2 are found from

$$\epsilon_{2r} = \frac{k_{z2}\eta_0}{k_0 \mathrm{Z}_2}, \;\; \mu_{2r} = \frac{k_{z2}^2 + k_0^2 \sin^2\theta_0}{k_0^2 \epsilon_{2r}} \tag{4.45}$$

for TM polarization, and

$$\mu_{2r} = \frac{k_{z2}\mathrm{Z}_2}{k_0 \eta_0}, \;\; \epsilon_2 = \frac{k_{z2}^2 + k_0^2 \sin^2\theta_0}{k_0^2 \mu_{2r}} \tag{4.46}$$

for TE polarization. Note that $k_0 \sin\theta_0 = \pi/a$ should be used with (4.46) for a rectangular waveguide with a TE_{10} incident field. In a TEM system, the equations are merely

$$\mu_{2r} = \frac{k_{z2}\mathrm{Z}_2}{k_0 \mathrm{Z}_0}, \;\; \epsilon_{2r} = \frac{k_{z2}\mathrm{Z}_0}{k_0 \mathrm{Z}_2}. \tag{4.47}$$

Some care is required to ensure that the proper branch of the arctangent function is used when computing k_{z2}. However, if it is known *a priori* that the material is a dielectric with $\mu = \mu_0$, then ϵ_2 may be computed using only Z_2^2. In this case,

$$\epsilon_{2r} = \frac{\eta_0^2}{2\mathrm{Z}_2^2}\left[1 + \sqrt{1 - 4\frac{\mathrm{Z}_2^2}{\eta_0^2}\sin^2\theta_0}\right] \tag{4.48}$$

for TM polarization, and

$$\epsilon_{2r} = \frac{\eta_0^2}{\mathrm{Z}_2^2} + \sin^2\theta_0 \tag{4.49}$$

for TE polarization. A TEM system gives the particularly simple formula

$$\epsilon_{2r} = \left(\frac{\mathsf{Z}_0}{\mathsf{Z}_2}\right)^2 \tag{4.50}$$

for a dielectric.

Note that these closed-form expressions are valid for any combinations of overlays and underlays, and thus the MUT may be contained within any known sequence of material layers. Note also that when the sample has low loss, the condition $\tan k_{z2}\delta \approx 0$ may be encountered at certain frequencies when computing k_{z2} from (4.43). Thus, the sample thicknesses

$$\delta = n\frac{\lambda_2}{2}, \quad n = 1, 2, \ldots \tag{4.51}$$

should be avoided. Here $\lambda_2 = 2\pi/\Re\{k_{z2}\}$.

4.2.4 Some Special Layer Arrangements

Homogeneous material backing

Consider the case where region 3 in Figure 4.1 is an unterminated homogeneous material of permittivity ϵ_3 and permeability μ_3 (a special case of which is air). Then

$$f_3(z) = e^{jk_{z3}z}, \quad g_3(z) = 0, \tag{4.52}$$

where $k_{z3} = \sqrt{k_3^2 - k_0^2 \sin^2\theta_0}$. Substituting these into (4.23) and (4.39) gives

$$Z_3(z) = \mathsf{Z}_3 \tag{4.53}$$

for both TM and TE polarization.

Shifted Conductor Underlay

Consider the case where region 3 is a homogeneous material of permittivity ϵ_3 and permeability μ_3, backed by a perfect conductor located at $z = z_3$. Then

$$f_3(z) = e^{jk_{z3}z}, \quad g_3(z) = e^{-jk_{z3}z}. \tag{4.54}$$

Applying the boundary condition $Z(z_3) = 0$ using the equations (4.23) and (4.39) leads to

$$Z_3(z) = j\mathrm{Z}_3 \tan k_{z3}(z_3 - z), \quad z_2 \le z \le z_3 \tag{4.55}$$

for both TM and TE polarization. For the special case where the conductor is located directly against the MUT, using $z_3 = 0$ produces

$$Z_3(z) = 0. \tag{4.56}$$

Material backing terminated by air

In this case region 3 consists of a homogeneous material layer of permittivity ϵ_3 and permeability μ_3 extending from $z = z_2$ to $z = z_3$, backed by an unterminated air region, $z > z_3$. In this case

$$f_3(z) = \begin{cases} \mathrm{e}^{-jk_{z3}z}, & z_2 \le z \le z_3 \\ \mathrm{e}^{-jk_{z0}z}, & z \ge z_3 \end{cases} \tag{4.57}$$

$$g_3(z) = \begin{cases} \mathrm{e}^{jk_{z3}z}, & z_2 \le z \le z_3 \\ 0, & z \ge z_3 \end{cases}. \tag{4.58}$$

Applying continuity of the impedances at $z = z_3$ results in

$$Z_3(z) = \mathrm{Z}_3 \frac{\mathrm{Z}_0 + j\mathrm{Z}_3 \tan k_{z3}(z_3 - z)}{\mathrm{Z}_3 + j\mathrm{Z}_0 \tan k_{z3}(z_3 - z)}, \quad z_2 \le z \le z_3 \tag{4.59}$$

for both TM and TE polarizations.

4.3 Formulation of Standard Methods Using Impedance Approach

Several standard methods can be established by combining measurements for the specific underlays considered in section 4.2.4. Several of these produce particularly simple expressions for ϵ_r and μ_r. Note that to implement these methods, the measurements should be calibrated so that the phase reference for both reflection coefficients is at the front face of the MUT.

4.3.1 Two-Backing Method

In this technique the MUT is backed by underlays consisting of two different materials. Typically, measurement A is made with the MUT backed by unterminated air. Measurement B is made with a layer of material behind the MUT, occupying $z_2 \leq z \leq z_3$, with an unterminated air region occupying $z > z_3$. Then,

$$Z_3^A = 0, \quad Z_3^B = \mathrm{Z}_3 \frac{\mathrm{Z}_0 + j\mathrm{Z}_3 \tan k_{z3}\Delta}{\mathrm{Z}_3 + j\mathrm{Z}_0 \tan k_{z3}\Delta} \tag{4.60}$$

where $\Delta = z_3 - z_2$ is the thickness of the underlay.

Although the resulting equations are more complicated, it is straight forward to extend this technique to using two underlays, each backed by air. Then

$$Z_3^A = \mathrm{Z}_3^A \frac{\mathrm{Z}_0 + j\mathrm{Z}_3^A \tan k_{z3}^A \Delta_A}{\mathrm{Z}_3^A + j\mathrm{Z}_0 \tan k_{z3}^A \Delta_A}, \tag{4.61}$$

$$Z_3^B = \mathrm{Z}_3^B \frac{\mathrm{Z}_0 + j\mathrm{Z}_3^B \tan k_{z3}^B \Delta_B}{\mathrm{Z}_3^B + j\mathrm{Z}_0 \tan k_{z3}^B \Delta_B}. \tag{4.62}$$

Air/Conductor Backed Method

The air/conductor backed method is a special case of the the two-backing method, and is described in [33]. In this formulation, let measurement A be made with a conductor placed directly behind the MUT, and let measurement B be made with the MUT backed by an unterminated air region. The appropriate arrangement for a free-space system is shown in Figure 4.2. In a guided-wave system, the conductor backing is replaced by a short circuit, and the air backing is replaced by a matched load, as shown in Figure 4.3.

In each case the MUT may be covered by an arbitrary overlay. From (4.56) and (4.53),

$$Z_3^A(z_2) = 0, \quad Z_3^B(z_2) = \mathrm{Z}_0. \tag{4.63}$$

Substituting these into (4.44) gives

$$\mathrm{Z}_2^2 = \frac{\mathrm{Z}_0 Z_1^A(z_1) Z_1^B(z_1)}{\mathrm{Z}_0 + Z_1^A(z_1) - Z_1^B(z_1)}, \tag{4.64}$$

while (4.43) produces

$$\tan k_{z2}\delta = -j\frac{Z_1^A(z_1)}{\mathrm{Z}_2}. \tag{4.65}$$

Recall that if there is no overlay then $Z_1(z_1)$ is computed via (4.26).

Experimental Results Using the Air/Conductor Backed Method with a Waveguide System

As an example of employing the air/conductor backed method, a Plexiglas sample of thickness $\delta = 0.498$ cm was placed into an X-band rectangular waveguide, as shown in Figure 4.3, and the reflection coefficient Γ_0 was measured using an HP 8510C vector network analyzer (VNA). The VNA was first calibrated using a waveguide calibration kit with the short/open/match technique. Following this, the reflection coefficient Γ_0^A was measured with the sample backed by a short circuit and then the reflection coefficient Γ_0^B was measured with the waveguide terminated in a matched load. From these, the quantities Z_1^A and Z_1^B were computed assuming no overlay (i.e., using (4.26)). Finally, Z_2 and k_{z2} were found from (4.64) and (4.65), and then ϵ_r and μ_r were calculated using (4.46).

The extracted complex values of μ_r and ϵ_r are shown in Figure 4.4. The extracted real part of μ_r is very close to unity and the extracted imaginary part of μ_r is close to zero. This is as expected, since Plexiglas is non-magnetic. The extracted real part of ϵ_r is around 2.6 across X-band, which is the typically quoted value for Plexiglas. There is some slight oscillation in this value, indicative of an imperfect waveguide calibration. The imaginary part of ϵ_r is small and imaginary over most of the band. Again, this is as expected for a low-loss dielectric.

4.3.2 Conductor-Backed Methods

Conductor-backed methods are those techniques that utilize a single material sample with two different homogeneous, conductor-backed underlays. The underlays may consist of the same material with two different thicknesses (Δ_A and Δ_B), two different materials with the same thickness, or two different materials with two different thicknesses. The underlay material may be air, or any other material with known parameters. If both underlays are air, the method is viewed as placing short circuits at two positions behind the MUT. Each of these cases may be treated using

$$Z_3^A(z_2) = jZ_3^A \tan k_{z3}^A \Delta_A, \quad Z_3^B(z_2) = jZ_3^B \tan k_{z3}^B \Delta_B. \tag{4.66}$$

Substitution into (4.44) gives the formula for Z_2, with μ_r and ϵ_r found from (4.45) or (4.46).

Layer-Shift Method

The layer-shift method is a simple implementation of a conductor-backed method, as described in [3]. Here measurement A is made with the conductor placed directly behind the MUT, and can be viewed as having an underlay of zero thickness. Measurement B is made with the MUT shifted a distance Δ from the conductor, and is viewed as having a spacer underlay (typically air) with properties ϵ_3 and μ_3. See Figure 4.5 for a free-space implementation of the layer-shift method.

The two arrangements thus produce

$$Z_3^A(z_2) = 0, \quad Z_3^B(z_2) = j\mathrm{Z}_3 \tan k_{z3}\Delta. \tag{4.67}$$

Using equation (4.67) in conjunction with equation (4.44) then gives

$$\mathrm{Z}_2^2 = \frac{[j\mathrm{Z}_3 \tan k_{z3}\Delta]\, Z_1^A(z_1) Z_1^B(z_1)}{j\mathrm{Z}_3 \tan k_{z3}\Delta + Z_1^A(z_1) - Z_1^B(z_1)} \tag{4.68}$$

and

$$\tan k_{z2}\delta = -j\frac{Z_1^A(z_1)}{\mathrm{Z}_2} \tag{4.69}$$

from which ϵ and μ may be found. Note that when the spacer has low loss, the condition $\tan k_{z3}\Delta \approx 0$ may be encountered at certain frequencies. Thus, the spacer thicknesses

$$\Delta = n\frac{\lambda_3}{2}, \quad n = 1, 2, \ldots \tag{4.70}$$

should be avoided. Here $\lambda_3 = 2\pi/\Re\{k_{z3}\}$.

As examples of the layer-shift method, experiments were undertaken using both a free-space and a coaxial TEM implementation.

Free-Space Implementation of the Layer-Shift Method

A free-space implementation of the layer-shift method was used at the Boeing Materials Measurement Laboratory to characterize a sample of magnetic radar absorbing material (MagRAM) consisting of a suspension of 35% by volume of BASF EW grade magnetic particles in a commercially available polyurethane elastomeric resin. A sample sheet of thickness $\delta = 0.1452$ cm and 60.96 cm on a side was placed on top of an aluminum plate, and illuminated using a focus-beam system at an incidence angle of $\theta_0 = 40^\circ$ with both parallel and perpendicular polarization.

The reflection coefficient Γ_0 was measured in the frequency range 5-18 GHz using a E8362C PNA network analyzer, which was calibrated using the same aluminum plate. Next a plexiglas spacer of thickness $\Delta = 0.5861$ cm was placed between the sample and the plate, and Γ_0 was again measured. The two sets of measurements were used to determine ϵ_r and μ_r via (4.68) and (4.69), with the dielectric constant of Plexiglas assumed to be $\epsilon_{3r} = 2.66$. The results for both polarizations are shown in Figures 4.6 and 4.7. Also shown in the figures are the values for ϵ_r and μ_r found by taking a small section from the sample sheet, placing it into a waveguide, and using the Nicolson-Ross-Weir reflection/transmission method [40],[54]. Results are reasonably consistent between polarizations, and agree well with the waveguide results, except for the real part of ϵ_r where the waveguide measurement reveals a somewhat smaller value. This is most likely due to a variation in the material parameters across the sheet. Indeed, it is not unusual for ϵ_r to be slightly different at the edge of the sample, where the waveguide section was removed, than in the middle of sheet where the beam illumination is concentrated.

Note that the extracted material parameters become quite unreliable around 17 GHz. At this frequency, the spacer is approximately one half of a wavelength thick, and thus $\tan k_{z3}\Delta \approx 0$. Under this condition, values of Z_2 computed from (4.68) experience large error due to measurement uncertainty.

Coaxial Implementation of the Layer-Shift Method

A coaxial implementation of the layer-shift method was carried out using an applicator consisting of two Electro-metrics EM2107-A coaxial adapters mated with a brass fixture. The adapters provide a transition from a standard N-type coaxial connector to a 15 cm long, 51 Ω coaxial system with a center conductor of diameter 3.3 cm, and an outer conductor with inner diameter 7.6 cm (Figure 4.9).

An 11.8 cm long Plexiglas sample was machined into a coaxial shape and placed into the fixture. The reflection coefficient Γ_0 was then measured using an Agilent 8753D VNA calibrated using a through-reflect-line (TRL) method [44], [17]. The reflection coefficient was first measured with the plexiglas sample placed against a shorting plate, then with a styrofoam spacer ($\epsilon_r = 1$) of thickness 2.54 cm placed between the sample and the plate (see Figure 4.8).

Values of ϵ_r and μ_r were computed in the band 44-1000 MHz using the measured values of Γ_0, and are shown in Figure 4.10. In the range 100-700 MHz the results are those expected for Plexiglas, with the real part of ϵ_r approximately 2.6, the imaginary part of ϵ_r close to zero, and $\mu_r \approx 1$. Below 100 MHz the sample becomes quite short compared to a wavelength, and the measured phase of Γ_0 is greatly affected by VNA phase uncertainty. Thus, the results below this frequency are unreliable. Around 700 MHz, the Plexiglas sample becomes a half wavelength long, and so $\tan k_{z2}\delta \approx 0$ in (4.69). Again the results become unreliable due to measurement uncertainty.

4.3.3 Two-Thickness Method

The two-thickness method, illustrated in Figure 4.11, differs in principle from the other underlay methods in that the properties of the underlay are not entirely known. This is because the underlay material is assumed to be identical to the unknown MUT. Here measurement A is made with the MUT backed by a conductor, and so $Z_3^A(z_2) = 0$.

From (4.25) this implies

$$Z_1^A = j\mathrm{Z}_2 \tan k_{z2}\delta. \tag{4.71}$$

Measurement B is made with the MUT placed against an underlay of material identical to the MUT, with thickness Δ (essentially creating a MUT with a larger thickness than in measurement A). Thus, measurements A and B are in essence two measurements of the MUT but with different thicknesses. From (4.25) and (4.55), the impedance of configuration B is

$$\begin{aligned} Z_1^B &= \mathrm{Z}_2 \frac{j\mathrm{Z}_2 \tan k_{z2}\Delta + j\mathrm{Z}_2 \tan k_{z2}\delta}{-\mathrm{Z}_2 \tan k_{z2}\delta \tan k_{z2}\Delta + \mathrm{Z}_2} \\ &= j\mathrm{Z}_2 \tan k_{z2}(\delta + \Delta). \end{aligned} \tag{4.72}$$

Eliminating Z_2 then gives a transcendental equation for k_{z2}:

$$\tan k_{z2}\delta = \frac{Z_1^A}{Z_1^B}\tan k_{z2}(\delta+\Delta). \tag{4.73}$$

This can be manipulated to show that k_{z2} also satisfies the alternative equation

$$\sin k_{z2}\Delta = \frac{Z_1^B - Z_1^A}{Z_1^B + Z_1^A}\sin k_{z2}(2\delta+\Delta), \tag{4.74}$$

which may be numerically advantageous. Once this is solved, Z_2 can be computed from (4.71).

Obviously, the two-thickness method is more complicated than the other underlay techniques in that it requires a root search (although once the root search is completed the same closed form expressions for ϵ_r and μ_r are used). Fortunately, the special case of $\Delta = \delta$ (i.e., using two sample thicknesses with the second thickness twice the first) does give closed-form solutions for Z_2 and k_{z2}:

$$\mathsf{Z}_2^2 = \frac{\left(Z_1^A\right)^2}{2\frac{Z_1^A}{Z_1^B} - 1} \tag{4.75}$$

$$\tan(k_{z2}\delta) = -\sqrt{1 - 2\frac{Z_1^A}{Z_1^B}}. \tag{4.76}$$

A free-space implementation of the two-thickness method was undertaken using the Boeing free-space range in the manner described in Section 4.3.2. First a 0.142 cm thick sample of MagRAM was placed against an aluminum plate and the reflection coefficient was measured under both parallel and perpendicular polarizations at an aspect angle of $\theta_0 = 40°$. Then a 0.145 cm thick sample of the same type of MagRAM was laid on top of the first sample and the reflection coefficients were again measured.

The two samples were first assumed to be of the same thickness, and the formula (4.76) was used to find k_{z2}. This result was then used as an initial guess in (4.73) to find the actual value of k_{z2} using the two slightly different sample thicknesses. With k_{z2} known, Z_2 was found from (4.71) and ϵ_r and μ_r computed from the closed-form expressions. The resulting permittivity and permeability are shown in Figures 4.6 and 4.7 for the frequency range 5-18 GHz. It can be seen that the extracted parameters compare quite well to the results obtained using the free-space implementation of the layer-shift method. However, the two-thickness results do not show the anomaly at 17 GHz caused by the spacer used in the layer-shift method.

4.4 Conclusion

This chapter demonstrates use of a unifying set of extraction equations for many non-resonant, reflection-only material characterization methods. Accuracy of the extraction equations was proven via implementation of three different reflection-only methods with actual measured data of both dielectric and magnetic media. Excellent agreement between extracted ϵ_r and μ_r using the extraction equations presented in this work and traditional material characterization methods and nominal material parameters was achieved. Therefore, a common resource for all performing material characterization using non-resonant, reflection-only material characterization methods has been accomplished.

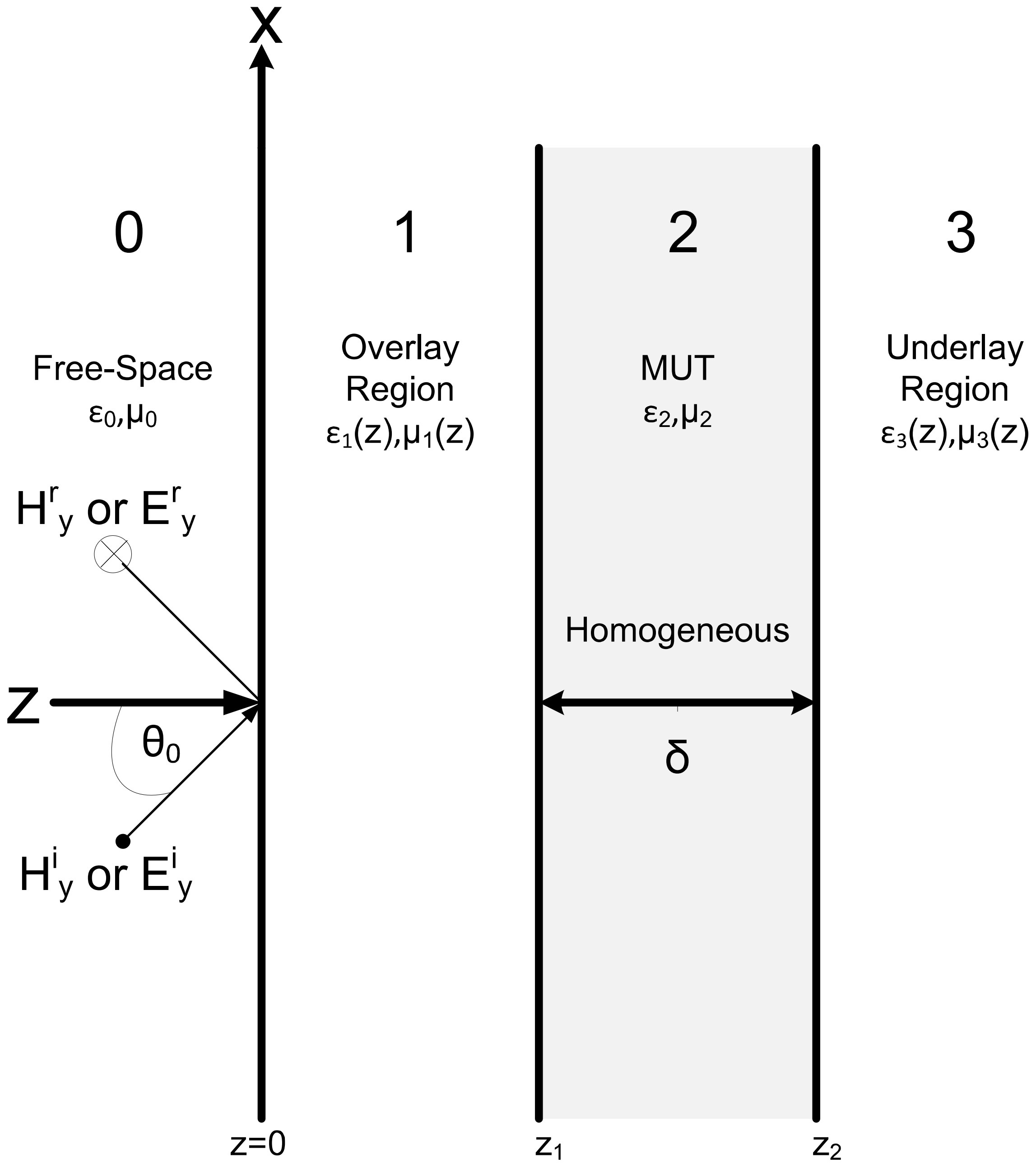

Figure 4.1: A free-space material characterization configuration that uses reflection-only measurements

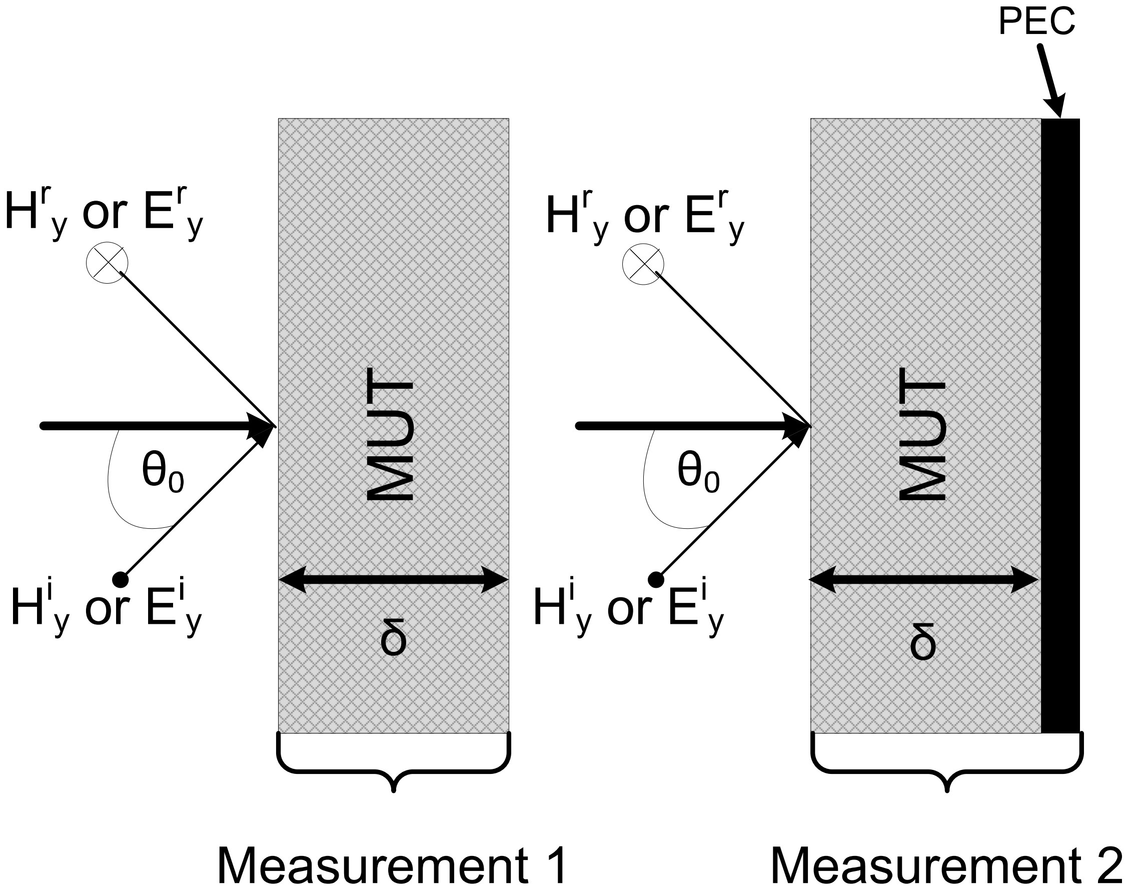

Figure 4.2: Free-space arrangement for the air/conductor backed method

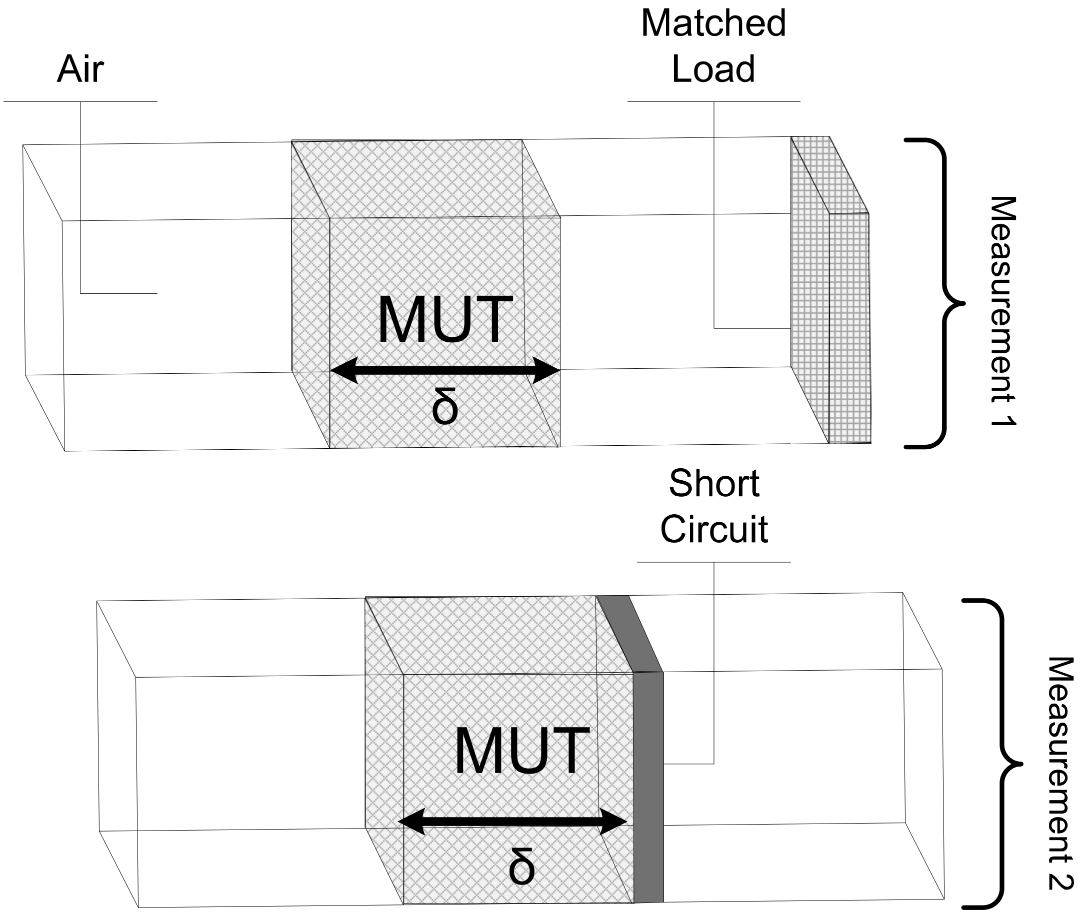

Figure 4.3: Rectangular waveguide arrangement for the air/conductor backed method

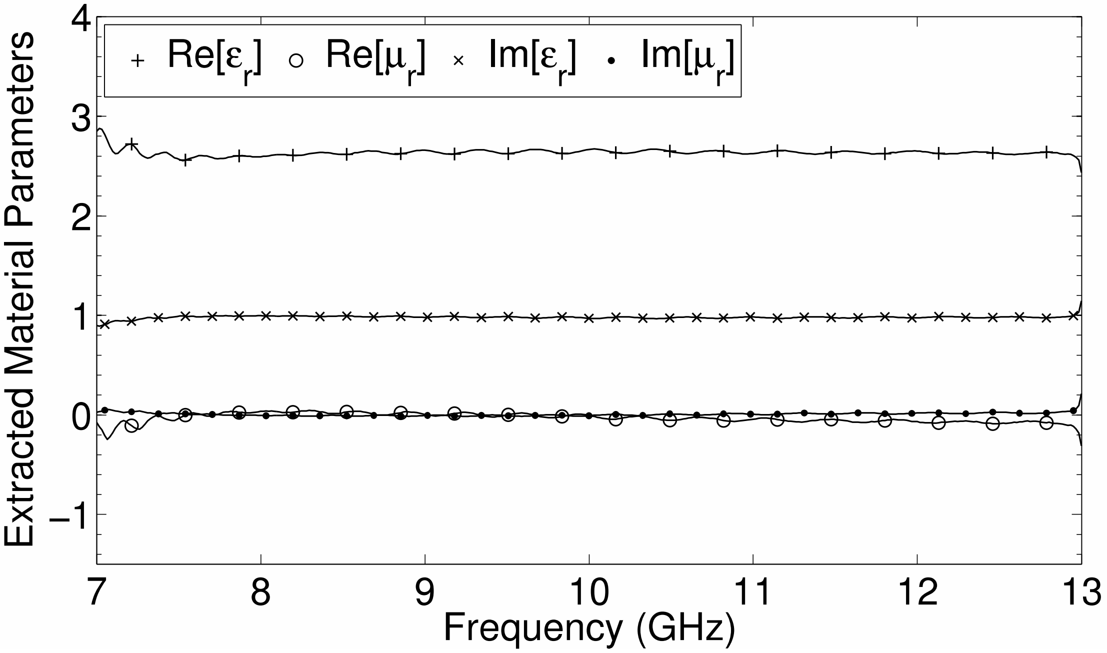

Figure 4.4: Material parameters for Plexiglas extracted using the air/conductor backed method with a rectangular waveguide system

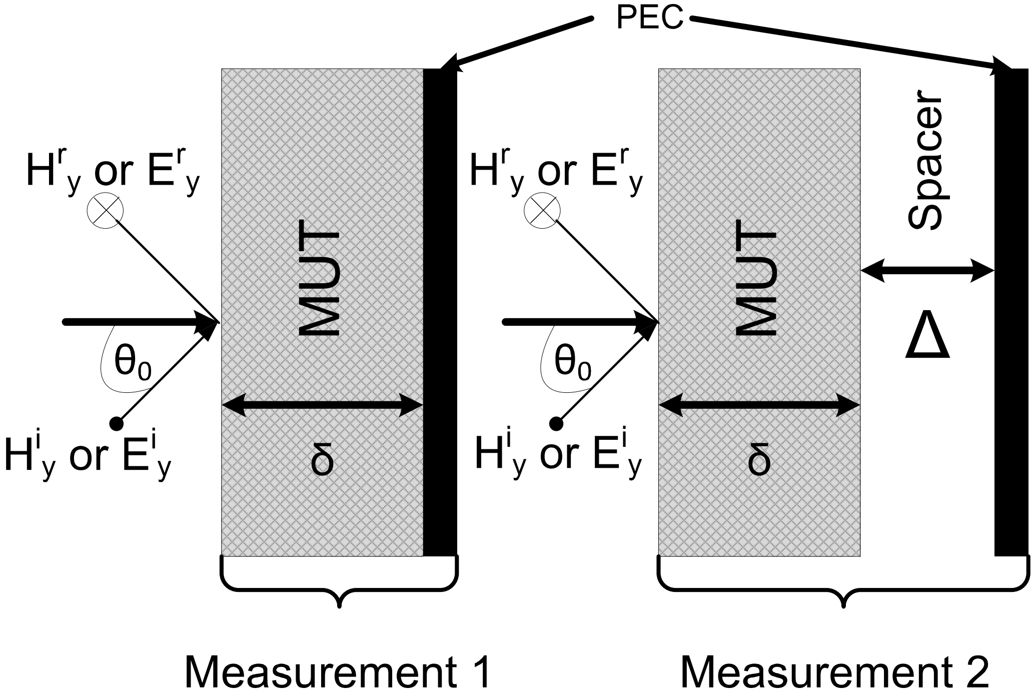

Figure 4.5: Free-space implementation of the layer-shift method

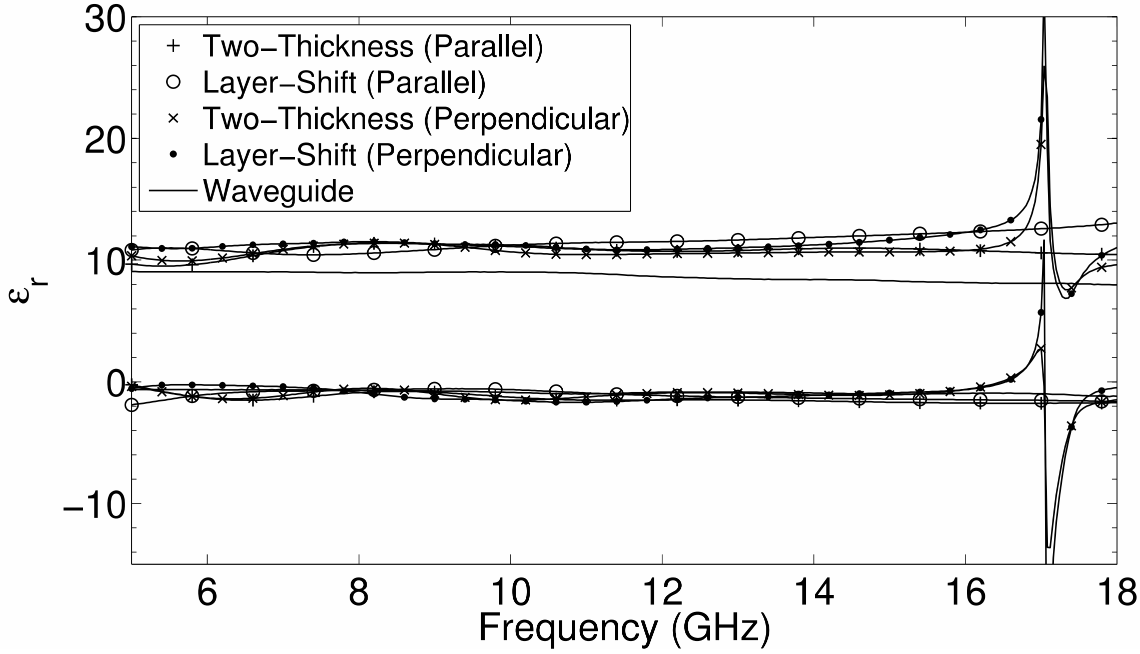

Figure 4.6: Permittivity of a 35% MagRAM sample extracted using free-space reflection-only methods

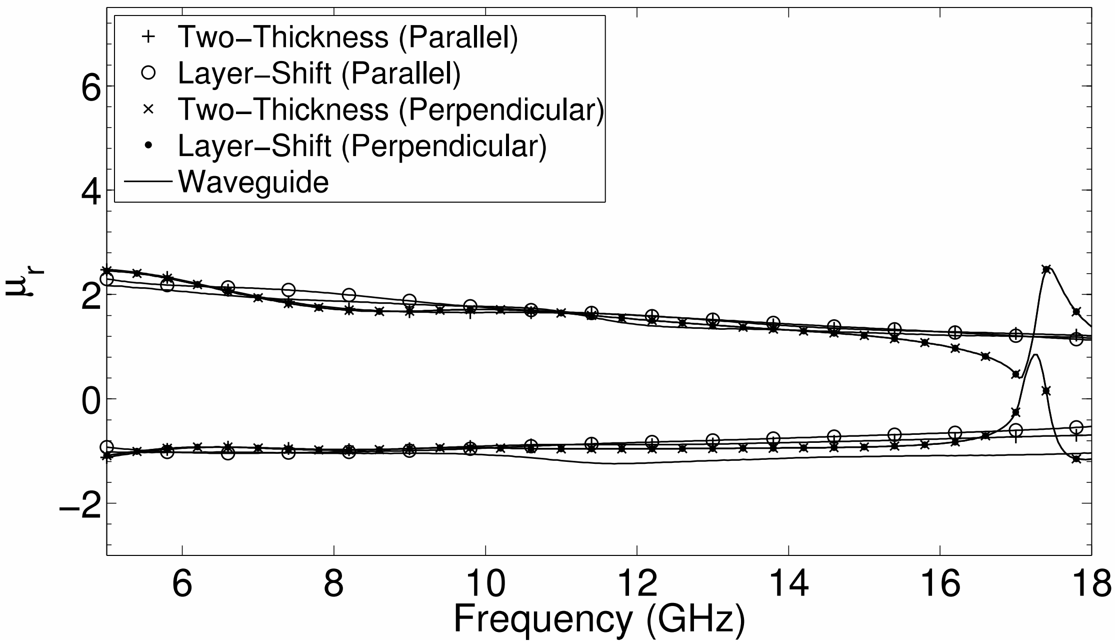

Figure 4.7: Permeability of a 35% MagRAM sample extracted using free-space reflection-only methods

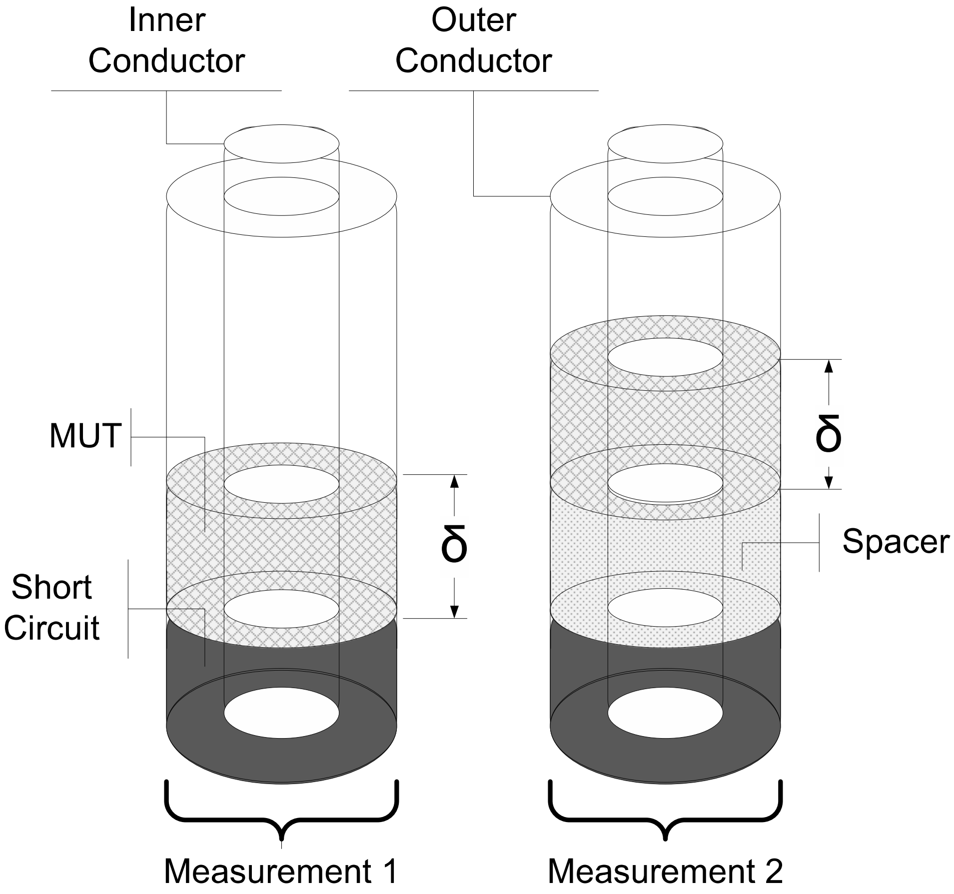

Figure 4.8: Coaxial representation of the layer-shift method

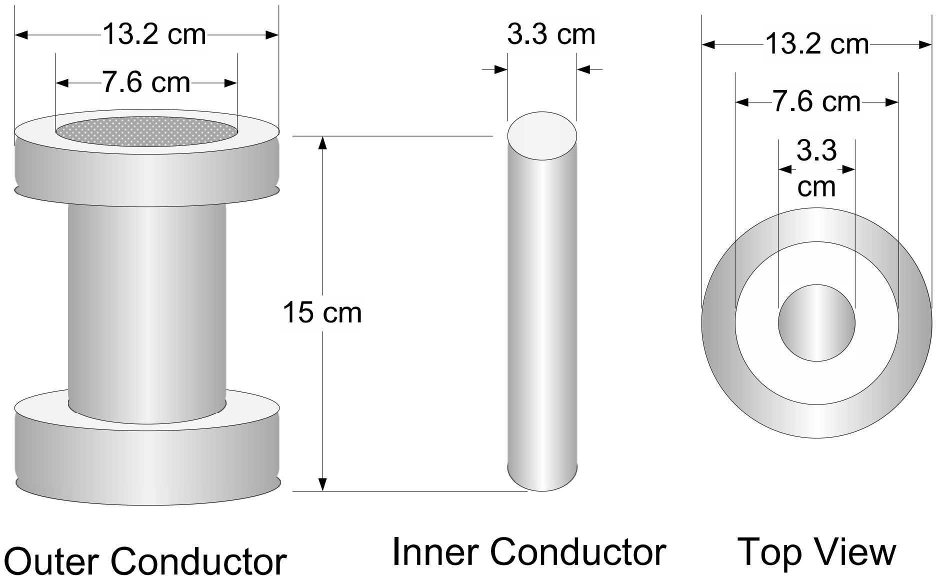

Figure 4.9: Diagram of the coaxial fixture used for TEM guided-wave implementation of the layer-shift method

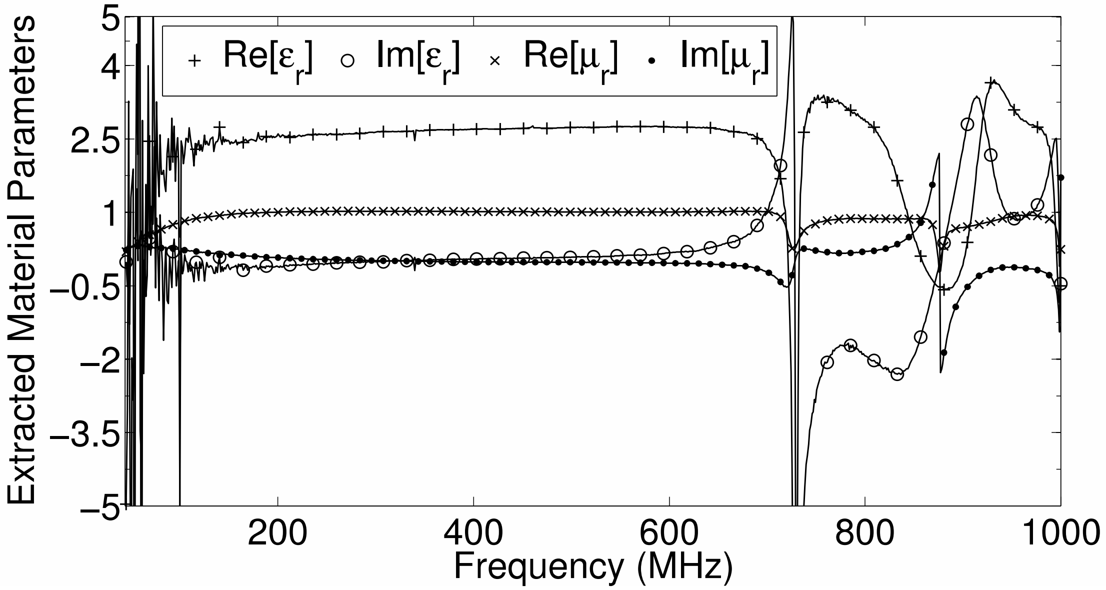

Figure 4.10: Permittivity extracted using a coaxial implementation of the layer-shift method

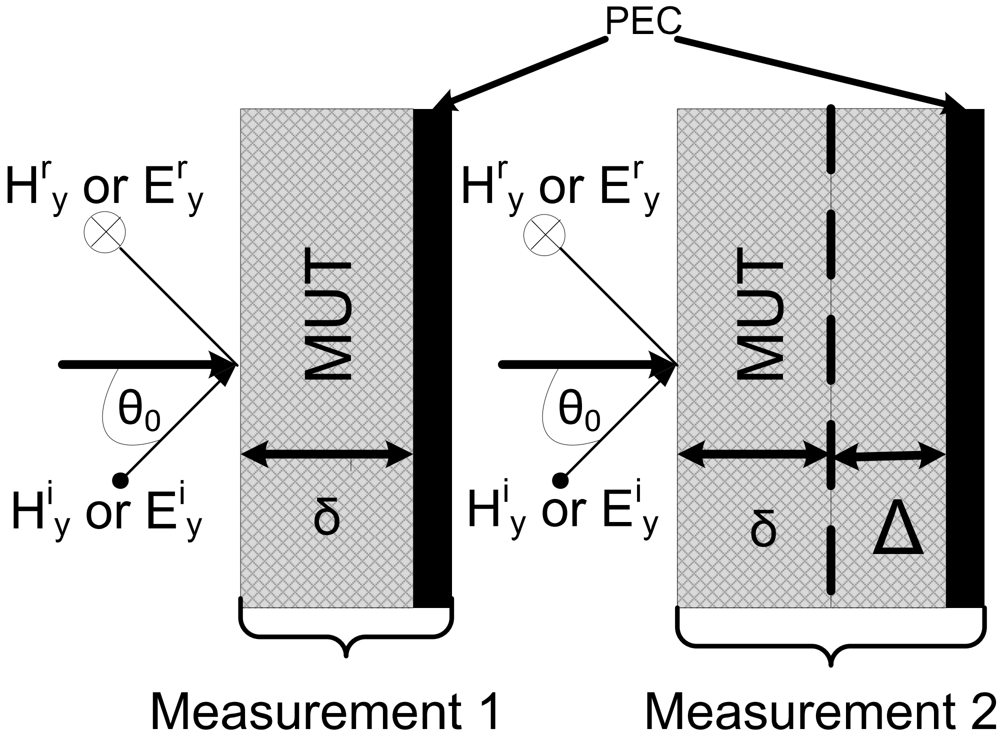

Figure 4.11: Free-space implementation of the two-thickness method

Chapter 5

The Dual Polarization Method

5.1 Introduction

The characterization of conductor-backed media has become an important task. For example, with the increased need for nondestructive testing of shielding materials adhered to perfect electric conductors (PEC) or in quality control applications, knowledge of a material's electrical properties can be very useful. There are three main categories of material characterization methods: (1) waveguide methods, (2) probe methods, and (3) free-space methods. There are several ways to characterize a conductor-backed medium using waveguide methods or probe methods as found in [5], [31], and [7]. Unfortunately, these methods are insufficient for nondestructive *in situ* samples or where no contact or alteration to the sample is allowed. In the specific cases where waveguide or probe methods are not feasible, free-space material characterization methods are necessary. However, most mainstream free-space methods that are considered reliable, like in [40] and [33], utilize transmission data or removal of the PEC backing in some capacity.

A proposed method for characterizing conductor-backed media is termed the *dual-polarization method*. The dual-polarization method uses the measured reflection coefficient from parallel and perpendicular polarized incident plane waves. In this manner, closed form expressions can be found for μ_r and ϵ_r.

This chapter explores the usefulness and reliability of the dual-polarization method by performing a thorough error analysis of the method. Thus, the main contribution of this chapter is to determine when the dual-polarization method can be used utilized and explain the method's shortcomings. Section 5.2 reviews the derivation of the dual-polarization method. Section 5.3 describes the parameters which cause error in the dual-polarization method, error analysis methods used, and analysis of how error can be amplified. The dual-polarization method is then used to simulate extraction of two sample materials in Section 5.4. Conclusions and future work are presented in Section 5.5.

5.2 Extraction method

Consider a conductor-backed planar material layer with thickness Δ, complex permeability $\mu(\omega) = \mu_0\mu_r(\omega)$ and complex permittivity $\epsilon(\omega) = \epsilon_0\epsilon_r(\omega)$, as shown in Figure 5.1. The layer is illuminated by a uniform plane wave of frequency ω, originating in an overlay region with complex permeability $\bar{\mu}(\omega) = \mu_0\bar{\mu}_r(\omega)$ and complex permittivity $\bar{\epsilon}(\omega) = \epsilon_0\bar{\epsilon}_r(\omega)$. If illumination occurs at an incidence angle θ from the normal to the surface, then the electric field reflected by the layer is determined by the global reflection coefficient

$$\Gamma(\omega) = \frac{R(\omega) - P^2(\omega)}{1 - R(\omega)P^2(\omega)}. \tag{5.1}$$

Here P is the propagation factor

$$P(\omega) = e^{-jk_z(\omega)\Delta} \tag{5.2}$$

and R is the interfacial (Fresnel) reflection coefficient

$$R(\omega) = \frac{Z(\omega) - \bar{Z}(\omega)}{Z(\omega) + \bar{Z}(\omega)}. \tag{5.3}$$

The wave impedances are dependent on the polarization of the illuminating field with respect to the plane of incidence. For the material under test (MUT) the impedance is

$$Z = \begin{cases} k\eta/k_z, & \perp\text{-polarization} \\ k_z\eta/k, & \|\text{-polarization,} \end{cases} \tag{5.4}$$

while for the overlay the impedance is

$$\bar{Z} = \begin{cases} \bar{k}\bar{\eta}/\bar{k}_z = \bar{\eta}/\cos\theta, & \perp\text{-polarization} \\ \bar{k}_z\bar{\eta}/\bar{k} = \bar{\eta}\cos\theta, & \|\text{-polarization.} \end{cases} \tag{5.5}$$

Here $k_0 = \omega/c$, $k = k_0\sqrt{\mu_r\epsilon_r}$, $\eta = \eta_0\sqrt{\mu_r/\epsilon_r}$, and $k_z = k_0\sqrt{\mu_r\epsilon_r - \bar{\mu}_r\bar{\epsilon}_r\sin^2\theta}$. The definitions of $\bar{k}$, $\bar{\eta}$, and $\bar{k}_z$ follow, with $(\bar{\mu}_r, \bar{\epsilon}_r)$ in place of $(\mu_r\epsilon_r)$.

Defining

$$K = \frac{k_z}{\bar{k}_z}, \quad H = \frac{k}{\bar{k}}\frac{\eta}{\bar{\eta}}, \quad I = \frac{\bar{\eta}}{\bar{k}}\frac{k}{\eta} \tag{5.6}$$

allows the interfacial reflection coefficients to be written as

$$R_\perp = \frac{H-K}{H+K} \tag{5.7}$$

for perpendicular polarization and

$$R_\| = \frac{K-I}{K+I} \tag{5.8}$$

for parallel polarization. Substituting these into (5.1) then gives the global reflection coefficients

$$\Gamma_\perp = \frac{HQ-K}{HQ+K} \tag{5.9}$$

$$\Gamma_\| = \frac{KQ-I}{KQ+I} \tag{5.10}$$

where

$$Q = \frac{1-P^2}{1+P^2} = j\tan(k_z\Delta). \tag{5.11}$$

Three situations are of interest:

1. Both μ_r and ϵ_r are unknown, but Δ is known.
2. The MUT is a dielectric with $\mu = \mu_0$, but both ϵ_r and Δ are unknown.
3. The MUT is a dielectric with $\mu = \mu_0$, but only ϵ_r is unknown.

The first two situations have two unknown quantities, and thus require two independent measurements. Using measurements of $\Gamma_\perp$ and $\Gamma_\parallel$ at the same angle θ is called the *dual-polarization method*. The third situation involves a single unknown quantity and thus requires only one measurement, which can be made at any angle and with either polarization. The third situation is also a variation of a well known method termed the *short-circuited reflection method* [33]. Since the focus of this dissertation is on characterization of both ϵ_r and μ_r, situation one is the focus of this chapter. The extraction equations for all three situations are derived for completeness. A fourth case in which the three parameters μ_r, ϵ_r and Δ are all unknown is left to future study.

5.2.1 Dual-polarization method for μ and ϵ

To find μ_r and ϵ_r, begin by solving (5.9) for K:

$$K = HQ\frac{1-\Gamma_\perp}{1+\Gamma_\perp}. \tag{5.12}$$

In addition, solve (5.10) for K:

$$K = \frac{I}{Q}\frac{1+\Gamma_\parallel}{1-\Gamma_\parallel} \tag{5.13}$$

Multiplying these gives

$$K^2 = HIY \tag{5.14}$$

where

$$Y = \left(\frac{1-\Gamma_\perp}{1+\Gamma_\perp}\right)\left(\frac{1+\Gamma_\parallel}{1-\Gamma_\parallel}\right). \tag{5.15}$$

Here Y is a known quantity, computed from the measured values of $\Gamma_\perp$ and $\Gamma_\|$. Substituting from (5.6) into (5.14) then gives

$$\left(\frac{k_z}{\bar{k}_z}\right)^2 = Y(HI) = \frac{k^2}{\bar{k}^2}Y. \tag{5.16}$$

Thus,

$$k_z^2 = k^2 - \bar{k}^2 \sin^2\theta = k^2 Y \cos^2\theta. \tag{5.17}$$

Rearranging gives

$$\frac{k^2}{\bar{k}^2}\left(1 - Y\cos^2\theta\right) = \sin^2\theta. \tag{5.18}$$

But since

$$\frac{k^2}{\bar{k}^2} = \frac{\mu_r\epsilon_r}{\bar{\mu}_r\bar{\epsilon}_r}, \tag{5.19}$$

the product of the relative permeability an permittivity is given by

$$\mu_r\epsilon_r = \bar{\mu}_r\bar{\epsilon}_r \frac{\sin^2\theta}{1 - Y\cos^2\theta}. \tag{5.20}$$

It is worth pausing to examine this simple expression. Since the numerator of the fraction is bounded by unity, if the product $\mu_r\epsilon_r$ is relatively large (as is the case with many radar absorbing materials) but the product $\bar{\mu}_r\bar{\epsilon}_r$ is much smaller (as would happen if the incident field originates in air), then $Y\cos^2\theta$ must be close to unity. If this is true, then the risk of cancelation error is high when the denominator is computed, and thus the expression (5.20) has the potential for being ill-conditioned with respect to both the measured quantity Y and the assumed known angle θ.

Next, equate (5.12) and (5.13) to give

$$\frac{H}{I}Q^2 = X \tag{5.21}$$

where

$$X = \left(\frac{1+\Gamma_\perp}{1-\Gamma_\perp}\right)\left(\frac{1+\Gamma_\|}{1-\Gamma_\|}\right). \tag{5.22}$$

But since

$$\frac{H}{I} = \frac{\eta_r^2}{\bar{\eta}_r^2}, \tag{5.23}$$

the ratio of relative permeability to relative permittivity is

$$\frac{\mu_r}{\epsilon_r} = \eta_r^2 = \bar{\eta}_r^2 \frac{X}{Q^2}. \tag{5.24}$$

Because the product $\mu_r \epsilon_r$ is known from (5.20), P and Q are known, and thus (5.20) and (5.24) can be combined to give closed-form formulas for relative permeability and relative permittivity:

$$\mu_r = \pm \bar{\mu}_r \sqrt{\frac{X}{Q^2} \frac{\sin^2 \theta}{1 - Y \cos^2 \theta}} \tag{5.25}$$

$$\epsilon_r = \pm \bar{\epsilon}_r \sqrt{\frac{Q^2}{X} \frac{\sin^2 \theta}{1 - Y \cos^2 \theta}}. \tag{5.26}$$

In these expressions, the proper sign is chosen to make $\Re\{\epsilon_r\} > 0$ and $\Re\{\mu_r\} > 0$.

5.2.2 Dual-Polarization Method for ϵ and Δ

If Δ is unknown, the fact that $\mu_r = 1$ is known *a priori* produces closed-form expressions for both ϵ_r and Δ. From (5.20), ϵ_r is found to be

$$\epsilon_r = \bar{\mu}_r \bar{\epsilon}_r \frac{\sin^2 \theta}{1 - Y \cos^2 \theta} \tag{5.27}$$

while (5.24) gives Δ as

$$\Delta = \frac{1}{k_z} \tan^{-1} \sqrt{-\epsilon_r \bar{\eta}_r^2 X}. \tag{5.28}$$

Note that while Δ is a real number, (5.28) will produce complex values due to experimental error. Thus, the imaginary part of Δ gives a measure of the error in finding Δ.

5.2.3 Dielectric Materials with Δ Known (Short-Circuited Reflection Method)

If only ϵ is unknown, then a single measurement is required. Under perpendicular polarization the measured reflection coefficient is given by (5.9). Substituting the expressions for H, Q, and K gives

$$\Gamma_{\perp} = \frac{j\bar{\chi}\tan\left(k_0 d\chi\right) - \bar{\mu}_r\chi}{j\bar{\chi}\tan\left(k_0\Delta\chi\right) + \bar{\mu}_r\chi}, \tag{5.29}$$

where $\chi = \sqrt{\epsilon_r - \bar{\epsilon}_r\bar{\mu}_r\sin^2\theta}$ and $\bar{\chi} = \sqrt{\bar{\mu}_r\bar{\epsilon}_r}\cos\theta$. Rearranging gives

$$\bar{\mu}_r\chi = j\xi_{\perp}\bar{\chi}\tan\left(k_0\Delta\chi\right), \tag{5.30}$$

where $\xi_{\perp} = (1-\Gamma_{\perp})/(1+\Gamma_{\perp})$. This is a single transcendental equation for ϵ_r.

If a single measurement is made under parallel polarization, then the measured reflection coefficient is given by (5.10). Substituting the expressions for K, Q, and I gives

$$\Gamma_{\parallel} = \frac{j\chi\bar{\epsilon}_r\tan\left(k_0\Delta\chi\right) - \epsilon_r\bar{\chi}}{j\chi\bar{\epsilon}_r\tan\left(k_0\Delta\chi\right) + \epsilon_r\bar{\chi}}. \tag{5.31}$$

Rearranging gives

$$\epsilon_r\bar{\chi} = j\xi_{\parallel}\bar{\epsilon}_r\chi\tan\left(k_0\Delta\chi\right), \tag{5.32}$$

where $\xi_{\parallel} = (1-\Gamma_{\parallel})/(1+\Gamma_{\parallel})$. This is again a single transcendental equation for ϵ_r. Similar expressions can be obtained for a purely magnetic material.

Although only a single measurement is necessary to characterize ϵ_r, if two measurements are available, then equation (5.27) can be used and the root search of the transcendental equation can be avoided.

5.3 Error analysis of the Dual-Polarization Method

There are many factors that can lead to errors in the extracted values of ϵ and μ with the dual-polarization method. Among these are model assumptions (plane wave excitation, infinite sample size), manufacturing issues (uniformity of thickness, surface roughness), and measurement issues (alignment of antennas, network analyzer accuracy). The effects of three important quantities are easy to identify and analyze. It is desirable that the dual-polarization technique be robust with respect to uncertainties in θ, Δ and the measured reflection coefficients $\Gamma_\perp$ and $\Gamma_\parallel$. Uncertainties in the first two of these are caused by inaccurate information regarding geometrical parameters. For instance, the value of θ used to perform the measurements must be measured or established in a controlled manner. Similarly, knowledge of the thickness Δ is subject to measurement uncertainty or manufacturer tolerance. The measured reflection coefficients are subject to error due to measurement uncertainties introduced by the instrumentation (network analyzer).

Assume that when the measurements of θ, Δ, $\Gamma_\perp$ and $\Gamma_\parallel$ are measured repeatedly, the distribution of their measurements is described by a normal distribution with mean ξ_i and standard deviation σ_i. Here $i = 1$ refers to θ, $i = 2$ to Δ, $i = 3$ to $|\Gamma_\perp|$, $i = 4$ to $\angle\Gamma_\perp$, $i = 5$ to $|\Gamma_\parallel|$, and $i = 6$ to $\angle\Gamma_\parallel$. Then when these measured values are used to compute μ and ϵ, the computed quantities will also be normally distributed with standard deviations given by the propagation of error formula

$$\sigma_\mu = \sqrt{\sum_{i=1}^{6} \sigma_i^2 \left(\frac{\partial \mu_r}{\partial x_i}\right)^2} \tag{5.33}$$

$$\sigma_\epsilon = \sqrt{\sum_{i=1}^{6} \sigma_i^2 \left(\frac{\partial \epsilon_r}{\partial x_i}\right)^2} \tag{5.34}$$

where $x_1 = \theta$, etc [53]. This formula holds as long as the six parameters are investigation are statistically independent. Although Δ and θ certainly are, there may be some nonzero correlation between $\Gamma_\perp$ and $\Gamma_\parallel$ due to the manner in which the network analyzer operates. If so, this is assumed minor and is ignored in this analysis. Note that the partial derivative terms in (5.33) and (5.34) are sometimes called *amplification factors*. Large the amplification factors may cause the standard deviation in the computed quantity to be increased compared to the standard deviations in the measured quantities.

General formulas for the derivatives may be established by writing

$$\mu_r \epsilon_r = A = \bar{\mu}_r \bar{\epsilon}_r \frac{\sin^2\theta}{1 - Y\cos^2\theta} \tag{5.35}$$

$$\frac{\mu_r}{\epsilon_r} = B = \bar{\eta}^2 \frac{X}{Q^2} \tag{5.36}$$

so that

$$\mu_r = \pm\bar{\mu}_r \sqrt{AB} \tag{5.37}$$

$$\epsilon_r = \pm\bar{\epsilon}_r \sqrt{\frac{A}{B}}. \tag{5.38}$$

Then

$$\frac{\partial\mu_r}{\partial x_i} = \bar{\mu}_r \frac{\partial}{\partial x_i}\left(\sqrt{AB}\right) = \frac{\bar{\mu}_r}{2\mu_r}\left(\frac{1}{A}\frac{\partial A}{\partial x_i} + \frac{1}{B}\frac{\partial B}{\partial x_i}\right) \tag{5.39}$$

$$\frac{\partial\epsilon_r}{\partial x_i} = \bar{\epsilon}_r \frac{\partial}{\partial x_i}\left(\sqrt{\frac{A}{B}}\right) = \frac{\bar{\epsilon}_r}{2\epsilon_r}\left(\frac{1}{A}\frac{\partial A}{\partial x_i} - \frac{1}{B}\frac{\partial B}{\partial x_i}\right) \tag{5.40}$$

or

$$\frac{\partial\mu_r}{\partial x_i} = \frac{\bar{\mu}_r}{\mu_r}\left(F_i + G_i\right) \tag{5.41}$$

$$\frac{\partial\epsilon_r}{\partial x_i} = \frac{\bar{\epsilon}_r}{2\epsilon_r}\left(F_i - G_i\right) \tag{5.42}$$

where

$$F_i = \frac{1}{2A}\frac{\partial A}{\partial x_i} \qquad G_i = \frac{1}{2B}\frac{\partial B}{\partial x_i}. \tag{5.43}$$

In addition to using the error propagation method, Monte Carlo methods were also used to calculate error for the dual-polarization method. Monte Carlo methods are a broad class of numerical techniques that use repeated sampling experiments to calculate results, as described in Section 3.3.1. Monte Carlo simulations were implemented by adding Gaussian distributed noise to the nominal values chosen for θ, Δ, $\Gamma_\perp$, and $\Gamma_\parallel$. Monte Carlo simulations were chosen in addition to the error propagation method because of the issue of rapidly varying amplification factors encountered with the error propagation method described in Section 3.3.2. Even though the error propagation method was not used to calculate the error due to all of the parameters, the functions for the derivatives were found because a great amount of insight is gained in observation of those functions.

5.3.1 Errors due to inaccuracies in measured θ

An unexpected result is that very large errors may result from small uncertainties in the measurement angle. This effect can be seen by examining the amplification factors $\frac{\partial \mu_r}{\partial \theta}$ and $\frac{\partial \epsilon_r}{\partial \theta}$. Computing the derivatives (5.43) and simplifying the results gives

$$\frac{\partial \mu_r}{\partial \theta} = \bar{\mu}_r (F_\theta + G_\theta), \quad \frac{\partial \epsilon_r}{\partial \theta} = \bar{\epsilon}_r (F_\theta - G_\theta) \tag{5.44}$$

where

$$F_\theta = \frac{\cot\theta\,(1-Y)}{1 - Y\cos^2\theta} \tag{5.45}$$

$$G_\theta = \frac{-4jdP^2 k_z'}{Q\left(1+P^2\right)^2} \tag{5.46}$$

$$k_z' = \frac{Y k_1^2 \sin^2\theta \left(\cos 2\theta - Y\cos^4\theta\right)}{2k_z\left(1 - Y\cos^2\theta\right)^2} \tag{5.47}$$

An initial assumption for the cause of large errors is the choice of angle to perform the extraction process. High errors are expected near $\theta = 0^\circ$ because parallel and perpendicular polarizations are identical at normal incidence. In addition, high errors are expected at $\theta = 90^\circ$ due to the impracticality of plane wave incidence completely tangential to the MUT. However, outside of the cases of $\theta = 0^\circ$ and $\theta = 90^\circ$ a surprising result is found when one plots the amplification factors for μ_r', μ_r'', ϵ_r', and ϵ_r'' from $\theta = 0^\circ$ and $\theta = 90^\circ$. From Figure 5.2, it is seen that the amplification factors for μ_r', μ_r'', ϵ_r', and ϵ_r'' are insensitive to choice of angle once θ is chosen sufficiently away from $\theta = 0^\circ$ and $\theta = 90^\circ$.

From Section 5.2.1, it was noted that the denominator in equation (5.20) can potentially lead to high errors due to cancelation effects, which in turn create large increases in the amplification factors. In fact the denominator in (5.20) is the primary source of error due to angle. The denominator of (5.20) can be found in the amplification factor in equations (5.45) and (5.46) via equation (5.47). The denominator in (5.20) can be separated into its real and imaginary parts as $\left(1 - Y_r \cos^2\theta\right) - jY_i \cos^2\theta$. Examination of this expression shows that Y_r and Y_i are the only quantities that can be controlled to prevent the real and imaginary parts from approaching zero. Recalling the fact that the term Y (defined in (5.15)) is essentially a product of $\Gamma_\perp$ and $\Gamma_\parallel$, Y can be controlled by the level of impedance mismatch (or media contrast) of the overlay and the MUT. In Figure 5.4, it is shown that as $\bar{\epsilon}_r$ increases the real part and the imaginary part of the denominator of (5.20) grow. This effect then causes rapid decrease in (5.20) as also shown in Figure 5.4. Therefore, as the contrast between the overlay and the MUT is decreased, the denominator in (5.20) is less prone to cancelation, and (5.45) and (5.46) are less likely to grow.

5.3.2 Errors due to inaccuracies in measured Δ

Errors introduced by imperfect knowledge of the sample thickness can be found by examining the amplification factors $\partial\mu_r/\partial\Delta$ and $\partial\epsilon_r/\partial\Delta$. Computing the derivatives (5.43) and simplifying the results gives

$$\frac{\partial\mu_r}{\partial\Delta} = \mu_r(F_\Delta + G_\Delta), \quad \frac{\partial\epsilon_r}{\partial\Delta} = \epsilon_r(F_\Delta - G_\Delta) \tag{5.48}$$

where

$$F_\Delta = 0 \tag{5.49}$$

$$G_\Delta = \frac{4jk_z P^2}{Q\left(1+P^2\right)^2}. \tag{5.50}$$

In general, the dual-polarization method is fairly insensitive to inaccuracies in measurement of MUT thickness. In fact, error due to measurement of Δ is not important until error due to θ, $\Gamma_\perp$, and $\Gamma_\parallel$ are sufficiently decreased.

However, there are certain material thicknesses where error due to Δ will become substantial. Equation (5.50) can be rewritten as $\frac{4k_zP^2}{\tan(k_z\Delta)\left(1+P^2\right)^2}$, where it can be shown that $Q = j\tan(k_z\Delta)$. With this formulation of (5.50), it can seen that when k_z is nearly real, (5.50) will be large when $\Delta = \frac{n\pi}{k_z}$ where $n = 1, 2, 3 \ldots$.

5.3.3 Errors due to inaccuracies in measured $\Gamma_\perp$ and $\Gamma_\parallel$

Accurate measurement of $\Gamma_\perp$ and $\Gamma_\parallel$ is essential in the extraction of material parameters with the dual-polarization method. In order to examine the error in extracted material parameters, the derivatives from (5.43) must be computed and analyzed for both the magnitude and phase of $\Gamma_\perp$ and $\Gamma_\parallel$. The contribution of the error caused by both the magnitude and phase of $\Gamma_\perp$ and $\Gamma_\parallel$ will be called collectively analyzer error, and its standard deviation will be computed as:

$$\sigma_\mu = \sqrt{\sum_{a=1}^{2} \sigma_a \left(\sum_{n=1}^{2} \frac{\partial \mu}{\partial a_n} \right)} \tag{5.51}$$

$$\sigma_\epsilon = \sqrt{\sum_{a=1}^{2} \sigma_a \left(\sum_{n=1}^{2} \frac{\partial \epsilon}{\partial a_n} \right)}. \tag{5.52}$$

Here $n = 1$ represents $\perp$, $n = 2$ represents $\parallel$, $a = 1$ represents $\angle\phi$, and $a = 2$ represents $|\Gamma_n|$, with $\Gamma = |\Gamma|\angle\phi$. To compute (5.43) for the analyzer amplification factors, the terms $F_{a_n} = \frac{1}{2}\frac{\cos^2\theta}{1-Y\cos^2\theta}\frac{\partial Y}{\partial a_n}$ and $G_{a_n} = \frac{1}{2X}\frac{\partial X}{\partial a_n} - \frac{1}{Q}\frac{\partial Q}{\partial a_n}$ are used. In (5.53)-(5.55), $N_1 = \frac{1+\Gamma_n}{1-\Gamma_n}$ and $N_2 = \frac{\cos\phi + j\sin\phi}{(1-\Gamma_n)^2}$, where

$$\frac{\partial X}{\partial a_n} = \begin{cases} 2j|\Gamma_n|N_1N_2 & a_n = 1 \\ 2N_1N_2 & a_n = 2 \end{cases} \tag{5.53}$$

$$\frac{\partial Y}{\partial a_n} = \begin{cases} 2j|\Gamma_1|N_1N_2 & a = 1 \\ \frac{2j|\Gamma_2|N_2}{N_1} & a = 1 \\ -N_1N_2 & a = 2, i = 1 \\ \frac{N_2}{N_1} & a = 2, n = 2 \end{cases} \tag{5.54}$$

$$\frac{\partial Q}{\partial a_n} = \frac{2jdk_0^2P^2}{\left(1+P^2\right)^2}\frac{\sin^2\theta\cos^2\theta}{\left(1-Y\cos^2\theta\right)^2}\frac{\partial Y}{\partial a_n}. \tag{5.55}$$

Error due to analyzer uncertainty in the dual-polarization method can be substantial. One reason for the large amount of error is the presence of the term $1-Y\cos^2\theta$ term as explained in Section 5.3.1. This term is present in F_{a_n} and in (5.55). Another reason analyzer error can be substantial is due to the term $1-\Gamma_n$, which is present in each N_1 and N_2 term, and subsequently in each F_{a_n} and G_{a_n}. The reason $1-\Gamma_n$ is especially troublesome is again due to cancelation effects. The magnitude of Γ_n is bounded between 0 and 1. Thus, depending on the impedance match of the overlay and the MUT, $1-\Gamma_n$ can potentially become very small and F_{a_n} and G_{a_n} large. Increasing $\bar{\epsilon}_r$ can help decrease the effect of analyzer error. However, analyzer error can still remain substantial relative to error due to θ and Δ uncertainty even if the impedance mismatch between the overlay and the MUT is decreased because reflection from the conductor backing can force the magnitude of Γ_n to unity. This again makes $1-\Gamma_n$ small. However, reflection from the conductor can potentially be reduced when the MUT thickness is such that the phase change in Γ_n makes $1-\Gamma_n \neq 0$, or if there is sufficient absorption to make $|\Gamma_n|$ small.

5.4 Numerical Experiments

In order to examine the feasibility of the dual-polarization method to perform extraction of ϵ_r and μ_r, error analysis of two sample materials has been undertaken. The error analysis was performed generating synthetic reflection coefficients that would be measured in real application of the the dual-polarization method. Synthetic ϵ_r and μ_r values were then computed using the dual-polarization extraction scheme described in Section 5.2. The error propagation method or Monte Carlo simulations were then implemented as necessary. All programming was done in Matlab. The measurement uncertainties for θ, Δ, $|\Gamma_n|$, and ϕ_n are given in Table 5.1. The uncertainties for $|\Gamma_n|$, and ϕ_n were taken from [21].

5.4.1 Error Analysis of Plexiglas

Plexiglas is a well known transparent thermoplastic. Plexiglas was chosen as an initial MUT because it is non-magnetic and has low loss. The MUT is assumed to have $\Delta = 1$in. with $\theta = 45^\circ$. The material parameters of plexiglas are in Table 5.3 and were taken from [13].

The error due to uncertainties in θ, Δ, analyzer error, and the total error for plexiglas are presented in Figure 5.5. The error shown in Figure 5.5 is done by performing 100,000 Monte Carlo trials.

Figure 5.5 shows that extraction of μ_r' and μ_r'' for Plexiglas is relatively insensitive to uncertainty for the dual-polarization method, with the total standard deviations being .18 and .23 respectively.

However, the extraction of ϵ_r' and ϵ_r'' show much more sensitivity to the dual-polarization method measurement uncertainties. Figure 5.5 shows that the largest contributor to the error of ϵ_r' and ϵ_r'' is analyzer error. Considering that errors due to analyzer uncertainty and uncertainties in θ are both dependent on impedance matching between the overlay and MUT as described in Sections 5.3.1 and 5.3.3 and error due to uncertainty in θ is not substantial, the bulk of the error due to analyzer uncertainty must be from cancelation in N_1 and N_2 (defined in Section 5.3.3). Figures 5.6 and 5.7 are plots of the error due to uncertainty in analyzer vs. the thickness of the MUT for ϵ_r and μ_r respectively. From Figures 5.6 and 5.7, it can be seen that are 4 distinct thicknesses where the error spikes. These thicknesses correspond to points where $\phi_\perp$ and $\phi_\|$ equal zero as in Figure 5.8. If one chooses to recalculate the error for the point in Figures 5.6 and 5.7 where the analyzer uncertainty is the smallest, much better results can be achieved as shown in Figure 5.9.

5.4.2 FGM40

FGM40 is a broadband silicone absorber. It can be used in various applications such as improving radar performance, reducing radar cross section, and reducing specular reflections [1]. FGM40 was chosen as a second example for a MUT because performance knowledge of the dual-polarization method with a high-loss magnetic material was desired. Also, it is common for a material like FGM40 to be used is shielding applications. The material parameters of FGM40 are given in Table 5.4. Also, $\Delta = 40$ mils and $\theta = 45^{\circ}$ are used.

The total error for FGM40 is shown in Figure 5.12. The errors were calculated with 100,000 Monte Carlo trials because the error propagation method provides an overestimation of error.

Figure 5.10 shows that both the real and imaginary parts of μ_r and ϵ_r are sensitive to extraction with the dual-polarization method. Again, error due to analyzer uncertainty is very high, especially for ϵ_r' and ϵ_r''. However, error due to θ uncertainty is much more of a contributing factor, especially for μ_r' and μ_r''.

Initially, one may think that the error due to analyzer uncertainty for FGM40 is associated with reflection off of the conductor backing like for Plexiglas as described in Section 5.4.1. However, this is not the case for FGM40. FGM40 is such a lossy material that there is a substantial amount of attenuation before waves reach the conductor backing.

Considering the increase in error due to uncertainties θ when compared to the errors calculated for Plexiglas, a majority of the error must be from the impedance mismatch between the overlay and the MUT, as described in Section 5.3.1. Figure 5.11 is a plot of the standard deviation for ϵ_r and μ_r due to θ uncertainty vs. the dielectric constant of the outside medium, $\bar{\epsilon}_r$. It shows that as $\bar{\epsilon}_r$ increases there is a rapid decrease in error. Table 5.5 then shows the decrease in total error for values of $\bar{\epsilon}_r$ of 1, 10, and 20. Figure 5.12 shows the breakdown of the error when $\bar{\epsilon}_r = 20$; this shows that error due to uncertainties in θ and analyzer uncertainties are still substantial. The only way to gain marked improvement in error due to θ and analyzer uncertainties is to create an even better impedance match by making the overlay a magnetic medium.

5.5 Conclusions

The dual-polarization method for characterization of both ϵ_r and μ_r is examined. Although the dual-polarization method can be formulated for dielectrics with unknown thickness or dielectrics with known thickness, the focus of this chapter is on characterizing conductor-backed media for both ϵ_r and μ_r.

Thorough analysis of the error propagated into the extraction of ϵ_r and μ_r by uncertainties in angle, thickness, and reflection coefficients has been conducted. Analysis has shown that the dual-polarization method can be very sensitive to uncertainties in angle and reflection coefficients, but relatively insensitive to uncertainties of MUT thickness. However, in very specific situations, the dual-polarization method have been can be applied accurately.

Measured Parameter	Tolerance (Standard Deviation)
Thickness, Δ	$\sigma_{\Delta} = 1$ mil
Angle of Incidence, θ	$\sigma_{\theta} = .5^{\circ}$
Magnitude of Γ, $\lvert\Gamma_n\rvert$	$\sigma_{\lvert\Gamma_n\rvert} = .004$
Phase of Γ_n, $\angle\Gamma{=}\phi_n$	$\sigma_{\phi_i} = .8^{\circ}$

Table 5.1: Measurement tolerances chosen for error analysis for two polarization method

μ_r'	μ_r''	ϵ_r'	ϵ_r''
1	0	2.65	.0076

Table 5.2: Material parameters for Plexiglas at 8.20 GHz

μ_r'	μ_r''	ϵ_r'	ϵ_r''
1	0	2.65	.0076

Table 5.3: Material parameters for Plexiglas at 8.20 GHz

μ_r'	μ_r''	ϵ_r'	ϵ_r''
2.08	2.53	21.86	.389

Table 5.4: Material parameters for FGM40 at 8.20 GHz

$\bar{\epsilon}_r$	μ_r'	μ_r''	ϵ_r'	ϵ_r''
1	2.12	4.45	12.52	13.24
10	1.13	.99	6.71	7.74
20	.45	.45	3.94	3.55

Table 5.5: Decrease in total error for FGM40 with increase of $\bar{\epsilon}_r'$

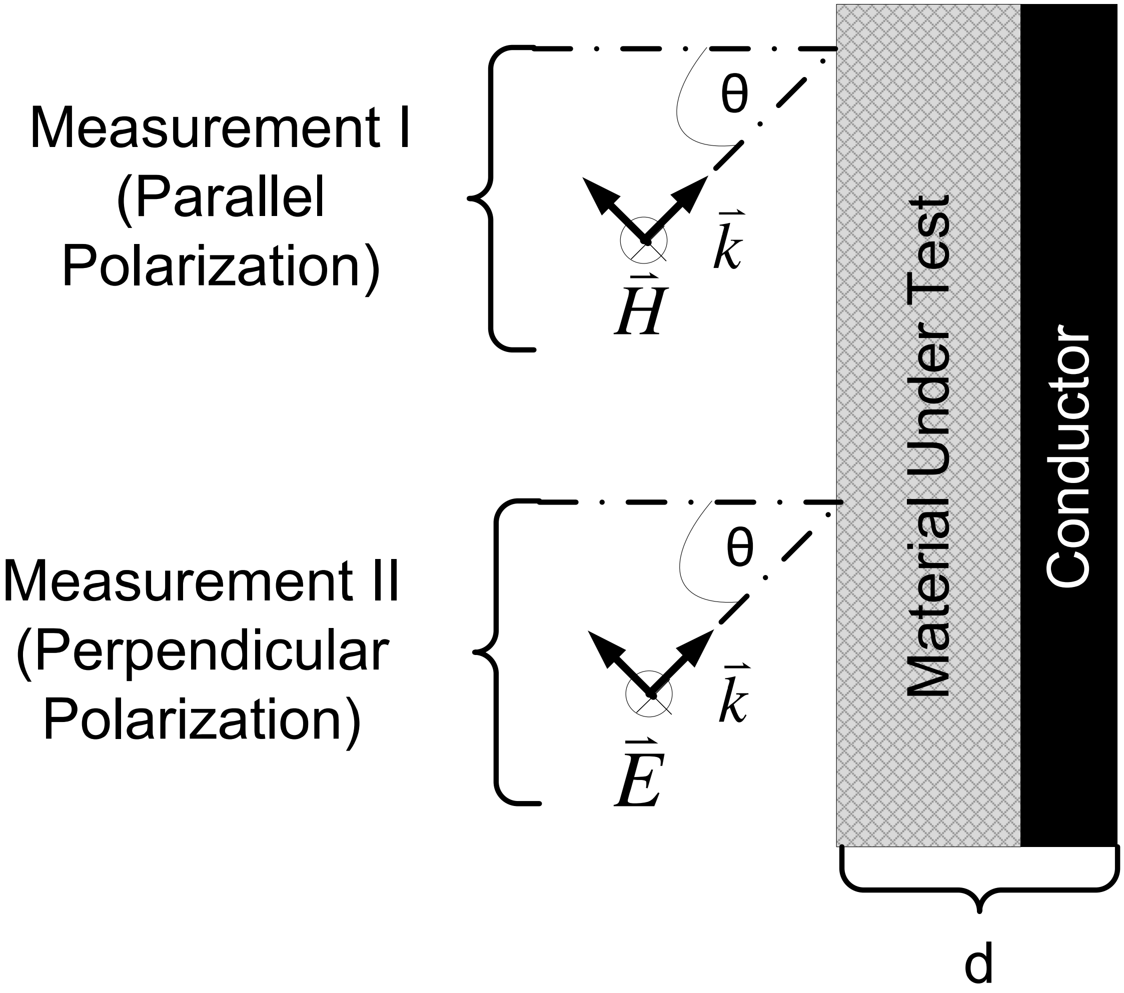

Figure 5.1: Diagram illustrating the dual-polarization method

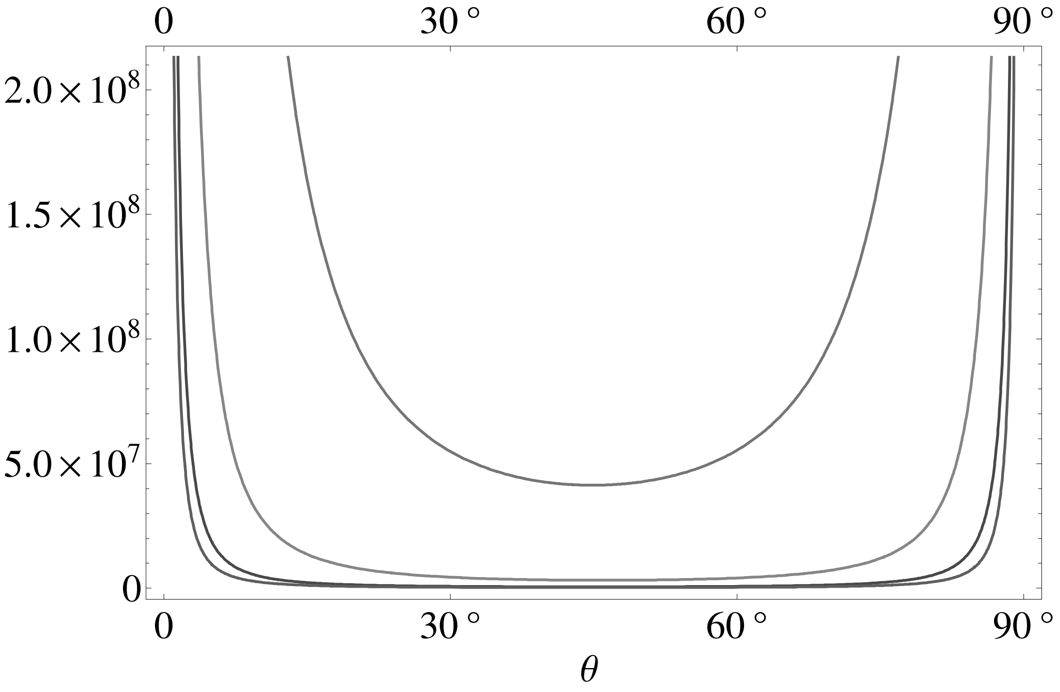

Figure 5.2: Amplification factors for μ'_r, μ''_r, ϵ'_r, and ϵ''_r vs. θ

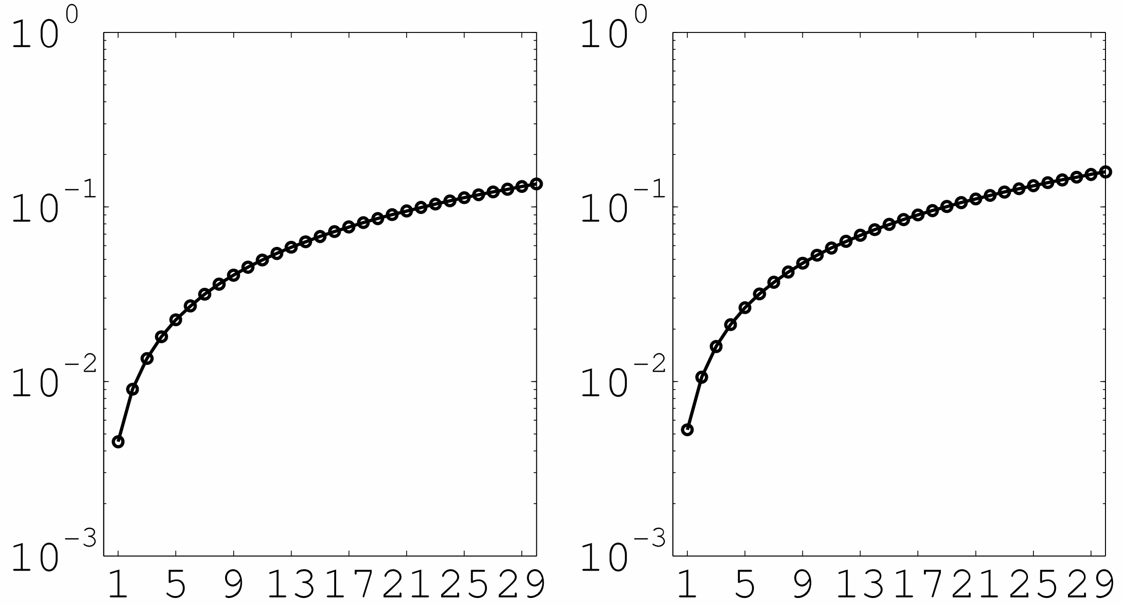

Figure 5.3: Denominator of Equation 5.20 vs. $\bar{\epsilon}_r$

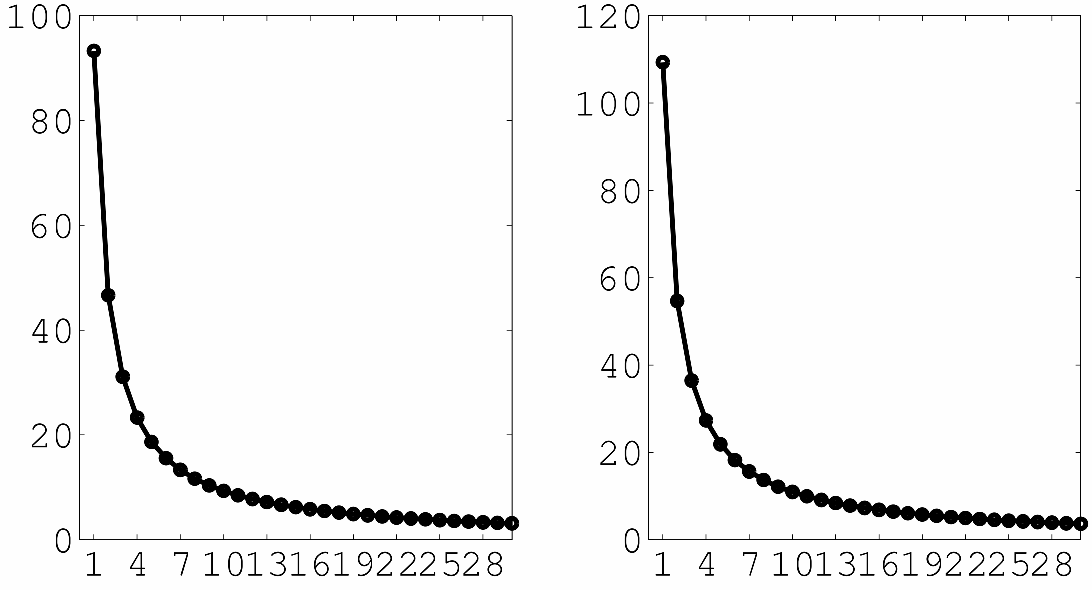

Figure 5.4: Equation 5.20 vs. $\bar{\epsilon}_r$

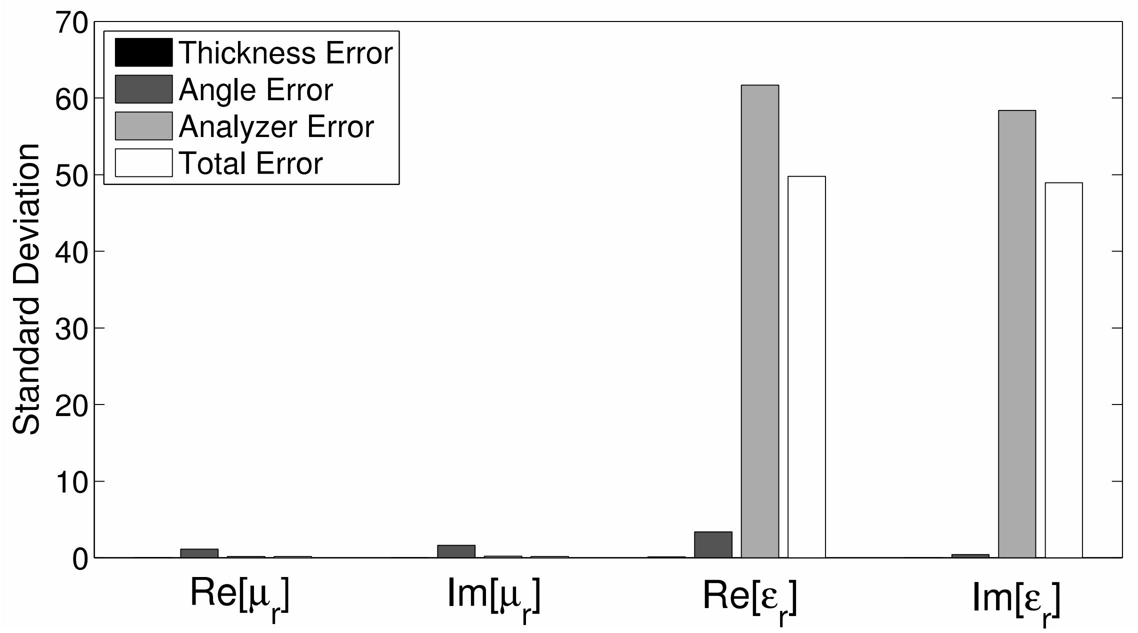

Figure 5.5: Error for Plexiglass

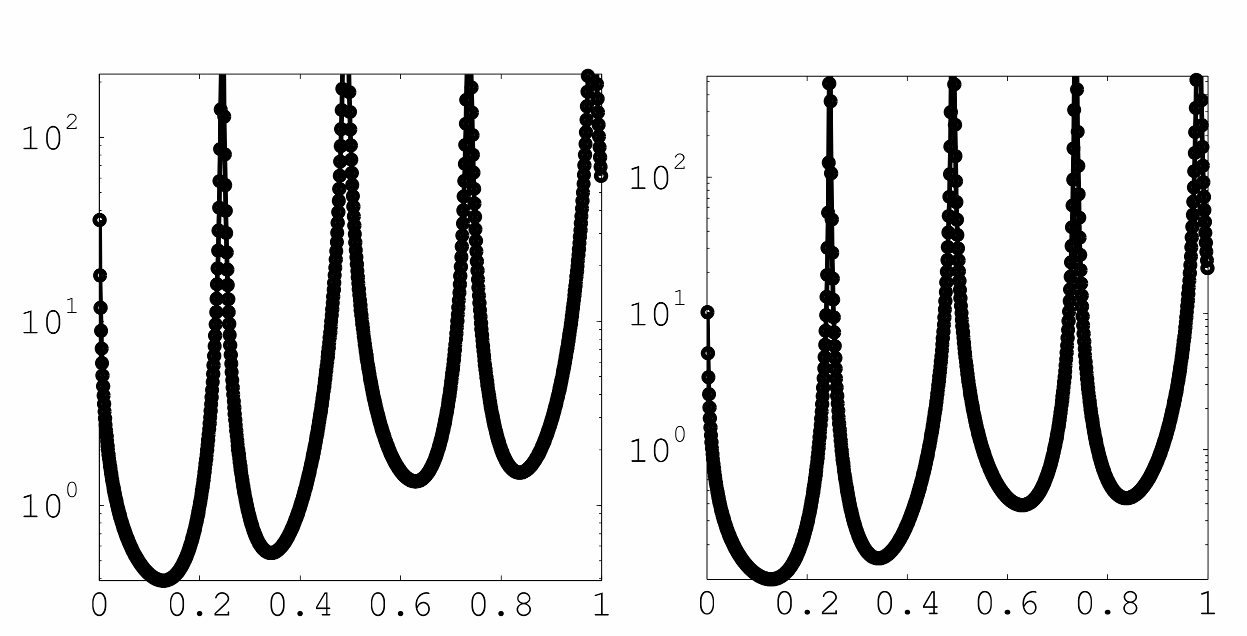

Figure 5.6: Analyzer error of Plexiglass vs. MUT thickness

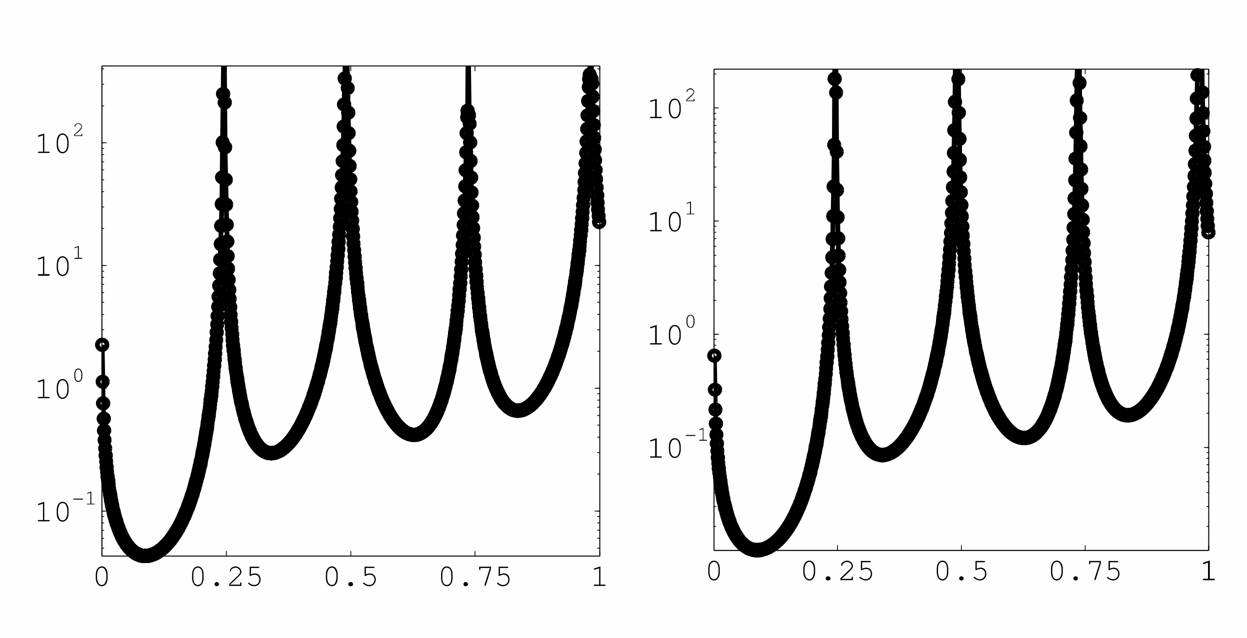

Figure 5.7: Analyzer error of Plexiglass vs. MUT thickness

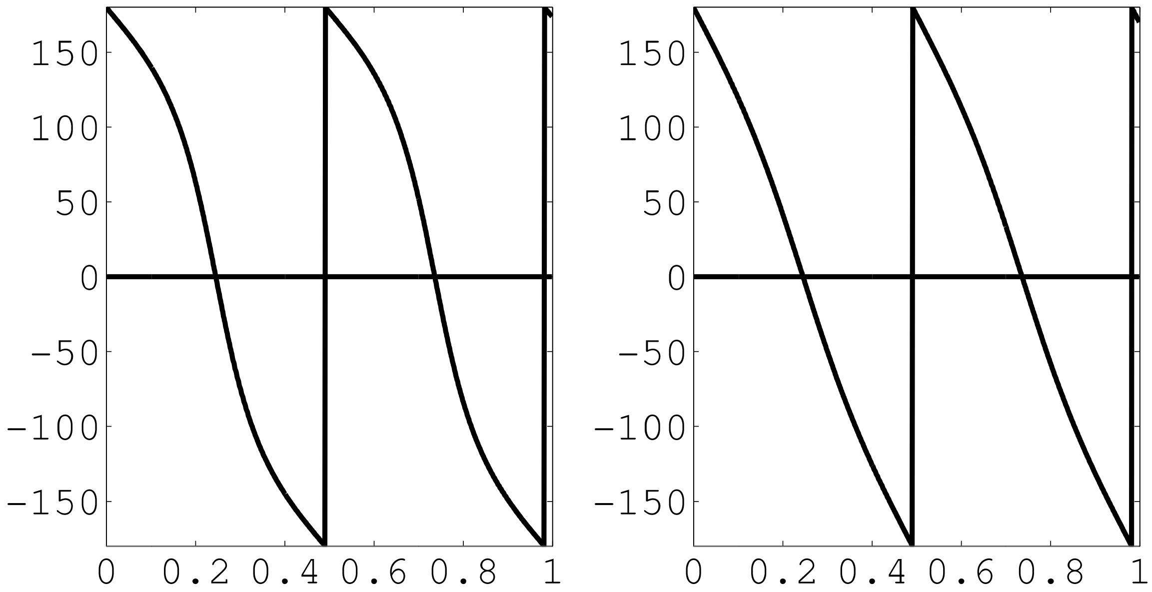

Figure 5.8: Change in phase for $\Gamma_\perp$ and $\Gamma_\parallel$ vs. MUT thickness (Plexiglas)

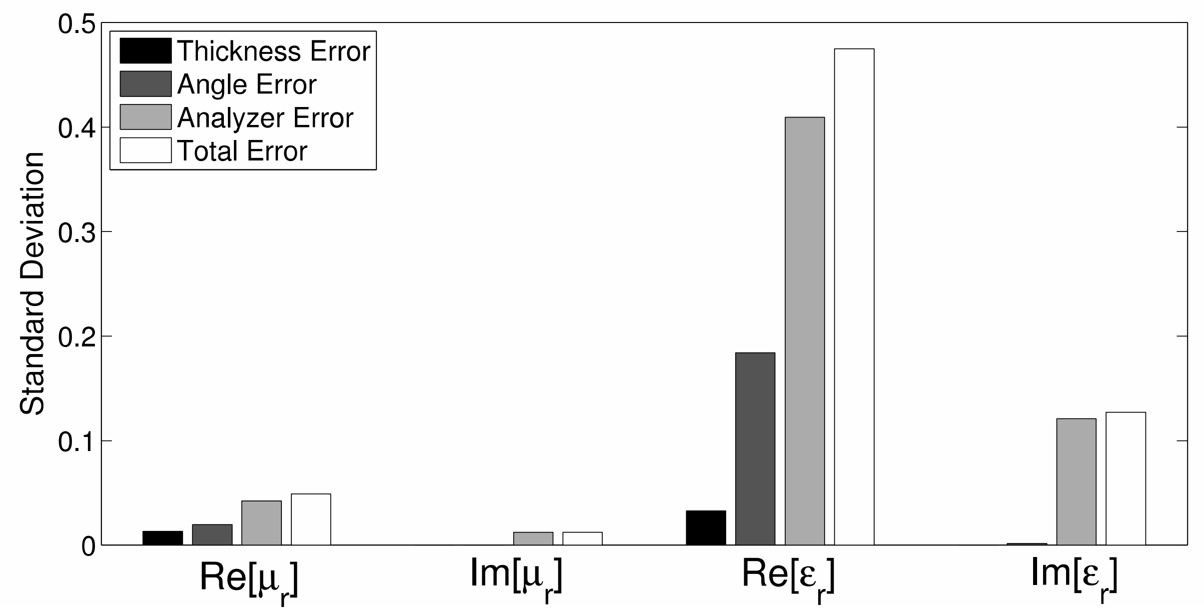

Figure 5.9: Error for Plexiglass for $\Delta = .1$ inch

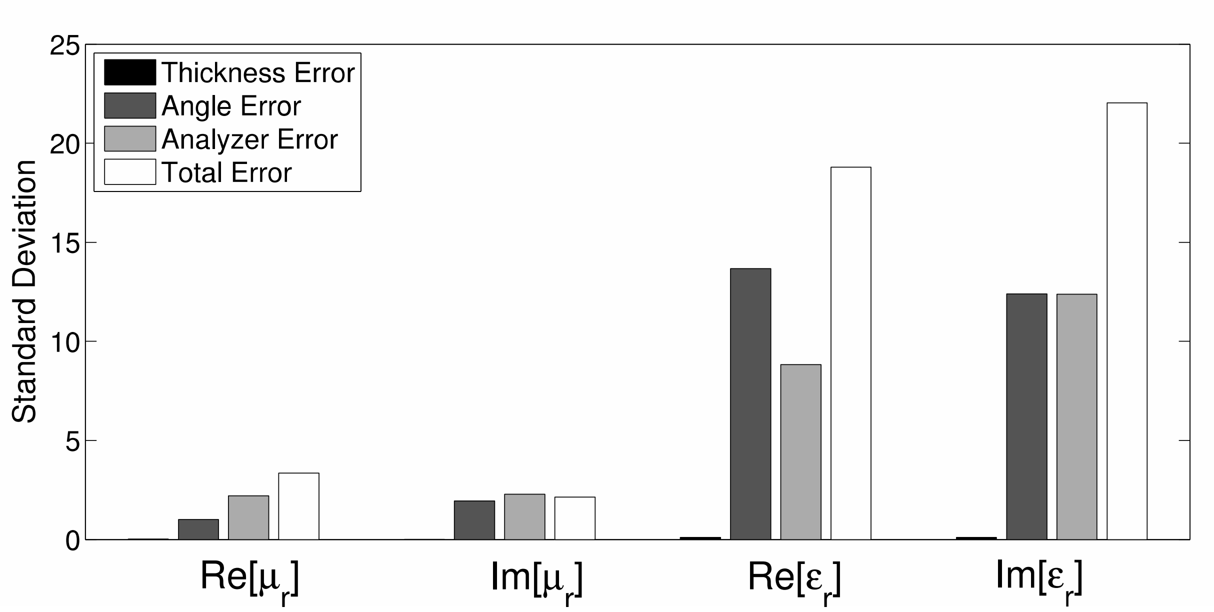

Figure 5.10: Error for FGM40

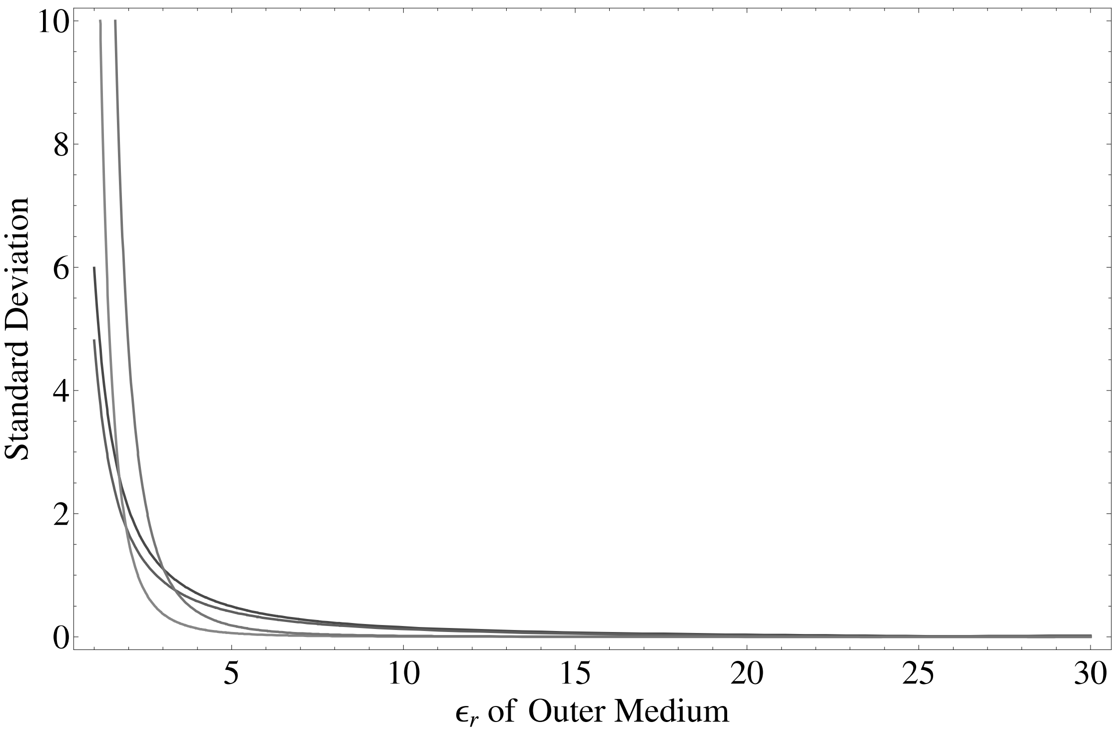

Figure 5.11: Decrease in error vs. increase of $\bar{\epsilon}'_r$

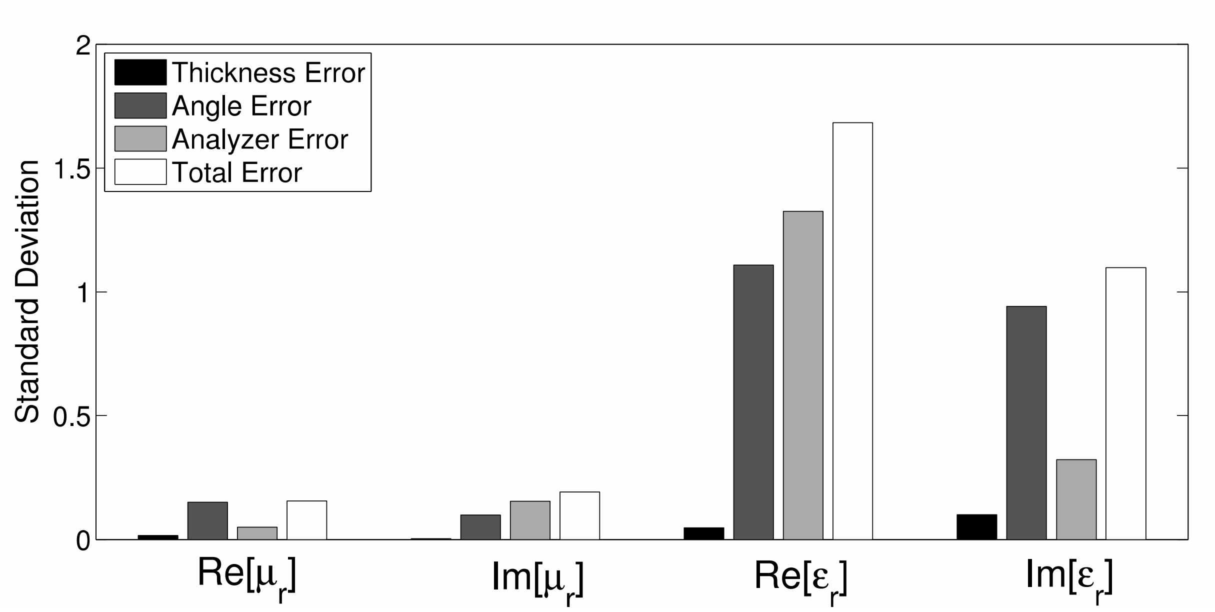

Figure 5.12: Error for FGM40 for $\bar{\epsilon}_r = 20$

Chapter 6

Interval Analysis

6.1 Introduction

Interval analysis is the mathematics of sets of numbers. A set or interval can be the set of all real numbers, a range of specified integers, the empty set, etc. Given a defined interval, interval analysis forms the rules of interval arithmetic and interval extensions .

Interval analysis was initially introduced in the thesis of R.E. Moore in [36]. One of the initial uses of interval arithmetic was to create bounds on machine calculations. For example, there are many different ways to represent a number within a programming language such as short, long, etc. As calculations are performed on different representations of numbers, a large amount of error can be inserted into a final computation. Thus, interval arithmetic has been used as a way to reduce error in computer calculations by bounding solutions.

Today interval analysis is being used in a variety of applications. Interval analysis has been used to solve various computer graphic issues [51], design analog integrated circuits [32], study economic utility analysis [34], and design of robots [25].

An increasing area of interest for interval analysis is its use for error analysis. Accurate error analysis is needed in various areas in electromagnetics as demonstrated in [43], [27], and [30]. Traditional error analysis methods include, but are not limited to, the error propagation method and Monte Carlo methods both of which can suffer from several computational issues as described in Chapter 3. Interval analysis is a suitable error analysis tool because the output interval directly quantifies the impact of propagated uncertainties [35]. In addition, interval analysis is quick and easy to implement. There are several software packages available that implement interval arithmetic. A popular package for interval analysis computations is Intlab. Intlab is a Matlab extension developed by Sigfried M. Rump [48]. Intlab utilizes outward rounding and performs computations on functions of interval arguments (discussed in section 6.2.1). For more about Intlab, one is encouraged to seek [19] and [48].

The major contribution of this chapter is to demonstrate the use of interval analysis as a tool for error analysis for material characterization methods. When attempting to measure the permittivity and permeability of a material in a laboratory, error inserted into the extraction is unavoidable. Therefore, it is crucial to know to what degree the extracted permittivity and permeability are valid. With the use of interval analysis, the parameters used in the measurement setup can be formed into intervals based on the instrument tolerances. Then the final solutions are intervals that give the exact bounds for the permittivity and permeability.

This chapter presents use of interval mathematics for use in error analysis of material characterization methods. An overview of interval mathematics is presented. In addition, example use of interval analysis is presented for error analysis of the free-space implementation of the layer-shift method which is described in Chapter 4.3.2. In these examples, measured permittivity and permeability data are shown combined with calculated interval bounds.

6.2 Background of Interval Analysis

6.2.1 Introduction to Interval Functions

Interval Notation

The essential concept of interval analysis is to perform computations with intervals of real numbers instead of real numbers themselves [19]. Again, an interval is simply a range of numbers or values. For example, the interval X can be represented as

$$[\underline{X}, \overline{X}] = \{x \in \mathbb{R} : a \leq x \leq b\}. \tag{6.1}$$

In interval analysis, the intervals are always closed sets with the endpoints included within the interval. It is common for capital letters to represent intervals and for lowercase letters to represent members of intervals. This particular representation of intervals is called infimum/supremum representation. Infimum/supremum representation entails that the lower and upper endpoints are referred to as the infimum and supremum respectively. In this chapter the infimum will be denoted with an underline, and the supremum will be denoted with an overline. Intervals can also be represented with their midpoint and radius. The midpoint of an interval is the point in the center of the interval defined as $m(X) = \frac{\left(\underline{X}+\overline{X}\right)}{2}$. The radius is simply half the width of the interval, which is $r(X) = \frac{\overline{X}-\underline{X}}{2}$. The midpoint-radius form is then

$$X =< m, r >, x \in \mathbb{R}. \tag{6.2}$$

Interval analysis utilizes computation of sets. Solutions to problems are considered enclosures, which are intervals that are guaranteed to include the true solution. In order to ensure an interval is an enclosure during machine calculations, rounding is performed in such a way that the lower bound always moves to the left and the upper bound always moves to the right at the last digit. This is termed *outward rounding*.

Interval Functions

There are two main classifications of functions in interval analysis. The first classification of interval functions are *united extensions.* United extensions are functions that are created by taking a real-valued function f and computing the range of values $f(x)$ takes as x is varied through an interval X [37]. United extensions are denoted as $\bar{f}(X)$. United extensions result in the set image of $f(X)$ which is defined by

$$\bar{f}(X) = \left\{f(x) : x \in X\right\}. \tag{6.3}$$

The other type of interval functions are *interval-valued extensions*, or shortly termed interval extensions. Interval extensions are created by directly extending an ordinary real-valued function to interval arguments [37]. Common notation for an interval extension of a function f is F. Although there is not a unique interval extension for a specific real-valued function, any interval extension is valid as long as when a degenerate interval (an interval with the same lower and upper bounds) is plugged into the interval extension then the correct value for the real-valued function is retrieved, i.e.,

$$F([x,x]) = f(x). \tag{6.4}$$

In order to make clear the difference between a united extension and a interval extension consider the real-valued function $f(x) = x(x-1)$ where $x \in X : X = [0,1]$. If one evaluates $\bar{f}(x)$ over X, one will find the united extension $\bar{f}(X) = \left[-\frac{1}{4}, 0\right]$. Now consider the interval extension of $f(x)$, $F(X) = X(X-1)$. When one calculates $F(X)$ for $X = [0,1]$, one finds $F(X) = [-1,0]$. This examples demonstrates the fundamental theorem of interval analysis. The fundamental theorem of interval analysis states that if F is an inclusion isotonic interval extension of f, then the range of f is a subset of the set F [37], i.e.,

$$f\left(X_1,\ldots,X_n\right) \subseteq F\left(X_1,\ldots,X_n\right). \tag{6.5}$$

6.2.2 Overview of Interval Arithmetic

Since intervals are sets, operations that are associated with sets are applicable to intervals. For example, the intersection of two intervals, X and Y, is defined by

$$X \cap Y = [\max\{\underline{X}, \underline{Y}\}, \min\{\overline{X}, \overline{Y}\}]. \tag{6.6}$$

However, if X and Y have no points in common or either $\overline{Y} < \underline{X}$ or $\overline{X} < \underline{Y}$ are true, then the intersection of X and Y yields the empty set, $\emptyset$. The union of two intervals X and Y is the points shared and included in X and Y as defined by

$$X \cup Y = \left[\min\{\underline{X}, \underline{Y}\}, \max\{\overline{X}, \overline{Y}\}\right]. \tag{6.7}$$

If X and Y have no points in common an interval cannot be formed with intersection. Nonetheless, an interval can be formed with what is called the *interval hull.* The interval hull is a subset of the intersection of two intervals and is defined by

$$X \underline{\cup} Y = \left[\min\{\underline{X}, \underline{Y}\}, \max\{\overline{X}, \overline{Y}\}\right]. \tag{6.8}$$

For interval arithmetic to be well-defined the basic operations of addition, subtraction, and division must be defined. All of these operations can be generally defined with $X \odot Y = \{x \odot y : x \in X, y \in Y\}$ for $\odot \in \{+, -, \times, \div\}$. The endpoint formulas for addition, substraction, multiplication, and division are:

$$X + Y = [\underline{x} + \underline{y}, \overline{x} + \underline{y}] \tag{6.9a}$$

$$X - Y = [\underline{x} - \overline{y}, \overline{x} - \underline{y}] \tag{6.9b}$$

$$X \times Y = [\min\{S\}, \max\{S\}] \tag{6.9c}$$

$$X \div Y = X \times \frac{1}{Y}. \tag{6.9d}$$

Here the set S is defined as $S = \{\underline{x}\underline{y}, \underline{x}\overline{y}, \overline{y}\underline{x}, \overline{x}\overline{y}\}$. In addition, $\frac{1}{Y} = [\frac{1}{\overline{y}}, \frac{1}{\underline{y}}]$ as long as $\underline{y} > 0$ or $\overline{y} < 0$. Thus, division by an interval containing zero is not defined. For a more complete treatment of interval arithmetic one is encouraged to consult [37].

6.2.3 Complex Intervals

Naturally, in the course of studying many engineering applications, especially in electromagnetic theory, complex numbers will be encountered. This section will review the three different ways to represent complex numbers in interval analysis and will present pertinent arithmetic properties in each representation.

Rectangular Representation

A rectangular interval is represented with intervals for the real and imaginary parts separately as in (6.10). As the name suggests, a rectangle is constructed in the complex plane as illustrated in Figure 6.1 with rectangular representation. The equation for a rectangular interval is composed of individual intervals for the real and imaginary parts as

$$Z = X + \jmath Y = \left\{x + \jmath y : x \in X, Y \in Y\right\}. \tag{6.10}$$

In general, addition/subtraction are very accurate with rectangular complex intervals. Addition and subtraction of rectangular intervals are performed with similar endpoint formulas as in Section 6.2.2 on the real and imaginary parts of the interval individually. However, multiplication/division in rectangular representation usually provides an overestimation in the resulting interval and is avoided [19].

Circular Representation

Another way to represent complex intervals is with circular arithmetic which was originally formulated in [18]. In order to convert from a rectangular interval to a circular interval, one must calculate the midpoint, a, and radius, r, of the circle. This process is similar to converting from infimum/supremum representation to midpoint/radius representation. One then represents the complex interval as

$$Z = \langle a, r \rangle = \{ z \in C : |z - a| \leq r \}, \tag{6.11}$$

which is portrayed in Figure 6.2. Unfortunately, addition/subtraction provides an overestimation in circular arithmetic. Circular arithmetic is especially useful for multiplication/division. Multiplication of circular complex intervals is defined as

$$Z_1 \times Z_2 = \langle a_1 \times a_2, |a_1| r_2 + |a_2| r_1 + r_1 r_2 \rangle. \tag{6.12}$$

Sector Representation

When parameters are encountered in polar form (i.e., reflection coefficients or impedances), it is useful to use sector representation. In sector representation as found in [26], the interval is represented with a radius, r, and an angle, w. Common notation for sectors is

$$Z = R \cdot e^{J \cdot W} := \left\{ r \cdot e^{J\, w} | r \in R, w \in W \right\}. \tag{6.13}$$

Sectors form arcs in the complex plane as depicted in Figure 6.3. Utilization of complex sector intervals often involves converting to circular or rectangular complex intervals to perform arithmetic operations and then conversion back to sector intervals.

6.3 Interval Sensitivities and Statistical Analysis

6.3.1 Interval Sensitivities

When performing an error analysis with interval analysis, the sensitivity interval is desired. The sensitivity interval is the interval which represents the lower and upper bounds for the parameter on which error analysis is being performed. Thus, the sensitivity interval represents the absolute bounds of a parameter and the radius of the sensitivity interval quantifies the impact of the propagation of errors in an experiment. In the cases presented in this work, the parameter can be ϵ_r or μ_r and will be represented in infimum/supremum representation as

$$\epsilon_r' = [\underline{\epsilon_r'}, \overline{\epsilon_r'}] \tag{6.14a}$$

$$\epsilon_r'' = [\underline{\epsilon_r''}, \overline{\epsilon_r''}] \tag{6.14b}$$

$$\mu_r' = [\underline{\mu_r'}, \overline{\mu_r'}] \tag{6.14c}$$

$$\mu_r'' = [\underline{\mu_r''}, \overline{\mu_r''}] \tag{6.14d}$$

.

To calculate the sensitivity interval, the original extraction equations for ϵ_r and μ_r are adapted for interval analysis by creating interval extensions. Unfortunately, sensitivity intervals can be an overestimation of the most probable bounds of ϵ_r and μ_r. Overestimation can occur with interval arithmetic operations such as multiplication of rectangular intervals [19]. The primary method of overcoming overestimation is *refinement*. Refinement is a process of sub-dividing an interval X into n smaller intervals, X_i, where $X_i \subseteq X$. The values of the interval extensions are then computed for each sub-interval, $F(X_i)$. Finally, the interval hull of all the $F(X_i)$ is taken to find an interval with a smaller radius which still contains the united extension $\bar{f}(X)$.

6.3.2 Interval Analysis Used as a Statistical Analysis Tool

The intent of error analysis is to determine the experimental uncertainty in a measurement process due to random errors. Assuming that a data set is normally distributed, random error in an experimental process is quantified by the standard deviation [53]. Standard deviation is thus a measurement of how much variation exists from the mean or expected value; the higher the standard deviation the more variance is found in a data set and vice versa. In order to implement interval analysis as an alternate method for error analysis, standard deviations predicted by interval analysis should match standard deviations predicted by other well-known statistical methods, like Monte Carlo simulations. Hence, the standard deviation and mean calculated with Monte Carlo simulations are compared to the radius and midpoint of the sensitivity interval respectively.

6.4 Error Analysis of the Layer-Shift Method

The layer-shift method is a well known material characterization method which was originally developed in [3]. The layer-shift method is performed by measuring the reflection coefficient twice, once with the MUT backed directly by a metal plate, and again with a spacer placed in between the MUT and the metal plate. The layer-shift method can be performed with free-space, coaxial, and waveguide implementations. The methodology of the layer-shift method is displayed in Figure 4.5 and explained in Section 4.3.2. In [10], the method is noted for being particularly good for characterizing dielectric media.

This section demonstrates how interval analysis can be used to predict the sensitivity of extracted μ and ϵ values using the layer-shift method. Analysis is shown for free-space implementation of the method.

6.4.1 Extraction Equations for the Free-Space Layer-Shift Method

In order to extract μ and ϵ using the layer-shift method, several parameters must be computed. From Sections 4.2.3 and 4.3.2, μ_r and ϵ_r are calculated from

$$\epsilon_r = \frac{k_{z2}\eta_0}{k_0 Z_2}, \mu_r = \frac{k_{z2}^2 + k_0^2 \sin^2\theta}{k_0^2 \epsilon_r}, \tag{6.15}$$

for TM polarization and

$$\mu_r = \frac{k_{z2} Z_2}{k_0 \eta_0}, \epsilon_r = \frac{k_{z2}^2 + k_0^2 \sin^2\theta}{k_0^2 \mu_r} \tag{6.16}$$

for TE polarization.

In equations (6.15-6.16), the intrinsic impedance, η_0, and the wavenumber, k_0, are determined by the medium which the plane waves originate. Here η_0 and k_0 are the free-space values and the subscript 2 denotes the MUT region.

To solve equations (6.15-6.16), two parameters must be calculated: (1) the impedance of the interface between the MUT and the metal plate or the spacer ,Z_2, and (2) the wave vector for the MUT in the z-direction, k_{z2}. Through calculation of the transverse impedance of each region and the interfacial reflection coefficients, Z_2 and k_{z2} can be found with:

$$Z_2 = \frac{Z_3^b Z_1^a(z_1) Z_1^b(z_1)}{Z_3^b + Z_1^a(z_1) - Z_1^b(z_1)} \tag{6.17}$$

$$k_{z2} = \frac{1}{\delta} \tan^{-1}\left(-\jmath \frac{Z_1^a(z_1)}{Z_2}\right) \tag{6.18}$$

where

$$Z_1^a = Z_0 \frac{1+\Gamma_a}{1-\Gamma_a}, \;\; Z_1^b = Z_0 \frac{1+\Gamma_b}{1-\Gamma_b} \tag{6.19}$$

$$Z_3^a = 0, \;\; Z_3^b = jZ_3 \tan(k_{z3}\Delta). \tag{6.20}$$

Equations (6.17)-(6.20) are derived in Section 4.2.1. Here Z_0 and Z_3 are the wave impedances, which are determined by the angle of incidence, the intrinsic properties of the medium (subscript 0 is for free space and subscript 3 is for the spacer), and the polarization of the incident waves. The thickness of the MUT is represented by δ and Δ is the thickness of the spacer. Also, Γ_a and Γ_b represent the reflection coefficient with the metal plate directly against MUT and with the spacer between the MUT and the metal plate, respectively.

6.4.2 Measurement Set-Up

The same measurement statement described in Chapter 4.3.2 was used. To reiterate, measurements were made at Boeing on a bistatic reflection range of a commercial MagRAM from 5-18 GHz. The angle of incidence was 40° and δ = 57.16 mil. Plexiglas was used as a spacer with thickness $\Delta = 230.74$ mil. The incident field was transverse magnetic (TM) polarized. Although measurement of incidence angle, MUT thickness, spacer thickness, and reflection coefficient (magnitude and phase) propagate error into the extracted permittivity and permeability, this work only demonstrates interval analysis for use of **error propagated by measurement of angle**. Error due to MUT thickness, spacer thickness, and reflection coefficient can also be accurately analyzed with interval analysis. However, angle uncertainty is sufficient to demonstrate the basic principles of error analysis with intervals. Based on the instrument tolerances used in the measurements, the angle interval sensitivity is taken as

$$\theta = 40^\circ \pm .5^\circ = [39.5^\circ, 40.5^\circ]. \tag{6.21}$$

6.4.3 Comparison Interval Analysis to Monte Carlo Simulations

To test the usefulness of interval analysis as a method for error analysis, interval sensitivities are compared against standard deviations predicted by Monte Carlo simulations. Thorough analysis of the propagated error due to measurement of angle is presented.

Distribution of Data

As an initial assessment, it must be shown that the data collected during the experimental implementation of the layer-shift method is normally distributed. In previous chapters, ϵ_r and μ_r were assumed to be normally distributed. Assumption of a normal distribution for ϵ_r and μ_r is a fair assumption because the normal distribution is a very common distribution for natural phenomena. Normal distribution of the data is critical for the probability theory discussed in Section 6.3.2 to be valid.

To demonstrate that the extracted ϵ_r and μ_r are normally distributed a normal probability plot is created. The normal probability plot assesses the data distribution by creating a cumulative distribution plot of the data set. Then a line joining the first and third quartiles of a data set is superimposed on the cumulative distribution plot [52]. The first and third quartiles are the points that cut off the lower and upper 25% of the data respectively (i.e. - the 25% and 75% percentiles). If the data set is normally distributed, the plot will be linear; otherwise there will be curvature in the plot. Here the extracted ϵ_r and μ_r values extracted using layer-shift method discussed in Sections in 6.4.1 and 6.4.2 are the data sets which are being tested for normal distribution. The extracted ϵ_r and μ_r are in Figures 4.6 and 4.7, respectively.

Figures 6.4-6.5 are normal probability plots of the extracted ϵ_r and μ_r from using the layer-shift method from 5-18 GHz as described in Section 4.3.2. Observation of Figures 6.4-6.5 show that the extracted ϵ_r and μ_r data can be considered normally distributed. There is some slight curvature in normal probability plot of μ_r'. This curvature is due to the waviness in the extracted μ_r' values. Figure 4.7 shows that the extracted μ_r' data set experiences a slight downward trend from 5-16 GHz. This downward trend in the μ_r' data set then creates some waviness in the cumulative distribution plot. In contrast, ϵ_r', ϵ_r'', and μ_r' are relatively flat from 5-16 GHz, which then leads to a straighter cumulative distribution plot.

Initial Comparison of Interval Analysis and Monte Carlo Simulations

The mean, ξ, and the standard deviation, σ, of extracted ϵ_r and μ_r predicted by Monte Carlo simulations and interval analysis is compared. Table 6.1 shows the mean calculated with Monte Carlo simulations and interval analysis at several points in the frequency band.

Again, the midpoint of the interval is interpreted as the mean when using interval analysis. At 10 GHz, the mean for both real and imaginary parts of ϵ_r and μ_r are extremely close. However, there are great discrepancies at 5 GHz and 15 GHz. At 15 GHz, the Plexiglas spacer is approaching an integer multiple of a half-wavelength. Thus, equation (6.20) becomes large and the extraction of ϵ_r and μ_r suffers. This behavior at 15 GHz is detrimental to Monte Carlo simulations which is evidenced by the drastic change in the mean values of ϵ_r and μ_r. The Monte Carlo simulations also suffer at 5 GHz; at 5 GHz the edge diffractions on the edge of the sample make it difficult to accurately measure the reflection coefficients, and thus affect the extraction process. Other frequencies between 5-15 GHz will show similar results to the one found at 10 GHz because the extraction process is not subject to the Plexiglas thickness or edge diffraction issues. This is evidenced by the flatness in the plot of ϵ_r and μ_r versus frequency in Figures 4.6 and 4.7.

These type of physical phenomena which result in random error in the measurement process are difficult to quantify with Monte Carlo simulations. In these situations, Monte Carlo simulations produce so many extreme values that the entire normal distribution is shifted. In these cases, interval analysis is a great tool to implement. Observation of Table 6.1 shows that the mean predicted by error analysis is much more stable. The stability of the mean values allows for immediate assessment of the sensitivity of ϵ_r and μ_r.

Table 6.2 shows the standard deviations by Monte Carlo simulations and sensitivity intervals computed via interval analysis. At first glance, it appears that the interval analysis predictions are overestimated. However, one must remember that one standard deviation, σ, predicted by Monte Carlo simulations is valid for only 34.1% of the extractions [53]. Even so, the sensitivity intervals are still considerably larger than the 3σ tolerances predicted by the Monte Carlo simulations which represent nearly 100% of ϵ_r and μ_r extractions. It is emphasized that interval analysis gives absolute bounds for μ_r and ϵ_r. From this perspective, the interval analysis solutions provide a useful benefit in that the worst possible solution is explicitly stated. Nevertheless, the worst possible solutions are not the most probable bounds for μ_r and ϵ_r. Using refinement as explained in Section 6.3, tighter sensitivity intervals can be calculated.

Comparison of Refined Interval Analysis and Monte Carlo Simulations

The refinement process described in Section 6.3 was used to obtain closer intervals to the standard deviations for ϵ_r and μ_r found with Monte Carlo due to propagation of angle error. Tables 6.3 and 6.4 show the refined bounds for the real and imaginary parts of ϵ_r and μ_r. The column labeled n shows how many times the angle interval was subdivided. As n increases, the radius of the ϵ_r and μ_r intervals become smaller. For n=100, there is the greatest amount of correlation between the standard deviations predicted Monte Carlo and interval analysis. Table 6.5 show the standard deviations predicted by Monte Carlo simulations and the original and refined interval standard deviations. In addition, further refinement past n=100 does not provide further decrease in the width of the interval. Additionally, Tables 6.3 and 6.4 show a great amount of stability in the midpoint of the intervals. The stability of the midpoint of the intervals is very important to ensure accurate comparison between Monte Carlo simulations and other interval results.

Visualization of Error Analysis

Interval analysis also provides a clear method for determining error introduced over a frequency band or any parameter where a sweep is desired. Figures 6.6 and 6.7 shows the infimum, supremum, and extracted μ_r and ϵ_r vs. frequency for the layer-shift method. The figure shows that the layer-shift method provides accurate extractions of μ_r and ϵ_r until the Plexiglas spacer becomes an integer multiple of $\lambda/2$ around 17 GHz where Z_3 becomes large and the extraction cannot be performed. In this manner, interval analysis is particularly useful opposed to the Monte Carlo simulations because it is computationally lighter; for Monte Carlo simulations hundreds of thousands trials must be run for each frequency which is to be evaluated.

6.5 Conclusions

This chapter demonstrate use of interval analysis for error analysis in reflection-only material characterization techniques. Interval analysis is shown to be useful by implementing it in predicting the error introduced by incidence angle uncertainty into the layer-shift method. Error tolerances predicted with interval analysis are compared to error bounds predicted with Monte Carlo simulations. Excellent agreement between error bounds found with Monte Carlo simulations and refined interval analysis are found. Thus, an additional tool for performing error analysis for material characterization has been found. Future work includes performing multivariate error analysis with interval analysis.

Freq. (GHz)	Method	$\xi_{\mu_r'}$	$\xi_{\mu_r''}$	$\xi_{\epsilon_r'}$	$\xi_{\epsilon_r''}$
5	Monte Carlo	4.8197	-1.5683	9.5510	-0.3274
5	Interval Analysis	2.4534	-1.0872	10.3583	-0.3780
10	Monte Carlo	1.7135	-0.9394	10.6874	-1.5008
10	Interval Analysis	1.7157	- 0.9420	10.6944	- 1.5105
15	Monte Carlo	-1.3249	-0.1793	-7.0188	-6.2221
15	Interval Analysis	1.2173	- 0.9263	10.6892	- 1.1006

Table 6.1: Mean ϵ_r and μ_r predicted by Monte Carlo simulations and interval analysis at 5,10, and 15 GHz

Frequency (GHz)	Method	$\sigma_{\mu_r'}$	$\sigma_{\mu_r''}$	$\sigma_{\epsilon_r'}$	$\sigma_{\epsilon_r''}$
10	Monte Carlo	0.0068	0.0113	0.0892	0.0562
10	Interval Analysis	0.1556	0.1556	0.4983	0.4983

Table 6.2: Standard deviation of ϵ_r and μ_r predicted by Monte Carlo simulations and interval analysis at 10 GHz

n	$\xi_{\mu'_r}$	$\sigma_{\mu'_r}$	$\xi_{\mu''_r}$	$\sigma_{\mu''_r}$
2	1.7138	0.0778	-0.9398	0.0800
5	1.7135	0.0345	-0.9394	0.0381
10	1.7135	0.0206	-0.9394	0.0246
20	1.7135	0.0137	-0.9394	0.0179
50	1.7135	0.0096	0.9394	0.0140
100	1.7135	0.0083	-0.9394	0.0127

Table 6.3: Standard deviation of μ_r predicted by refined interval analysis at 10 GHz

n	$\xi_{\epsilon'_r}$	$\sigma_{\epsilon'_r}$	$\xi_{\epsilon''_r}$	$\sigma_{\epsilon''_r}$
2	10.6102	0.2865	-0.8675	0.2701
5	10.6083	0.1665	-0.8654	0.1401
10	10.6076	0.1276	-0.8649	0.0979
20	10.6072	0.1083	-0.8647	0.0770
50	10.6070	0.0929	-0.8645	0.0645
100	10.6070	0.0083	-0.8645	0.0604

Table 6.4: Standard deviation of ϵ_r predicted by refined interval analysis at 10 GHz

Method	$\sigma_{\epsilon_r'}$	$\sigma_{\epsilon_r''}$	$\sigma_{\mu_r'}$	$\sigma_{\mu_r''}$
Monte Carlo	0.2274	0.1091	0.0329	0.0226
Interval Analysis	2.6321	2.6321	1.0224	1.0224
Interval Analysis (Refined)	0.2194	0.0953	0.0333	0.0255

Table 6.5: Standard deviation of ϵ_r and μ_r predicted by Monte Carlo simulations and Interval Analysis at 10 GHz

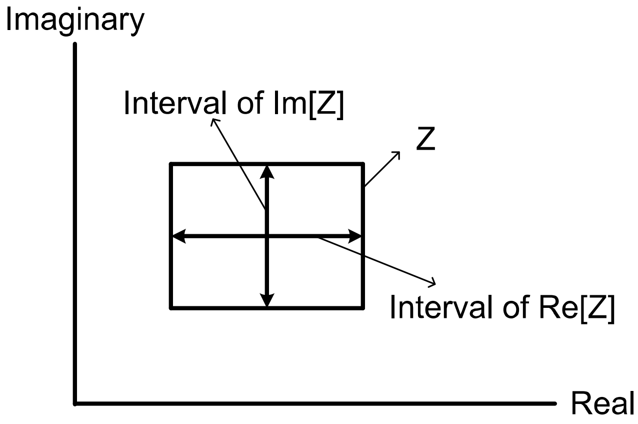

Figure 6.1: Rectangular interval representation in the complex plane

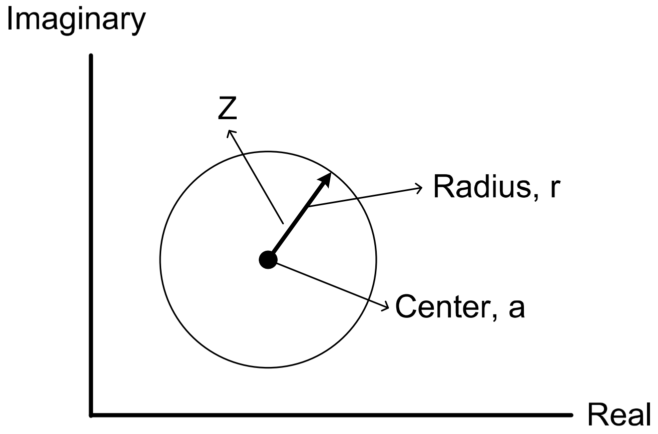

Figure 6.2: Circular interval representation in the complex plane

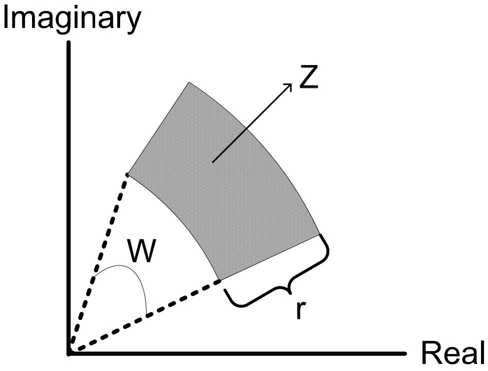

Figure 6.3: Sector interval representation in the complex plane

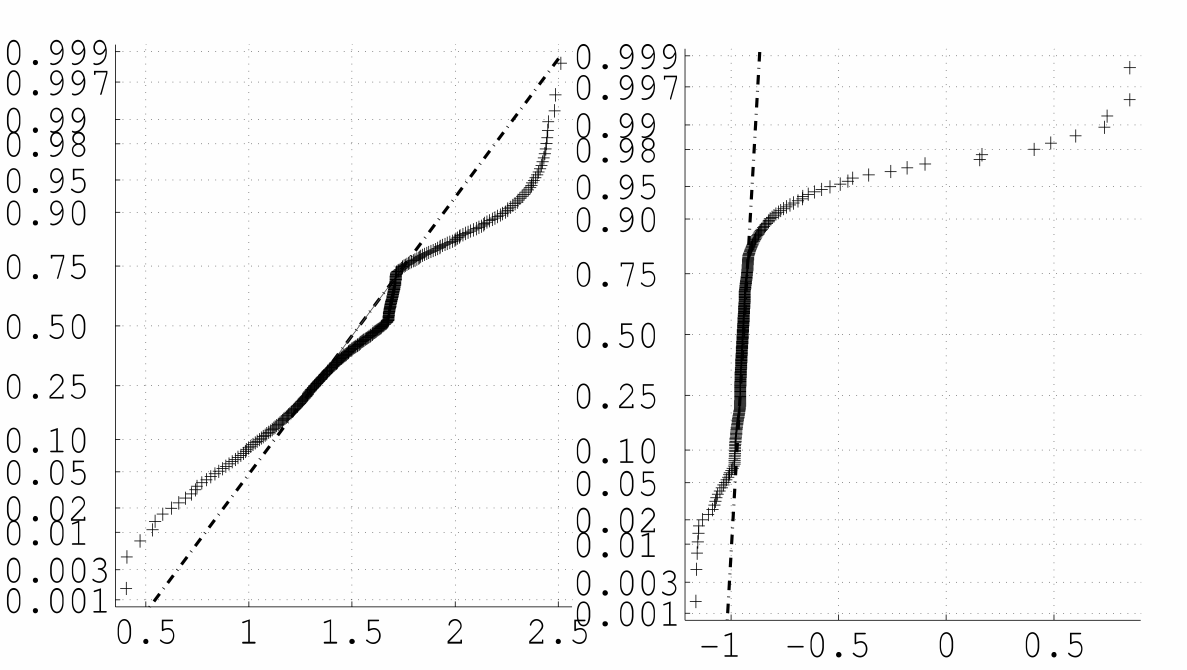

Figure 6.4: Normal probability plots of extracted ϵ_r from the layer-shift method

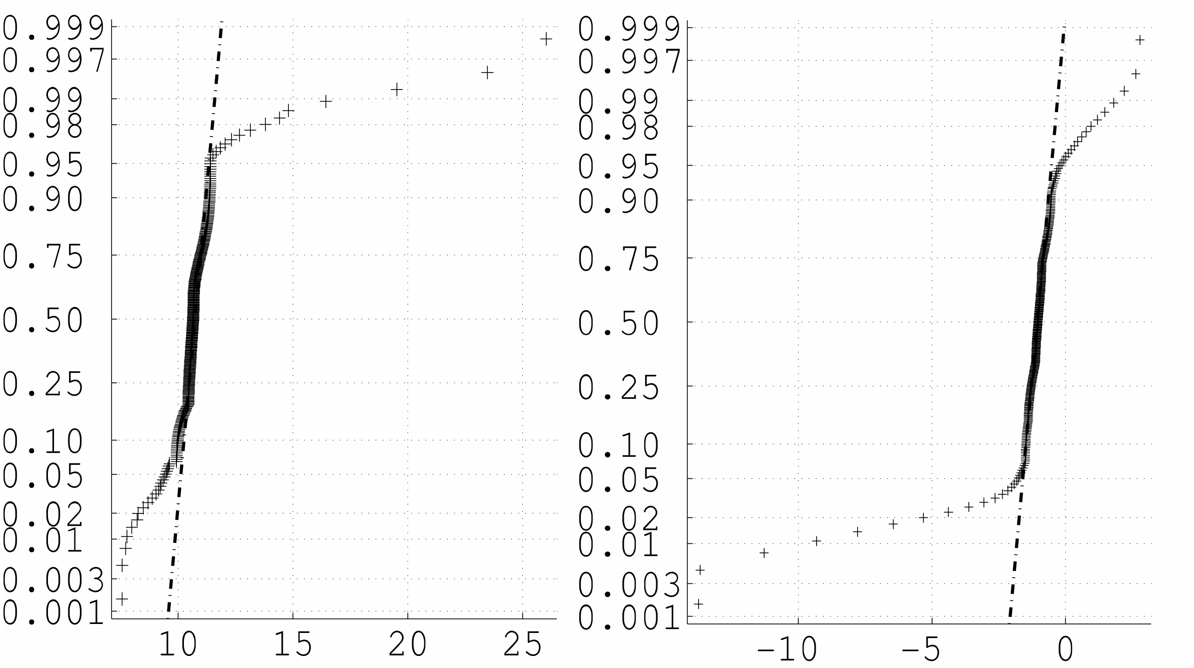

Figure 6.5: Normal probability plots of extracted μ_r from the layer-shift method

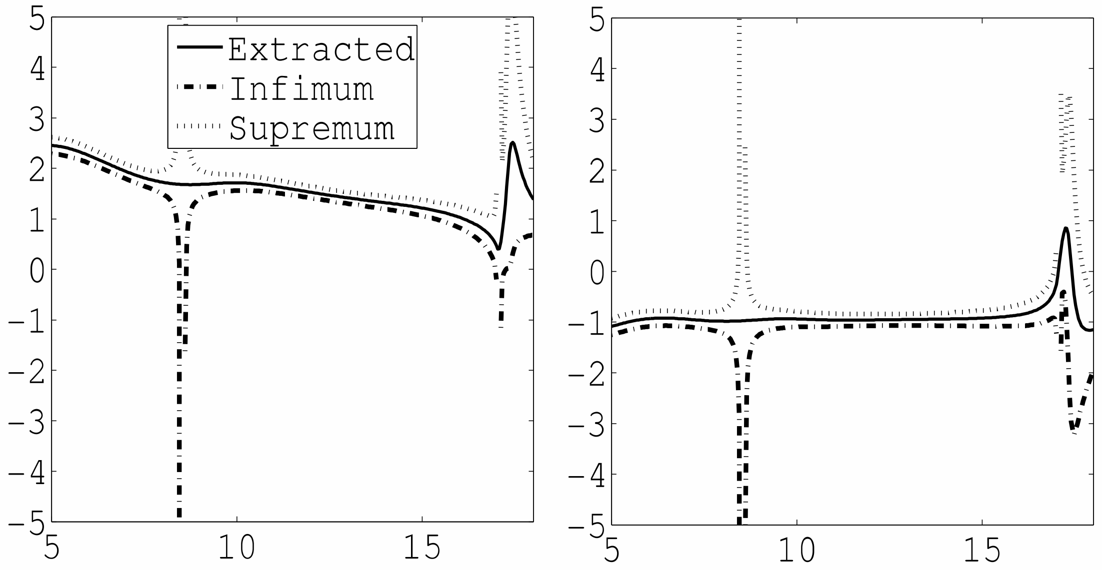

Figure 6.6: Layer-shift extraction of vs. frequency

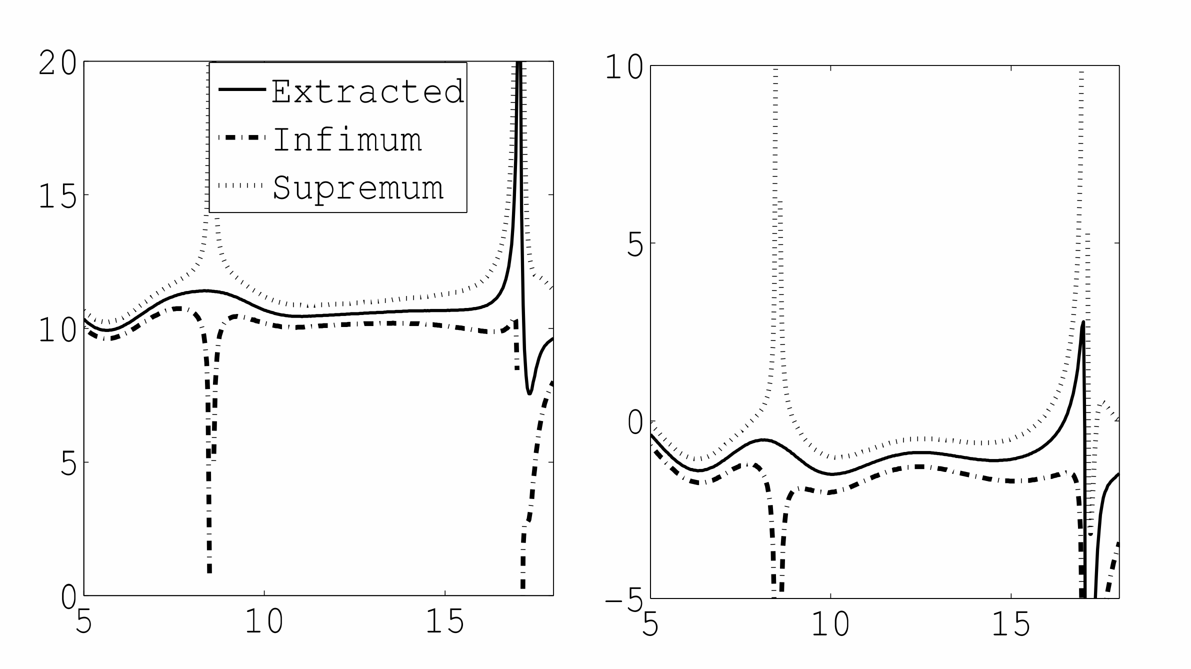

Figure 6.7: Layer-shift extraction of ϵ_r vs. frequency

Chapter 7

Effects of Curved Wavefronts on Free-Space Material Characterization Techniques

7.1 Introduction

Up to this point, there has only been analysis of random error in reflection-only material characterization methods. This chapter performs an error analysis on a source of systematic error in free-space reflection-only material characterization methods.

In all free space material characterization techniques, a plane wave is assumed to illuminate the MUT. A plane wave is defined as a constant-frequency wave whose wavefronts (surfaces of constant phase) are infinite parallel planes of constant amplitude normal to the phase velocity vector.

Since in practice a true plane wave cannot be produced, the assumption of plane wave incidence used to derive extraction formulas introduces a source of error into extraction schemes. To examine the extent of this error, the canonical problem of a line source above a material slab is examined. By varying the height of the line source, the effect of wavefront curvature on the accuracy of the extracted material properties can be explored.

The scattered electric field produced by both electric and magnetic line sources above an air-backed and conductor-backed MUT are computed via the Sommerfeld integral approach, and used to determine a reflection coefficient for the case of a nonplanar incident-field wavefront by maintaining Snell's law of reflection. This data is then used in the expressions for μ_r and ϵ_r derived using a planar incident field, and the error computed. The effect of wavefront curvature is explored for various combinations of aspect angle and material parameters to determine the conditions under which the effect of curvature is least pronounced.

7.2 Reflection Coefficients Due to an Electric Line Source

7.2.1 Field of An Electric Line Source Above a Layered Medium

In order to find the reflection coefficient due to a curved wavefront, the scattered electric field in region 3 (shown in Figure 7.3) must first be found. The infinite electric line current supports the fields $\vec{E}$ and $\vec{H}$. The approach taken to find $\vec{E}$ and $\vec{H}$ in region 3 is to solve the wave equation, $\nabla^2\vec{A}+k^2\vec{A}=0$, for $\vec{A}$ in each source-free region depicted in figure 7.3, where $k^2=\omega^2\mu\epsilon$.

Before solving the wave equation for $\vec{A}$, a few simplifications can be made. First due to the invariance of the geometry in figure 7.3 in the x-direction, $\vec{A}$ can simply be written as $\hat{x}A_x(y,z)$. The Lorentz condition ($\nabla\cdot\vec{A}+\jmath\omega\mu\epsilon\phi=0$) then shows that the scalar potential is zero because $\nabla\cdot\vec{A}=\frac{\partial}{\partial x}A_x(y,z)=0$. Therefore from $\vec{E}=-\jmath\omega\vec{A}-\nabla\phi$, there is only an x-component to the electric field and $E_x=-\jmath\omega A_x$. In addition, the magnetic field is expressed as $\vec{H}=\frac{1}{\mu}\nabla\times\vec{A}=\frac{1}{\mu}[\hat{y}\frac{\partial A_x}{\partial z}-\hat{z}\frac{\partial A_x}{\partial y}]$, and so $H_y=\frac{1}{\mu}\frac{\partial A_x}{\partial z}$ and $H_z=-\frac{1}{\mu}\frac{\partial A_x}{\partial y}$.

The method chosen to solve the wave equation is to take the Fourier transform of A_x in each region; the Fourier transform is performed on the y-variable to reduce the partial differential equations to ordinary differential equations. The Fourier transform pair is defined as

$$\tilde{A_x}(k_y,z) = \int_{-\infty}^{\infty} A_x(y,z)\,e^{-\jmath k_y y}\,dy \tag{7.1}$$

$$A_x(y,z) = \frac{1}{2\Pi}\int_{-\infty}^{\infty} \tilde{A_x}(k_y,z)\,e^{\jmath k_y y}\,dk_y. \tag{7.2}$$

Plugging the inverse Fourier transform into the wave equation for A_x, one will find

$$\frac{1}{2\pi}\int_{-\infty}^{\infty}\left(\frac{\partial^2}{\partial z^2}+k^2-k_y^2\right)\tilde{A_x}\left(k_y,z\right)e^{\jmath k_y y}dk_y=0. \tag{7.3}$$

Since the inverse Fourier transform is zero, $\left\{\frac{\partial^2}{\partial z^2}+k^2-k_y^2\right\}A_x=0$. Therefore, there are two ordinary differential equations that must be solved.

The equation $\left(\frac{\partial^2}{\partial z^2}+p^2\right)\tilde{A_x}\left(k_y,z\right)=0$ has to be solved in regions 0, 2, and 3. The equation $\left(\frac{\partial^2}{\partial z^2}+q^2\right)\tilde{A_x}\left(k_y,z\right)=0$ must be solved in region 1. Here $p=\pm\sqrt{k_0^2-k_y^2}$ and $q=\pm\sqrt{k^2-k_y^2}$, with the sign chosen such that waves decay as they propagate.

The solutions to the ordinary differential equations can be assumed to be $\tilde{A_x}\left(k_y,z\right)\backsim e^{\pm jpz}$ in regions 0, 2, and 3 and $\tilde{A_x}\left(k_y,z\right)\backsim e^{\pm\jmath qz}$ in region 1. Thus, the solutions in each region are:

$$\tilde{A_x} = C_1e^{-jpz}, \text{ in region 3} \tag{7.4}$$

$$\tilde{A_x} = C_2e^{jpz}+C_3e^{-jpz}, \text{ in region 2} \tag{7.5}$$

$$\tilde{A_x} = C_4\sin(qz)+C_5\cos(qz), \text{ in region 1.} \tag{7.6}$$

The fields are then found from the potentials using

$$H_y=\frac{1}{2\pi}\int_{-\infty}^{\infty}\frac{1}{\mu}\frac{\partial\tilde{A_x}(k_y,z)}{\partial z}e^{\jmath k_y y}\partial k_y \tag{7.7}$$

$$H_z=\frac{-1}{2\pi}\int_{-\infty}^{\infty}\frac{1}{\mu}\jmath k_y\tilde{A_x}(k_y,z)e^{\jmath k_y y}dk_y \tag{7.8}$$

$$E_x=\frac{1}{2\pi}\int_{-\infty}^{\infty}-\jmath\omega\tilde{A_x}(k_y,z)e^{\jmath k_y y}dk_y. \tag{7.9}$$

In order to find the constants C_1, C_2, C_3, C_4, and C_5, the boundary conditions on the tangential electric and magnetic field must be enforced $\left(\hat{n}\times\left(\vec{E}_3-\vec{E}_2\right)=-\vec{M}_s,\ \hat{n}\times\left(\vec{H}_3-\vec{H}_2\right)=\vec{J}_s\right)$ at $z=t$ and $z=h$.

At $z = h$, the is no magnetic current, so E_x and A_x are continuous. Thus, $E_{x2} = E_{x3}$, $\tilde{A}_{x2} = \tilde{A}_{x3}$. Hence, from equating equation (7.4) to equation (7.5), $C_3 = C_1 - C_2 e^{\jmath 2ph}$.

At $z = h$, H_y is discontinuous by the electric line source. Therefore, the equation $\left(\frac{\partial^2}{\partial z^2} + p^2\right)\tilde{A_x}\left(k_y, z\right) = 0$ at $z = h$ becomes

$$-\frac{\partial \tilde{A}_{x3}}{\partial z} + \frac{\partial \tilde{A}_{x2}}{\partial z} = \mu_0 I. \tag{7.10}$$

Substituting the solutions of $\tilde{A}_x$ in equations (7.4) - (7.5) in equation (7.10), equation (7.10) becomes

$$\jmath p C_1 e^{-\jmath ph} + \jmath p C_2 e^{\jmath ph} - \jmath p C_3 e^{-\jmath ph} = \mu_0 I. \tag{7.11}$$

Substituting $C_3 = C_1 - C_2 e^{\jmath 2ph}$ into equation (7.11) then gives

$$C_2 = \mu_0 I \frac{e^{-\jmath ph}}{2\jmath h} = F, \tag{7.12}$$

where F is an alternate variable name for C_2.

At the $z = t$ interface, E_x and H_y are continuous. The tangential electric fields, E_x, and magnetic fields, H_y, are then

$$C_2 e^{\jmath pt} + C_3 e^{\jmath pt} = C_4 \sin(qt) + C_5 \cos(qt) \tag{7.13}$$

$$\frac{\jmath p}{\mu_0} C_2 e^{\jmath pt} - \frac{\jmath p}{\mu_0} C_3 e^{\jmath pt} = \frac{q}{\mu} C_4 \sin(qt) - \frac{q}{\mu} C_5 \cos(qt). \tag{7.14}$$

The boundary equations at $z = h$ and $z = t$ give two equations and three unknowns. The boundary conditions at $z = 0$ give a condition for C_4 and C_5, i.e. - $C_5 = WC_4$ (where W is yet to be determined). With $C_5 = WC_4$,

$$Fe^{\jmath pt} + C_3 e^{\jmath pt} = C_4\left[\sin(qt) + W\cos(qt)\right] \tag{7.15}$$

$$F\jmath p\mu_r e^{\jmath pt} - \jmath p\mu_r e^{\jmath pt} = C_4\left[q\cos(qt) - Wq\sin(qt)\right]. \tag{7.16}$$

Equations (**??**)-(7.16) are then solved for C_3, which yields

$$C_3 = \frac{\mu_0}{2\jmath p} R e^{-\jmath p(h-2t)}, \tag{7.17}$$

where

$$R = \frac{\mu_r \jmath p\sin(qt) - q\cos(qt) + W\left[q\sin(qt) - \mu_r \jmath p\cos(qt)\right]}{\mu_r \jmath p\sin(qt) + q\cos(qt) - W\left[q\sin(qt) + \mu_r \jmath p\cos(qt)\right]}. \tag{7.18}$$

Equation (7.17) has a singularity at $p = 0$. To remove this singularity, $R+1$ is examined. $R+1$ yields

$$R+1 = \frac{2\mu_r \jmath p\sin(qt) + 2\mu_r W\jmath q\cos(qt)}{\mu_r \jmath p\sin(qt) + q\cos(qt) - W\left[q\sin(qt) + \mu_r \jmath p\cos(qt)\right]} \sim p. \tag{7.19}$$

This property will be used later.

Using equation (7.17) and $C_3 = C_1 - C_2 e^{\jmath 2ph}$, $\tilde{A}_x$ in both regions 2 and region 3 can be written as

$$\tilde{A}_x = \frac{\mu_0 I}{2\jmath p} e^{-\jmath p|z-h|} + \frac{\mu_0 I}{2\jmath p} R e^{-2\jmath p(h-t)} e^{-2\jmath p(z-h)}. \tag{7.20}$$

To find A_x, the inverse Fourier transform of equation (7.20) must be taken. Taking the inverse Fourier transform of equation (7.20), $\tilde{A}_x$ is calculated from

$$A_x = \frac{1}{2\pi}\int_{-\infty}^{\infty} \frac{\mu_0 I}{2\jmath p} e^{-\jmath p|z-h|} e^{\jmath k_y y} + \frac{1}{2\pi}\int_{-\infty}^{\infty} \frac{\mu_0 I}{2\jmath p} \bar{R} e^{-2\jmath p(z-h)}, \tag{7.21}$$

where $\bar{R} = e^{-2\jmath p(h-t)} R$. The first term in equation (7.21) is equal to a zeroth-order Hankel function of the second kind [20]. Therefore, equation (7.21) is equal to

$$A_x = \frac{\mu_0 I}{4\jmath} H_0^{(2)}\left(k_0 r\right) + \frac{1}{2\pi}\int_{-\infty}^{\infty} \frac{\mu_0 I}{2\jmath p}\bar{R} e^{-2\jmath p(z-h)}, \tag{7.22}$$

where $r = \sqrt{(z-h)^2 + y^2}$.

The first term in equation (7.22) represents the principal reflected potential produced by the line source at $z = h$ and $y = 0$. The image of the principal potential produced by the line source is $-\frac{\mu_0 I}{4\jmath} H_0^{(2)}\left(k_0 \bar{r}\right)$, where $\bar{r} = \sqrt{\bar{h}^2 + y^2}$. The second term in equation (7.22) is the correction term in the scattered potential. The correction factor still contains the singularity at $p = 0$. To remove the singularity at $p = 0$, make the $\bar{R} = e^{-2\jmath p(h-t)} R$ substitution into equation (7.22), and again examine $R + 1$. Adding 1 to R removes the singularity at $p = 0$. The correction factor then becomes

$$A_x^c = \frac{\mu_0 I}{2\pi}\int_{-\infty}^{\infty} \frac{\mu_r\left(\sin(qt) + W\cos(qt)\right)e^{-\jmath p\bar{h}}}{\mu_r \jmath p\sin(qt) + q\cos(qt) - W\left[q\sin(qt) - \mu_r \jmath p\cos(qt)\right]} e^{\jmath k_y y}\, dk_y, \tag{7.23}$$

where $\bar{h} = z + h - 2t$.

For the special case of a conductor-backed slab, $E_x = 0$ at $z = 0$ because the tangential component of the electric field equals zero at a PEC. Thus, $\tilde{A}_x = 0$ since $E_x = -\jmath\omega A_x$. Furthermore, $C_5 = 0$ because $C_4\sin(qt) + C_5\cos(qt) = 0$ at $z = 0$. Ultimately, $W = 0$ and A_x^c becomes

$$A_x^c = \frac{\mu_0 I}{2\pi}\int_{-\infty}^{\infty} \frac{\mu_r \sin(qt)e^{-\jmath p\bar{h}}}{\mu_r \jmath p\sin(qt) + q\cos(qt)} e^{\jmath k_y y}\, dk_y. \tag{7.24}$$

As noted in Section 7.2, the scattered potential due to the electric line source is

$$A_x = A_x^s + A_x^c. \tag{7.25}$$

The scattered electric field due to the electric line source is computed with $E_x = -\jmath\omega A_x$, where

$$E_x^S = E_x^R + E_x^C \tag{7.26}$$

with

$$E_x^R = \frac{\omega\mu_0 I}{4} H_0^{(2)}(k_0 \bar{r}) \tag{7.27}$$

$$E_x^C = \frac{\omega\mu_0 I}{4\pi} \int_{-\infty}^{\infty} \frac{2\jmath\mu_r \sin(qt) e^{-\jmath p\bar{h}}}{\mu_r \jmath p \sin(qt) + q\cos(qt)} e^{\jmath k_y y} dk_y, \tag{7.28}$$

where $\bar{r} = \sqrt{(z - [2t - h])^2 + y^2}$.

Equation (7.28) can be rewritten in a more useful form. Expanding $e^{\jmath k_y y}$ into $\cos(k_y y) + \jmath \sin(k_y y)$ with Euler's identity, dividing numerator and denominator with $\sin(qt)$, and realizing that q and p are even in k_y gives

$$E_x^c = \frac{-\omega\mu_0 I}{\pi} \int_0^{\infty} \frac{\jmath e^{-\jmath p\bar{h}}}{\jmath p + q\frac{\mu_0}{\mu}\cot(qt)} \cos(k_y y) dk_y. \tag{7.29}$$

Next, using $\cot(x) = \jmath\frac{1+e^{-2\jmath x}}{1-e^{-2\jmath x}}$, the final form of the correction factor of the scattered electric field becomes

$$E_x^c = \frac{-\omega\mu_0 I}{\pi} \int_0^{\infty} \frac{e^{-\jmath p\bar{h}}}{p + q\frac{\mu_0}{\mu}\frac{1+e^{-2\jmath qt}}{1-e^{-2\jmath qt}}} \cos(k_y y) dk_y. \tag{7.30}$$

The final scattered electric field is thus:

$$E_x^S = \frac{\omega\mu_0 I}{4} H_0^{(2)}(k_0 \bar{r}) + \frac{-\omega\mu_0 I}{\pi} \int_0^{\infty} \frac{e^{-\jmath p\bar{h}}}{p + q\frac{\mu_0}{\mu}\frac{1+e^{-2\jmath qt}}{1-e^{-2\jmath qt}}} \cos(k_y y) dk_y. \tag{7.31}$$

7.2.2 Reflection Coefficient to Emulate Plane Wave Reflection

Geometry for Simulations

In order to find an appropriate reflection coefficient, the free-space measurement setup that would be used in an actual measurement scenario is emulated. The free-space measurement setup is diagrammed in Figure x.

Considering the setup in Figure 7.4, the y, $\bar{h}$, and $\bar{r}$ in equation (7.33) can be rewritten in terms of an equivalent incident angle θ_i. With r as the distance from the front face of the slab, $y = 2r\sin\theta_i$. Similarly, $\bar{h} = 2r\cos\theta_i$. Lastly,

$$\bar{r} = \sqrt{4(h-t)^2 + y^2} = 2\sqrt{r^2\cos^2\theta_i + r^2\sin^2\theta_i} = 2r. \tag{7.32}$$

As a result, equation (7.33) can be rewritten in terms of θ_i as

$$E_x^s = \frac{\omega\mu_0 I}{4} H_0^{(2)}(2k_0 r) + \frac{-\omega\mu_0 I}{\pi}\int_0^\infty \frac{e^{-2jpr\cos\theta_i}}{p + q\frac{\mu_0}{\mu}\frac{1+e^{-2jqt}}{1-e^{-2jqt}}}\cos(2k_y r\sin\theta_i)dk_y. \tag{7.33}$$

Reflection Coefficient for the Electric Line Source

In order to find the global reflection coefficient, a calibration similar to a real laboratory measurement process is used. The calibration process works by placing a PEC plate at the same location as the front layer of the material stack at $z = t$. Since the reflection coefficient for a PEC plate is -1, the calibrated reflection coefficient is

$$\Gamma = -\frac{E_x^s}{E_x^p}, \tag{7.34}$$

where E_x^p is the scattered field due to the PEC plate. To find the scattered field off of the PEC plate by the electric line source, image theory is used. Figure 7.5 shows the diagram of the image theory setup. The calculated scatted field is

$$E_x^p = \frac{\omega\mu_0 I}{4} H_0^{(2)}(k_0 d), \tag{7.35}$$

where d is the distance from the image line source to the observation point in Figure 7.5. The very important result for the calibrated reflection coefficient is therefore

$$\Gamma = -1 + \frac{4}{\pi}\frac{1}{H_0^{(2)}(2k_0 d)}\int_0^\infty \frac{e^{-2\jmath pr\cos\theta_i}}{p + q\frac{\mu_0}{\mu}\frac{1+e^{-2\jmath qt}}{1-e^{-2\jmath qt}}}\cos(2k_y r\sin\theta_i)\,dk_y. \tag{7.36}$$

7.3 Reflection Coefficient for a Magnetic Line Source

The process for finding the reflection coefficient due to a magnetic line source follows the same steps for finding the reflection coefficient for the electric line source described in Section 7.2. The goal is to find the scattered electric and magnetic fields, $\vec{E}$ and $\vec{H}$, supported a magnetic line source. To find $\vec{E}$ and $\vec{H}$, the wave equation is solved for the magnetic vector potential, $\vec{F}$, in the three source-free regions diagramed in Figure 7.3. Additionally, boundary conditions are applied at $z = t$ and $z = h$ to find the amplitude constants generated from solution of the wave equation. The same Fourier transform pair in equations (7.1)-(7.2) are used to solve for the wave equation in terms of $\vec{F}$.

Like for the solution for the scattered electric field due to the electric line source, the scattered *magnetic* field due to the magnetic line source is composed of two parts - the reflected field and a correction factor. The total scattered magnetic field is thus written as

$$H_x^s = H_x^R + H_x^C. \tag{7.37}$$

In equation (7.37), H_x^R is the reflected portion of the scattered magnetic field and is found to be

$$H_x^R = \frac{\omega\epsilon_0 Im}{4}H_0^{(2)}(k_0\bar{r}), \tag{7.38}$$

while H_x^C is the correction factor of the scattered magnetic field which is

$$H_x^C = \frac{-\omega\epsilon_0 Im}{\pi}\int_0^\infty \frac{e^{-2jpr\cos\theta_i}}{p+q\frac{\epsilon_0}{\epsilon}\frac{1+e^{-2jqt}}{1-e^{-2jqt}}}\cos(k_y y)dk_y. \tag{7.39}$$

At this point, it is necessary to find the scattered electric field due to the magnetic line source since this is the field is what is measured experimentally. The electric field is computed from the magnetic field by using

$$E_y = \frac{1}{j\omega\epsilon}\frac{\partial H_x}{\partial z}. \tag{7.40}$$

Using equation (7.40), equations (7.38)-(7.39) are used to find the scattered electric field which is

$$E_x^R = \frac{k_0 Im}{j4}\frac{z+h-2t}{\bar{r}}H_1^{(2)}(k_0\bar{r}) \tag{7.41}$$

$$E_x^c = \frac{Im}{\pi}\int_0^\infty \frac{pe^{-jp(z+h-2t)}}{p+q\frac{\epsilon_0}{\epsilon}\frac{1+e^{-2jqt}}{1-e^{-2jqt}}}\cos(k_y y)dk_y. \tag{7.42}$$

Once again using a calibration process similar to that used in an actual laboratory setting and employing image theory the reflection coefficient for the magnetic line source is found to be

$$\Gamma_m = 1+\frac{4j}{\pi}\frac{1}{k_0\cos\theta_i H_1^{(2)}(k_0\bar{r})}\int_0^\infty \frac{e^{-2jpr\cos\theta_i}}{p+q\frac{\epsilon_0}{\epsilon}\frac{1+e^{-2jqt}}{1-e^{-2jqt}}}\cos(2k_y r\sin\theta_i)dk_y. \tag{7.43}$$

7.4 Wave Curvature Impact on the Two-Thickness Method

The two-thickness method is a method for characterizing conductor-backed media. The two-thickness method is utilized by measuring the reflection coefficient for two different MUT thicknesses. The extraction equations and further information about the two-thickness method is found in Section 4.3.3. Additionally, a diagram of the two-thickness method is found in Figure 4.11. For the analysis in this chapter, a hypothetical implementation of the two-thickness method is created. To see the impact of wave curvature on the the two-thickness method, the reflection coefficients calculated with both the line sources and plane waves are compared. Comparison of the reflection coefficients is a good starting point because if there is little change between the reflection coefficients computed with the line sources and plane waves, then there will most likely be little difference in the extractions of ϵ_r and μ_r. The reflection coefficients are then compared under two different scenarios which include:

1. Variable line source distance to the MUT (incidence angle and MUT thickness held constant)
2. Variable MUT thickness (incident angle and distance to MUT held constant).

Both scenarios are tested on TE and TM polarized fields incident on Plexiglas and a 35% MagRAM described in Chapter 4. In all scenarios, the the second MUT thickness is always **twice** the thickness of the initial MUT thickness; this is done so the extraction equations are in closed form. All measurement setup parameters are presented in each scenario.

7.4.1 Scenario 1: Variation of Line Source Distance to the MUT

In a real laboratory environment, a true plane wave is not physically realizable since a wave would have to propagate to infinity to be a true plane wave. However, waves which can be approximated as plane waves are achievable when the distance between the source and the MUT is great enough. Thus, the distance from the source to the MUT in the laboratory environment is an important factor in the plane wave assumption in free-space material characterization models.

To test the effect of the distance between the source and the MUT, the reflection coefficients due to the electric and magnetic line sources derived in Section 7.2 are computed and used in the two-thickness extraction scheme as if they were calculated with the plane wave assumption. The angle of incidence and the MUT thickness are held constant. The reflection coefficients are calculated for the line source placed at various distances from the MUT. The angle of incidence is set to $\theta = 40^\circ$ and the MUT thicknesses are set to 40 mil and 80 mil. Analysis is conducted at 3 GHz. The reflection coefficient is defined as $\Gamma = \Gamma' + \jmath\Gamma''$.

Tables 7.2 and 7.4 show the real and imaginary parts of the reflection coefficients calculated by varying the distance of the electric line source to the MUT. Here Γ_1 and Γ_2 are the reflection coefficients for when the MUT is 40 mil thick and 80 mil thick respectively. Also, h is the distance from the electric line source to the MUT in meters as shown in Figure 7.4. The reflection coefficient is then calculated for $h = 2^n$ for $n = 1,2,3\ldots$.

Observations of Tables 7.2, 7.4, 7.6 and 7.8 show for each increase in h there is little to no change in the reflection coefficients for both polarizations and both materials. Additionally, there is very little difference between the reflection coefficients calculated with a plane assumption, shown in Tables 7.1, 7.3, 7.5, and 7.7 and the reflection coefficients calculated with the electric and magnetic line sources. Since there is very little difference in the reflection coefficients calculated with the plane wave and line sources, there is little impact on the extracted ϵ_r and μ_r values.

Analysis of this scenario may show deceiving results. The MUT thicknesses in this scenario are very thin. Although these thicknesses are not uncommon in shielding or electromagnetic shielding control applications, the wavefronts do not cycle through enough phase for the presence of the MUT to be very significant. Therefore, analysis of scenario 2 where the MUT thicknesses are increased is necessary to show if a MUT with a greater thickness will have a greater affect on the calculation of the reflection coefficients using the line sources.

7.4.2 Variable MUT thickness

In this scenario, the MUT thickness are varied from 120 mil to 400 mil in 40 mil increments. The incidence angle is 40°. Also, h is set to 1 m and the operating frequency is set to 3 GHz.

This value of h is chosen because most laboratory setups will be able to have greater distance between the source antennas and the MUT. Thus, this scenario is a worst case scenario of sorts and better results can be assumed in real laboratory environments.

Tables 7.9, 7.11, 7.13, 7.15 show the reflection coefficients calculated with the plane wave assumption for both TE and TM polarizations for both Plexiglas and the MagRAM. Tables 7.10, 7.12, 7.14, 7.16 show the reflection coefficients calculated with the electric and magnetic line sources. Again, there is great agreement between the reflection coefficients calculated with the plane wave assumption and the line sources. There is the least amount of agreement between the reflection coefficients calculated with the TM polarized plane wave and the magnetic line source for the MagRAM sample. Tables 7.17 and 7.18 show the extracted ϵ_r and μ_r values with this case. Observation of the percent errors noted in these tables shows that there is very little impact on the extraction of ϵ_r and μ_r.

7.5 Conclusions

The impact of wave curvature on free-space material characterization methods has been investigated. The plane wave assumption in free-space material characterization methods can be thought of as a type of systematic error in all free-space methods because a true plane wave is not physically realizable in a laboratory environment.

To test the impact of wave curvature, the Fresnel reflection coefficients for TE and TM polarized waves are replaced with reflection coefficients calculated with electric and magnetic line sources in the two-thickness extraction algorithm. Results showed very little impact on the reflection coefficients or extracted ϵ_r and μ_r values for the line source distance of 1 m. As many labaratory setups should be able to have greater distance between the source antenna and the MUT, the impact on wave curvature is not expected to be great in many free-space material characterization measurements.

MUT Thickness	Γ'	Γ''
40 mil	-0.995	0.097
80 mil	-0.980	0.196

Table 7.1: Reflection coefficients calculated with a TM polarized plane wave (Plexiglas)

Line Source Distance (meters)	Γ'_1	Γ''_1	Γ'_2	Γ''_2
1	-.994	9.79×10^{-2}	-.979	.196
2	-.994	9.79×10^{-2}	-.980	.196
4	-.995	9.79×10^{-2}	-.980	.196
8	-.995	9.79×10^{-2}	-.980	.196
16	-.992	$9.79 \times 10^{-}2$	-.980	.196

Table 7.2: Reflection coefficients calculated with a magnetic line source at variable distances from the MUT (Plexiglas)

MUT Thickness	Γ'	Γ''
40 mil	-0.8238	0.2298
80 mil	-0.5968	0.3776

Table 7.3: Reflection coefficients calculated with a TM polarized plane wave (35% MagRAM)

Line Source Distance (meters)	Γ'_1	Γ''_1	Γ'_2	Γ''_2
1	-0.824	0.230	-0.597	0.378
2	-0.824	0.230	-0.596	0.378
4	-0.823	0.230	-0.596	0.377
8	-0.823	0.229	-0.596	0.377

Table 7.4: Reflection coefficients calculated with a magnetic line source at variable distances from the MUT (35% MagRAM)

MUT Thickness	Γ'	Γ''
40 mil	-0.990	0.140
80 mil	-0.960	0.279

Table 7.5: Reflection coefficients calculated with a TE polarized plane wave (Plexiglas)

Line Source Distance (meters)	Γ_1'	Γ_1''	Γ_2'	Γ_2''
1	-0.992	0.139	-0.961	0.280
2	-0.990	0.140	-0.960	0.279
4	-0.990	0.140	-0.960	0.279
8	-0.990	0.140	-0.960	0.279

Table 7.6: Reflection coefficients calculated with an electric line source at variable distances from the MUT (Plexiglas)

MUT Thickness	Γ'	Γ''
40 mil	-0.899	0.148
80 mil	-0.762	0.268

Table 7.7: Reflection coefficients calculated with a TE polarized plane wave (35% MagRAM)

Line Source Distance (meters)	Γ'_1	Γ''_1	Γ'_2	Γ''_2
1	-0.899	0.148	-0.761	0.267
2	-0.899	0.148	-0.762	0.267
4	-0.899	0.148	-0.762	0.267

Table 7.8: Reflection coefficients calculated with an electric line source at variable distances from the MUT (35% MagRAM)

MUT Thickness (mil)	Γ'	Γ''
120	-0.9554	0.2952
160	-0.9186	0.3950
200	-0.8685	0.4954
240	-0.8027	0.5960
280	-0.7181	0.6953
320	-0.6110	0.7908
360	-0.4769	0.8778
400	-0.3111	0.9488

Table 7.9: Reflection coefficients calculated with a TM plane wave (Plexiglas)

MUT Thickness (mil)	Γ'	Γ''
120	-0.954	0.295
160	-0.917	0.394
200	-0.867	0.495
240	-0.801	0.595
280	-0.716	0.694
320	-0.608	0.789
360	-0.474	0.876
400	-0.308	0.946

Table 7.10: Reflection coefficients calculated with a magnetic line source with variable MUT thickness (Plexiglas)

MUT Thickness (mil)	Γ'	Γ''
120	-0.5739	0.3346
160	-0.3516	0.2911
200	-6.04×10^{-2}	0.102
240	-0.1982	0.1043
280	-0.3513	- 0.2345
320	-0.4794	- 0.2430
360	-0.5615	- 0.1989
400	-0.6000	- 0.1403

Table 7.11: Reflection coefficients calculated with a TM plane wave (35% MagRAM)

MUT Thickness (mil)	Γ'	Γ''
120	-0.603	0.301
160	-0.406	0.270
200	-0.259	0.120
240	-0.250	-7.50×10^{-2}
280	-0.349	-0.198
320	-0.464	-0.227
360	-0.545	-0.201
400	-0.590	-0.154

Table 7.12: Reflection coefficients calculated with a magnetic line source with variable MUT thickness (35% MagRAM)

MUT Thickness (mil)	Γ'	Γ''
120	-0.9097	0.4146
160	-0.8385	0.5443
200	-0.7456	0.6656
240	-0.6306	0.7752
280	-0.4932	0.8688
320	-0.3339	0.9413
360	-0.1545	0.9863
400	0.0411	0.9971

Table 7.13: Reflection coefficients calculated with a TE plane wave (Plexiglas)

MUT Thickness (mil)	Γ'	Γ''
120	-0.911	0.415
160	-0.840	0.545
200	-0.747	0.667
240	-0.632	0.777
280	-0.494	0.871
320	-0.334	0.944
360	-0.154	0.990
400	-4.14×10^{-2}	1.001

Table 7.14: Reflection coefficients calculated with an electric line source with variable MUT thickness (Plexiglas)

MUT Thickness (mil)	Γ'	Γ''
120	-0.3319	0.4177
160	-0.0820	0.3193
200	0.0603	0.1019
240	0.0397	- 0.1299
280	-0.0914	- 0.2699
320	-0.238	-0.298
360	-0.3462	- 0.2579
400	-0.4027	- 0.1876

Table 7.15: Reflection coefficients calculated with a TE plane wave(35% MagRAM)

MUT Thickness (mil)	Γ'	Γ''
120	-0.331	0.419
160	-8.14×10^{-2}	0.320
200	-6.04×10^{-2}	0.102
240	-3.96×10^{-2}	-0.129
280	-9.16×10^{-2}	-0.269
320	-0.238	-0.298
360	-0.347	-0.256
400	-0.402	-.0186

Table 7.16: Reflection coefficients calculated with an electric line source with variable MUT thickness (35% MagRAM)

MUT Thicknesses	ϵ_r'	ϵ_r' Percent Error	ϵ_r''	ϵ_r'' Percent Error
120 and 240 mil	10.6139	.34	- 1.4870	1.3
160 and 320 mil	10.6367	.12	- 1.5119	.73
200 and 400 mil	10.6300	.19	- 1.5098	.6

Table 7.17: Extracted ϵ_r calculated with an electric line source reflection coefficients (MagRAM)

MUT Thicknesses	μ_r'	μ_r' Percent Error	μ_r''	μ_r'' Percent Error
120 and 240 mil	1.6487	.078	- 0.9079	.88
160 and 320 mil	1.6525	.15	- 0.9037	.41
200 and 400 mil	1.6534	.21	- 0.9024	.27

Table 7.18: Extracted μ_r calculated with an electric line source reflection coefficients (MagRAM)

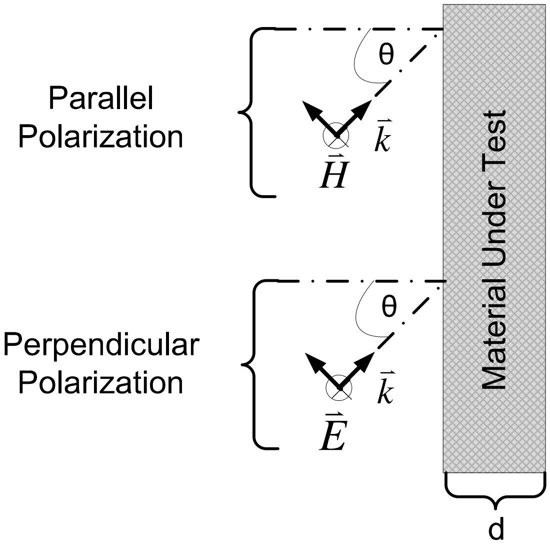

Figure 7.1: Diagram of plane wave incidence for free-space material characterization

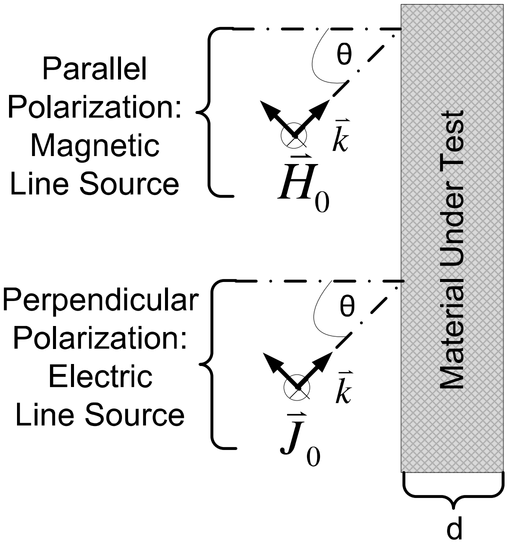

Figure 7.2: Diagram of curved wavefront incidence for free-space material characterization

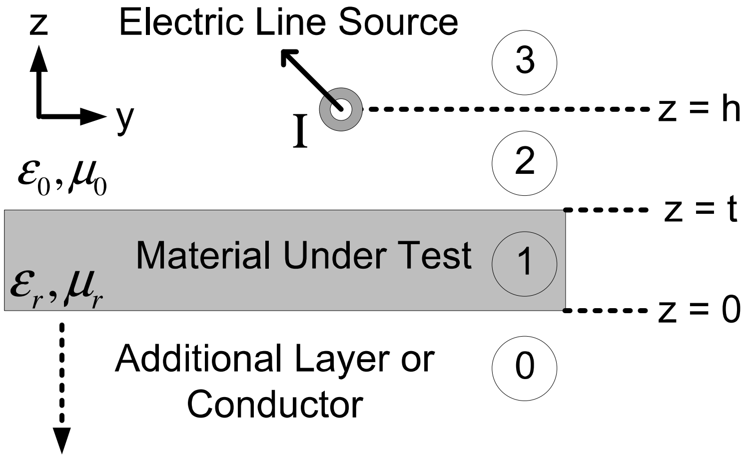

Figure 7.3: Diagram of a line source above a layered slab

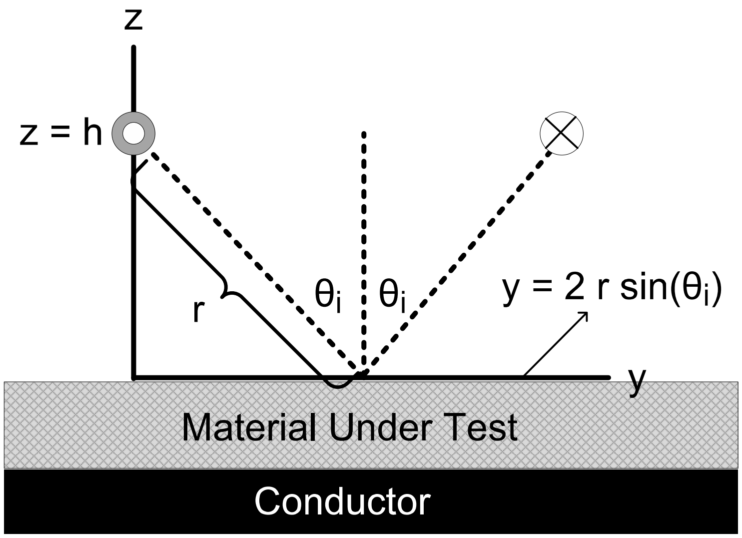

Figure 7.4: Geometry reflection coefficient simulations

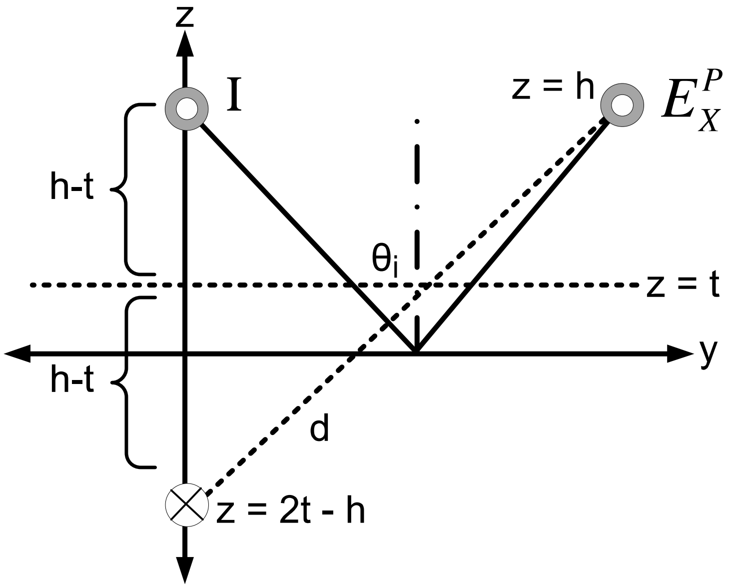

Figure 7.5: Image theory setup

Chapter 8

Conclusions

The main objective of this dissertation is the study of the strengths and weaknesses of various reflection-only material characterization methods by performing a thorough error analysis. More specifically, it was desired to know the propagation of measurement errors into extracted material parameters.

The characterization of materials with reflection-only free-space techniques requires the analysis of plane wave reflection off of a planar slab. Thus, the canonical problem, of plane wave incidence on an infinite slab is of great importance. Furthermore, the reflection-only coaxial-line and waveguide methods presented in this work can be considered special cases of plane wave propagation. In Chapter 2 the general analysis of this canonical problem is shown in detail. Topics covered in this chapter include: (1) plane wave propagation in unbounded media, (2) reflection and transmission at normal and oblique incidence, and (3) reflection and transmission at layered slabs.

Error analysis is an extremely important aspect of material characterization. In perspective of the many applications of material characterization, some of which are listed in Chapter 2, the level of certainty in the extracted permittivity and permeability is paramount. Error analysis in material characterization has included the study of the effect of temperature [8], calibration liquids [41], numerical techniques [40], propagation of high order modes [12], and air gaps in material samples [55] on the reliability of the characterization process.

Chapter 3 expounds upon the error analysis methods utilized in this work. In addition, an overview of types of uncertainty, interpretation of uncertainty, and the normal distributed are presented.

Chapter 4 demonstrated the use of a unifying set of extraction equations for many non-resonant, reflection-only material characterization methods. Accuracy of the extraction equations was proven via implementation of three different reflection-only methods with actual measured data of both dielectric and magnetic media. Excellent agreement between extracted ϵ_r and μ_r using the extraction equations presented in this work and traditional material characterization methods and nominal material parameters was achieved. Therefore, a common resource for all performing material characterization using non-resonant, reflection-only material characterization methods has been accomplished.

In Chapter 5, the dual-polarization method for characterization of both ϵ_r and μ_r is examined. Although the dual-polarization method can be formulated for dielectrics with unknown thickness or dielectrics with known thickness, the focus of this chapter is on characterizing conductor-backed media for both ϵ_r and μ_r.

Thorough analysis of the error propagated into the extraction of ϵ_r and μ_r by uncertainties in angle, thickness, and reflection coefficients has been conducted. Analysis has shown that the dual-polarization method can be very sensitive to uncertainties in angle and reflection coefficients, but relatively insensitive to uncertainties of MUT thickness. However, in very specific situations, the dual-polarization method have been can be applied accurately.

Chapter 6 demonstrated use of interval analysis for error analysis in reflection-only material characterization techniques. Interval analysis is shown to be useful by implementing it in predicting the error introduced by incidence angle uncertainty into the layer-shift method. Error tolerances predicted with interval analysis are compared to error bounds predicted with Monte Carlo simulations. Excellent agreement between error bounds found with Monte Carlo simulations and refined interval analysis are found. Thus, an additional tool for performing error analysis for material characterization has been found. Future work includes performing multivariate error analysis with interval analysis.

In Chapter 7, the impact of wave curvature on free-space material characterization methods has been investigated. The plane wave assumption in free-space material characterization methods can be thought of as a type of systematic error in all free-space methods because a true plane wave is not physically realizable in a laboratory environment.

To test the impact of wave curvature, the Fresnel reflection coefficients for TE and TM polarized waves are replaced with reflection coefficients calculated with electric and magnetic line sources in the two-thickness extraction algorithm. Results showed very little impact on the reflection coefficients or extracted ϵ_r and μ_r values for the line source distance of 1 m. As many labaratory setups should be able to have greater distance between the source antenna and the MUT, the impact on wave curvature is not expected to be great in many free-space material characterization measurements.

BIBLIOGRPAHY

Bibliography

[1] Eccosorb fgm-40: Thin, flexible, broadband, microwave absorber. Technical report, Emerson & Cuming Microwave Products N.V.

[2] *On the Inadequacy of the overlay method for characterizing a conductor-backed material using free-space measurements*, 2010.

[3] S. M. Matitsin L. N. Novogrudskiy K. N. Rozanov A. K. Sarychev A. V. Seleznev A. A. Kalachev, I. V. Kukolev. The methods of investigation of complex dielectric permittivity of layer polymers containing conductive inclusions. In J. A. Emerson and J. M. Torkelson, editors, *Optical and Electrical Properties of Polymers, Materials Reseach Society Symposia Proceedings*, volume 214, pages 119–124, Pittsburgh, PA, 1991.

[4] J. Baker-Jarvis, E. J. Vanzura, and W. A. Kissick. Improved technique for determining complex permittivity with the transmission/reflection method. *IEEE Transactions on Microwave Theory Techniques*, 38:1096–1103, August 1990.

[5] S. Bakhtiari, S. I. Ganchev, and R. Zoughi. Open-ended rectangular waveguide for nondestructive thickness measurement and variation detection of lossy dielectric slabs backed by a conducting plate. 42(1):19–24, 1993.

[6] S. Bakhtiari, N. Qaddoumi, S. I. Ganchev, and R. Zoughi. Microwave noncontact examination of disbond and thickness variation in stratified composite media. *IEEE Transactions on Microwave Theory and Techniques*, 42(3):389–395, 1994.

[7] A. E. Bogle, M. J. Havrilla, and E. J. Rothwell. Two-layer parallel-plate green's function due to a magnetic source for electromagnetic material characterization of conductor backed lossy media. In *Proc. IEEE Antennas and Propagation Society Int. Symp*, pages 169–172, 2007.

[8] S. Bringhurst, M.F. Iskander, and M.J. White. Thin-sample measurements and error analysis of high-temperature coaxial dielectric probes. *Microwave Theory and Techniques, IEEE Transactions on*, 45(12):2073 –2083, December 1997.

[9] H.E. Bussey. Measurement of rf properties of materials a survey. *Proceedings of the IEEE*, 55(6):1046 – 1053, 1967.

[10] X. Chen, D. Liang, and K. Huang. Microwave imaging 3-D buried objects using parallel genetic algorithm combined with FDTD technique. *Journal of Electromagnetic Waves and Applications*, 20:1761–1774, December 2006.

[11] Robert E. Collin. *Field Theory of Guided Waves.* John Wiley & Sons, New York, NY, 2 edition, 1991.

[12] T. W. Dakin and C. N. Works. Microwave Dielectric Measurements. *Journal of Applied Physics*, 18:789–796, September 1947.

[13] Gary Dester. *Electromagnetic Material Characterization of a Conductor-Backed Material Using the Two-Layer, Two Thickness, and Two-Iris Waveguide Methods: Error Analysis, Simulations, and Experimental Results.* PhD thesis, Michigan State University, 2008.

[14] Paul Drude. Zeits. f. physik. *physik. Chemie, Ann. Physik und Chemie*, 267:466, 1897.

[15] Stephen A. Dyer. *Survey of instrumentation and measurement.* John Wiley & Sons, 2001.

[16] M.J. Cloud E.J. Rothwell. *Electromagnetics.* CRC Press, Boca Raton, FL, 2nd edition, 2009.

[17] G. F. Engen and C. A. Hoer. Thru-reflect-line: An improved technique for calibrating the dual six-port automatic network analyzer. 27(12):987–993, 1979.

[18] I. Gargantini and P. Henrici. Circular arithmetic and the determination of polynomial zeros. *Numerische Mathematik*, 18(4):305–320, 1971.

[19] G. I. Hargreaves. Interval analysis in MATLAB. *Manchester Centre for Comp. Math., Manchester, Numerical Analysis Report*, 416, 2002.

[20] R.F. Harrington. *Time-harmonic electromagnetic fields.* IEEE Press series on electromagnÃľtic wave theory. IEEE Press, 2001.

[21] Hewlett Packard. *User's Guide: HP8753 Network Analyzer*, December 1997.

[22] A.R. Hippel. *Dielectrics and Waves.* John Willey & Sons, New York, 1954.

[23] Ifan Hughes and Thomas Hase. *Measurements and Their Uncertainties: A Practical Guide to Modern Error Analysis.* Oxford University Press, USA, 2010.

[24] Umran Inan and Aziz Inan. *Electromagnetic Waves.* Prentice Hall, Upper Saddle River, NJ, 2000.

[25] Michel Kieffer, Luc Jaulin, Éric Walter, and Dominique Meizel. Robust autonomous robot localization using interval analysis. *Reliable Computing*, 6:337–362, 2000. 10.1023/A:1009990700281.

[26] R. Klatte and Ch. Ullrich. Complex sector arithmetic. *Computing*, 24(2):139–148, June 1980.

[27] P. Koivisto. Reduction of errors in antenna radiation patterns using optimally truncated spherical wave expansion. *Progress In Electromagnetics Research*, 47:313–333, 2004.

[28] Friedrich Kremer and Andreas Schönhals, editors. *Broadband Dielectric Spectroscopy.* Springer, 1 edition, 2002.

[29] Jerzy Krupka. Frequency domain complex permittivity measurements at microwave frequencies. *Measurement Science and Technology*, 17, 2006.

[30] Z.-F. Li L. Ma and G. Liao. System error analysis and calibration methods for multi-channel sar. *Progress In Electromagnetics Research*, 112:309–327, 2011.

[31] J. Lai, D. Hughes, E. Gallaher, and R. Zoughi. Determination of the thickness and dielectric constant of a dielectric slab backed by free-space or a conductor through inversion of the reflection coefficient of a rectangular waveguide probe. In *Proc. 21st IEEE Instrumentation and Measurement Technology Conf. IMTC 04*, volume 1, pages 56–60, 2004.

[32] D. M. W. Leenaerts. Application of interval analysis for circuit design. 37(6):803–807, 1990.

[33] C.P. Neo V.V. Varadan V.K. Varadan L.F. Chen, C.K. Ong. *Microwave Electronics.* John Wiley & Sons Ltd, 2004.

[34] J. Matthews, R. Broadwater, and L. Long. The application of interval mathematics to utility economic analysis. *Power Systems, IEEE Transactions on*, 5(1):177 –181, feb. 1990.

[35] David Moens and Dirk Vandepitte. Interval sensitivity theory and its application to frequency response envelope analysis of uncertain structures. *Computer Methods in Applied Mechanics and Engineering*, 196(21-24):2486 – 2496, 2007.

[36] Ramon E. Moore. Interval arithmetic and automatic error analysis in digital computing, 1962.

[37] Ramon E. Moore, R. Baker Kearfott, and Michael J. Cloud. *Introduction to Interval Analysis.* SIAM, 2009.

[38] J.E. Besson M.G. Fabry Mosig, J.R. and F.E. Gardiol. Reflection of an open- ended coaxial line and application to non-destructive measurement of materials. *IEEE Trans. Instrum. Meas.*, IM-30:45–51, 1991.

[39] S. O. Nelson and S. Trabelsi. Measurement of grain and seed moisture and density through permittivity relationships. In *Proc. IEEE Instrumentation and Measurement Technology Conf. (I2MTC)*, pages 964–969, 2010.

[40] A. M. Nicolson and G. F. Ross. Measurement of the intrinsic properties of materials by time-domain techniques. *Instrumentation and Measurement, IEEE Transactions on*, 19(4):377 –382, 1970.

[41] A. Nyshadham, C.L. Sibbald, and S.S. Stuchly. Permittivity measurements using open-ended sensors and reference liquid calibration-an uncertainty analysis. *Microwave Theory and Techniques, IEEE Transactions on*, 40(2):305 –314, February 1992.

[42] Committee on the Survey of Materials Science and Engineering, editors. *Materials and Man's Needs: Materials Science and Engineering – Volume I, The History, Scope, and Nature of Materials Science and Engineering.* National Academy of Sciences, 1975.

[43] N. Polydorides. Linearization error in electrical impedance tomography. *Progress In Electromagnetics Research*, 93:323–337, 2009.

[44] V. Demir J. R. Gladden R. K. Challa, D. Kajfez and A. Z. Elsherbeni. Permittivity measurement with a non-standard waveguide by using trl calibration and fractional linear data. *Progress In Electromagnetics Research B*, Vol. 2:1–13, 2008.

[45] Semyon Rabinovich. *Measurement errors and uncertainties: theory and practice.* Springer, 3rd edition edition, August 15, 2005.

[46] Simon Ramo, John R. Whinnery, and Theodore Van Duzer. *Fields and waves in communication electronics.* Wiley, 1994.

[47] W. Romanoff. *Handbuch dey Physik*, volume XV. Julius Springer Verlag, Berlin, 1927.

[48] S.M. Rump. INTLAB - INTerval LABoratory. In Tibor Csendes, editor, *Developments in Reliable Computing*, pages 77–104. Kluwer Academic Publishers, Dordrecht, 1999. `http://www.ti3.tu-harburg.de/rump/`.

[49] F. Sagnard, F. Bentabet, and C. Vignat. In situ measurements of the complex permittivity of materials using reflection ellipsometry in the microwave band: experiments (part ii). 54(3):1274–1282, 2005.

[50] F. Sagnard, F. Bentabet, and C. Vignat. In situ measurements of the complex permittivity of materials using reflection ellipsometry in the microwave band: theory (part i). *IEEE Transactions on Instrumentation and Measurement*, 54(3):1266–1273, 2005.

[51] John M. Snyder. Interval analysis for computer graphics. *SIGGRAPH Comput. Graph.*, 26(2):121–130, 1992.

[52] Trevor J. Duguid Farrant Stephen L R Ellison, Vicki J. Barwick. *Practical Statistics for the Analytical Scientist: A Bench Guide.* The Royal Society of Chemistry, 2009.

[53] John R. Taylor. *An Introduction to Error Analysis: The Study of Uncertainties in Physical Measurements.* University Science Books, 1997.

[54] W.B. Weir. Automatic measurement of complex dielectric constant and permeability at microwave frequencies. *Proceedings of the IEEE*, 62(1):33 – 36, 1974.

[55] T.C. Williams, M.A. Stuchly, and P. Saville. Modified transmission-reflection method for measuring constitutive parameters of thin flexible high-loss materials. *Microwave Theory and Techniques, IEEE Transactions on*, 51(5):1560 – 1566, May 2003.

[56] R. Zoughi. *Microwave Non-Destructive Testing and Evaluation.* Kluwer Academic Publishers, 2000.